Supplementary Material

The Great Oxidation from a minimal ocean–atmosphere model

Matthew D. Schwartz[a], David T. Johnston[b]

[a]Department of Physics, Harvard University, Cambridge, MA, USA

[b]Department of Earth and Planetary Sciences, Harvard University, Cambridge, MA, USA

This supplement contains Texts S0–S8 with their figures and tables and its own reference list. Text S0 lists symbols and units; S1 gives the full model and its present-day closure; S2 the inputs and their provenance; S3 the geological data, the comparisons with the rock record and their numerical reproducibility; S4 the sensitivity to the outgassing exponent and to the assumptions; S5 the roles of an imposed Lomagundi excursion; S6 the phosphorus ceiling; S7 the steady states of two published models; S8 the paleosol CO_2 barometry.

Contents

S0 Symbols, units and constants

Tables S1–S3 list the symbols of equations (1)–(9) of the main text, with the anoxic branch (2′), and of (S1)–(S7) of Supplementary Text S1, with (S2a)–(S2d), each with its meaning, its unit or value, and, for the fluxes and parameters, the equation in which it is defined. Ages t are in Ga and durations in Myr, and every flux is in Tmol yr^{-1}, with organic-carbon burial counted in moles of carbon (one mole of carbon buried releases one mole of O_2) and reductant fluxes in O_2 equivalents. The source of each value is given in Table 1 of the main text and Tables S8–S10.

Table S1: State variables, units and inventories.

Symbol	Meaning	Unit or value
O	atmospheric oxygen	present atmospheric level (PAL); 1 PAL = 3.7×10^{19} mol of O_2; $p_{O_2} = 0.21\,O$ bar
N	atmospheric methane	Tmol CH_4; $p_{CH_4} = N/N_{atm}$
C	atmospheric carbon dioxide	multiples of the pre-industrial level (278 ppmv); $C = 1$ corresponds to 5×10^{16} mol of carbon
P	dissolved phosphate	model units (present riverine steady state with no iron trap = 1)
ice state	open water or global glaciation	switched by equation (8) of the main text and (S7)
n_{O_2}	oxygen content of one PAL	3.7×10^{19} mol
N_{atm}	gas content of one bar of atmosphere	1.8×10^{20} mol = 1.8×10^{8} Tmol (Claire et al., 2006)
n_C	carbon content of one pre-industrial atmosphere of CO_2	5×10^{16} mol
t; $t_\times$; t_{ref}	age; prescribed epoch at which the open-water oxygen budget crosses zero (burial first balances the oxygen-independent sinks, equation (3) of the main text); reference age of the Archean burial fraction	Ga; 2.4425 Ga (inside 2.46–2.43 Ga); 2.65 Ga
ΔT; F	global temperature anomaly; radiative forcing relative to the pre-industrial state	K; W m^{-2}

Table S2: Fluxes ($\mathrm{Tmol\,yr^{-1}}$; reductant fluxes in O_2 equivalents), with the equation in which each is defined and, where one is specified, its present-day or Archean value.

Symbol	Meaning	Defined	Value
B_{mar}	marine organic-carbon burial, $a_{\mathrm{mar}}\,p(t)\,P/(P+P_h)$	(1), (S4)	6.67 today; $N_A = 2.07$ in the Archean
$B_{\mathrm{land}}\,\phi(O)$	terrestrial organic burial times the fire factor	(S1)	$L_0 = 3.33$ today; zero before 0.47 Ga
S_{land}	natural terrestrial methane source	(S1), (S2)	13.6 (218 $\mathrm{Tg\,CH_4\,yr^{-1}}$) today; zero before land plants
Ω	photochemical oxidation of methane by oxygen, $k_{\mathrm{eff}}\,n_{\mathrm{O_2}}\,O\,N$; zero on the anoxic branch ($R > B_{\mathrm{mar}}$, no free oxygen); in the numerical solution the term is continued through $O = 0$, where it takes the value $-\frac{1}{2}(R - B_{\mathrm{mar}})$ and passes the unmet hydrogen to the methane equation (Sec. S1.3)	(2), (2′), (S2b)	0 (numerically -0.22 $\mathrm{Tmol\,CH_4\,yr^{-1}}$) before the nickel decline; positive after 2.64 Ga
$k_{\mathrm{esc}}N$	escape to space of the hydrogen carried by methane at the diffusion limit, in O_2 equivalents (numerically also the methane lost, in $\mathrm{Tmol\,CH_4\,yr^{-1}}$); the methane-borne part of the total hydrogen escape E_{H} of (S2d); $= G + \frac{1}{2}(R - B_{\mathrm{mar}})$ on the anoxic branch	(2), (2′), (S2c), (S2d)	1.86 $\mathrm{Tmol\,CH_4\,yr^{-1}}$ before the nickel decline (the whole reductant excess over burial, of which $G_A = 1.64$ is made from the methanogens' own hydrogen supply and 0.22 from hydrogen in excess of burial; Sec. S1.3)
E_{H}	total hydrogen escape to space at the diffusion limit, in O_2 equivalents, $\Phi_0 f_T$ with $\Phi_0 = 3340$ and $f_T = f_{\mathrm{H_2}} + 2f_{\mathrm{CH_4}}$ the total hydrogen mixing ratio; $2k_{\mathrm{esc}}N$ under the adopted assumption that the hydrogen freed when water oxidizes the escaping carbon escapes too ($f_{\mathrm{H_2}} = 2f_{\mathrm{CH_4}}$), $k_{\mathrm{esc}}N$ under the alternative that methanogens consume it (Secs. S1.2 and S1.3)	(S2a), (S2d)	2×1.86 before the nickel decline under the adopted assumption (the whole excess $R_A + 2G_A - N_A$); the same total under the alternative, then carried by twice the methane
$W_{\mathrm{ox}}O^{1/2}$	oxidative weathering of old sedimentary organic carbon	(1)	$W_{\mathrm{ox}} = 8.19$ at $O = 1$
$R(t)$	oxygen-independent reductant sink (volcanic and metamorphic gases), $R_A\,r_{\mathrm{Ni}}(t)$ before $t_\times$, halved at the subaerial-volcanism step (2.5 Ga)	(1), (3)	$R_A = 2.5$
$G(t)$	hydrogen-fed marine methane source, $G_A\,r_{\mathrm{Ni}}(t)$ before $t_\times$	(2), (3)	$G_A = 1.64$ $\mathrm{Tmol\,CH_4\,yr^{-1}}$ ($= 6.56$ $\mathrm{Tmol\,H_2\,yr^{-1}}$); 0.66 today
$S(t)$	total oxygen-independent sink $R + 2G$; after $t_\times$, $f_{\mathrm{org}}(t)\,V_{\mathrm{out}}(t)$	(4)	2.07 at $t_\times$; 1.82 today
$V_{\mathrm{out}}(t)$	volcanic and metamorphic outgassing of carbon	(6)	$V_{\mathrm{mod}} = 8$ today
W_{sil}	continental silicate weathering ending as buried carbonate	(7)	$W_0 = 5.73$ today
F_{sfw}	seafloor weathering (carbonate precipitated in altered ocean crust)	(S5)	$F_d = 0.459$ today
$W_P(t)$	riverine phosphate delivery	(S4)	1 in model units; $\times 3$ over 0.75–0.635 Ga
$k_s P$	phosphate scavenging by iron oxides	(S4)	

Table S3: Parameters and constants, grouped by the part of the model in which they act. "Where" gives the equation of the main text or of Supplementary Text S1 in which the symbol first appears, or, for a quantity that appears in no displayed equation, the section in which it is introduced. Sources are given in Table 1 of the main text and Tables S8–S10.

Symbol	Meaning	Where	Value
Oxygen, methane and the reductant budget			
$k_{\mathrm{eff}}(p_{\mathrm{O_2}}, p_{\mathrm{CH_4}})$	effective rate constant for the net photochemical destruction of CH_4 by O_2 (Claire et al., 2006)	(2)	tabulated surface; 3×10^{-9} $\mathrm{Tmol^{-1}\,yr^{-1}}$ at 0.21 bar
k_{esc}; Φ_0	hydrogen-escape rate constant for methane, $2\Phi_0/N_{\mathrm{atm}}$; diffusion-limited escape per unit total hydrogen mixing ratio (Claire et al., 2006)	(2), (S2d)	3.7×10^{-5} $\mathrm{yr^{-1}}$; 3340 Tmol O_2-eq $\mathrm{yr^{-1}}$
a_{mar}; $p(t)$, p_A	modern marine burial; productivity factor and its pre-Neoproterozoic value	(S4)	6.67 Tmol C $\mathrm{yr^{-1}}$; $p_A = 0.332$; $p = 1$ after 0.65 Ga
P_h	half-saturation constant of the nutrient factor	(S4)	0.007 (factor 0.93 Archean, 0.99 today)
N_A; f_A	Archean net organic burial $f_A V_{\mathrm{out}}(t_{\mathrm{ref}})$; late-Archean burial fraction	(3), (4)	2.07 Tmol C $\mathrm{yr^{-1}}$; 0.137 ± 0.011
$f_{\mathrm{org}}(t)$; $f_\times$; δ_{in}	burial fraction, piecewise linear through $f_\times$ at $t_\times$, 0.179 at 1.40 Ga and 0.228 at 0.27 Ga; input-carbon composition	(4)	$f_\times = 0.148$; $\delta_{\mathrm{in}} = -5 \pm 1$ per mil
W_{ox}	amplitude of oxidative weathering of sedimentary organic carbon at one PAL	(1)	8.19 Tmol $\mathrm{yr^{-1}}$
R_A; G_A	reductant and methane amplitudes at $r_{\mathrm{Ni}} = 1$	(3)	2.5 Tmol O_2-eq $\mathrm{yr^{-1}}$; 1.64 Tmol CH_4 $\mathrm{yr^{-1}}$
$r_{\mathrm{Ni}}(t)$	normalized nickel series: 1 before 2.7 Ga, 0.5 at 2.5 Ga, 0.0225 at 0.55 Ga, log-linear between	(3)	
θ	fraction of sub-ice oxygen and methane production vented to the air	Sec. S1.8	zero (the four glaciations remain when θ is raised to 0.03)
Carbon, weathering and outgassing			
V_{mod}	modern outgassing	(6)	8 Tmol C $\mathrm{yr^{-1}}$ (prior 6–10)
ν, n, m	outgassing exponent $\nu = nm$; heat-flow exponent; outgassing-to-heat-flow power	(6), (S5)	0.715, the midpoint of the four-glaciation interval $(0.7075, 0.7225)$ fixed by the glacial record, inside the published range $[0, 1.46]$; $n = 0.73$ in $[0, 0.73]$; implied $m = \nu/n = 0.98$, slightly below the sampled range $[1, 2]$ (Krissansen-Totton et al., 2018)
W_0; β; $f_w(t)$	modern silicate weathering; its CO_2 exponent; emergence weatherability, $0.5 \to 1$ over 2.55–2.45 Ga	(7)	5.73 Tmol C $\mathrm{yr^{-1}}$; 0.3
λ; T_e	temperature per unit forcing; e-folding temperature of weathering	(7)	0.69 K per W $\mathrm{m^{-2}}$; 11.1 K
β_w; τ_{sil}; n_0	ocean–atmosphere carbon partition; silicate-weathering response time; $\partial \ln W_{\mathrm{sil}}/\partial \ln C$ today	(5), (S6)	29.6; 380 kyr; 0.68
β_{ice}	partition under ice (store returned at the thaw)	(9)	$= \beta_w$; airborne share 3.4%
F_d, E_a, γ, b, f_{sed}	seafloor weathering: modern flux, activation energy, CO_2 exponent, spreading exponent, early sediment thickness	(S5)	0.459 Tmol C $\mathrm{yr^{-1}}$, 75 kJ $\mathrm{mol^{-1}}$, 0.27, 1, 0.6
T_p, $T_{p,0}$; R_g; $Q(t)$	pore-water temperature (deep water $1.02\,T_s - 16.67$ K for surface temperature T_s, floor 271.15 K, plus 9 K today) and its present value; gas constant; relative heat flow $(1 - t/4.5\,\mathrm{Gyr})^{-n}$	(S5)	
Climate and ice			
$F_{\mathrm{CO_2}}$, $F_{\mathrm{CH_4}}$	radiative forcings for an anoxic atmosphere with 1 bar N_2 (Byrne and Goldblatt, 2014), relative to reference levels of 278 ppmv CO_2 and 0.715 ppmv CH_4	(8)	W $\mathrm{m^{-2}}$
$Q_\odot$; $s(t)$	absorbed sunlight today; relative solar luminosity (Gough, 1981)	(8)	238.17 W $\mathrm{m^{-2}}$; $[1 + \frac{2}{5}t/4.57\ \mathrm{Gyr}]^{-1}$
D^*; $H(t)$	glaciation threshold (forcing deficit); methane-free CO_2 at which it is met	(8)	10.1 W $\mathrm{m^{-2}}$; 72 × pre-industrial at the first glaciation
X, C_X; r; s_{cal}; Q_{ice}	deglaciation CO_2 level and the same in pre-industrial units; forcing amplitude of the snowball models; their insolation; sunlight absorbed by a snowball today (albedo 0.6)	(S7)	0.01 bar (36); 0.686; 0.94; 136.1 W $\mathrm{m^{-2}}$
T_{f}	deep-water temperature under ice (the freezing point)	(9)	271.15 K
Phosphorus and later schedules			
k_0; O_d	iron-trap strength; oxygen level above which the trap switches off	(S4)	10 before 0.72 Ga, 1.67 after 0.55 Ga; 0.3 PAL
L_0; O_f	modern land burial; oxygen level of fire suppression, $\phi = [1 + (O/O_f)^5]^{-1}$	(S1)	3.33 Tmol C $\mathrm{yr^{-1}}$; 0.75 PAL
Numerical integration and thresholds			
(none)	start of integration; oxygen threshold for onset and permanence; age down to which glaciations are counted as Paleoproterozoic (those beginning at or before it; the absence of glaciation between this age and the Cryogenian sets the lower limit on ν)	Sec. S1.11	3.0 Ga; 10^{-5} PAL; 2.22 Ga

S1 Model details and the present-day closure

The equations of the main text are written for ages older than 0.47 Ga, before land plants, when the terrestrial burial and terrestrial methane terms of the model are zero. Here we give the full system that we integrate from 3.0 Ga to the present, the rate laws and constants not written out in the main text, the redox budget of the atmosphere while it holds no free oxygen, the alternatives to the adopted reductant sink and sub-ice carbon budget, and the carbon and alkalinity balance through a deglaciation under the two storage cases. In the last subsection we compare the model's present-day steady state with the budget of Holland (2002) quantity by quantity. Most of those quantities are set to their modern values when the model is built, and their agreement with Holland's estimates is therefore not a test of the model. Symbols are collected in Supplementary Text S0, and every input is listed with its source and published range in Supplementary Text S2.

S1.1 The full system integrated to the present

Atmospheric oxygen changes at the rate at which organic carbon is buried at sea and on land, plus the oxygen released in making terrestrial methane, less the oxygen consumed by methane oxidation, by the oxidative weathering of old organic carbon (kerogen) and by the volcanic and metamorphic reductant flux,

$$n_{\mathrm{O_2}}\,\dot{O} = B_{\mathrm{mar}} + B_{\mathrm{land}}\,\phi(O) + 2S_{\mathrm{land}} - 2\,\Omega - W_{\mathrm{ox}}\,O^{1/2} - R(t). \tag{S1}$$

Here O is atmospheric oxygen in units of the present atmospheric level (PAL, 3.7×10^{19} mol of $\mathrm{O_2}$), $n_{\mathrm{O_2}}$ is the oxygen content of one PAL, a dot is the rate of change forward in time, t is age, and every flux is in $\mathrm{Tmol\,yr^{-1}}$. Atmospheric methane N, in Tmol with one bar equal to $N_{\mathrm{atm}} = 1.8\times10^{8}$ Tmol (Claire et al., 2006), changes at the rate of its hydrogen-fed marine source and its terrestrial source, less photochemical oxidation and hydrogen escape,

$$\dot{N} = G(t) + S_{\mathrm{land}} - \Omega - k_{\mathrm{esc}}N, \qquad \Omega = k_{\mathrm{eff}}(p_{\mathrm{O_2}}, p_{\mathrm{CH_4}})\,n_{\mathrm{O_2}}\,O\,N. \tag{S2}$$

On the open-water branch atmospheric carbon dioxide C, in multiples of the pre-industrial level (5×10^{16} mol of carbon), changes at the rate of outgassing plus kerogen oxidation, less organic burial at sea and on land, continental silicate weathering and seafloor weathering,

$$n_{\mathrm{C}}\,\beta_w\,\dot{C} = V_{\mathrm{out}}(t) + W_{\mathrm{ox}}O^{1/2} - B_{\mathrm{mar}} - B_{\mathrm{land}}\phi(O) - W_{\mathrm{sil}}(C,\Delta T,t) - F_{\mathrm{sfw}}(C,\Delta T,t), \tag{S3}$$

where n_{C} is the carbon content of one pre-industrial atmosphere of $\mathrm{CO_2}$ and β_w is the ocean–atmosphere partition of Section S1.5. Dissolved phosphate, the fourth reservoir, relaxes within about 222 yr to the balance of riverine delivery against burial and iron-oxide scavenging, and at the ages of interest it is therefore in quasi-steady state, with marine organic burial set by the steady-state phosphate concentration,

$$P = \frac{W_P(t)}{1 + k_s(O,t)}, \qquad k_s = \frac{k_0(t)}{1 + (O/O_d)^4}, \qquad B_{\mathrm{mar}} = a_{\mathrm{mar}}\,p(t)\,\frac{P}{P + P_h}. \tag{S4}$$

Here W_P is the riverine phosphate delivery in units of its present value, equal to one except during the Neoproterozoic pulse of Section S1.10; $k_0 = 10$ is the strength of phosphate scavenging by iron oxides (the iron trap) before the Neoproterozoic; and $O_d = 0.3$ PAL is the oxygen level above which the deep water oxygenates and the trap switches off. The modern marine burial $a_{\mathrm{mar}} = 6.67$ $\mathrm{Tmol\,C\,yr^{-1}}$ is the organic burial of Holland (2002), 10.0 ± 3.3 $\mathrm{Tmol\,yr^{-1}}$, times the marine share of Burdige (2005), two thirds. With the half-saturation constant $P_h = 0.007$ the nutrient factor $P/(P+P_h)$ is 0.93 in the Archean and 0.99 today. The productivity factor $p(t)$ is one today and $p_A = 0.332$ before the Neoproterozoic, the value at which Archean marine burial equals the isotope-implied net burial $N_A = 2.07$ $\mathrm{Tmol\,C\,yr^{-1}}$ of the main text.

The terrestrial organic burial $B_{\mathrm{land}}\,\phi(O)$ increases linearly from zero between 0.47 and 0.40 Ga (Rubinstein et al., 2010; Morris et al., 2018) to the amplitude at which $B_{\mathrm{land}}\phi(1)$ equals the modern land burial $L_0 = 3.33$ $\mathrm{Tmol\,C\,yr^{-1}}$, one third of Holland's total organic burial. The factor $\phi(O) = [1 + (O/O_f)^5]^{-1}$ with $O_f = 0.75$ PAL suppresses burial on land as oxygen rises into the range in which wildfire limits vegetation (Belcher and McElwain, 2008). The terrestrial methane source S_{land} is the natural land source in the top-down methane budget of Saunois et al. (2020), 218 $\mathrm{Tg\,CH_4\,yr^{-1}}$ (183–248), or 13.6 $\mathrm{Tmol\,yr^{-1}}$, introduced with land plants over the same interval as the terrestrial burial. Because this methane is made from photosynthate, each mole of $\mathrm{CH_4}$ added to (S2) is accompanied by two moles of $\mathrm{O_2}$ added to (S1), and the source is oxygen-neutral once that methane is oxidized. This source accounts for nearly all of the model's modern methane, 0.70 ppmv; the hydrogen-fed source, $G(0) = 0.66$ $\mathrm{Tmol\,yr^{-1}}$ today, is a small addition to it. For ages older than 0.47 Ga both terms vanish identically, and (S1), (S2) and (S3) are then equations (1), (2) and (5) of the main text with no approximation. The model reaches $O = 1$ today because W_{ox} is set to close the present-day oxygen budget at one PAL (Section S1.11). The modern oxygen level therefore carries no information about oxygen regulation in the model.

S1.2 The photochemical rate surface and hydrogen escape

We take k_{eff} from the surface that Claire et al. (2006) computed with a one-dimensional photochemical model as a function of $p_{\mathrm{O_2}}$ and $p_{\mathrm{CH_4}}$ (their Fig. 3), interpolate it bilinearly in $\log p_{\mathrm{O_2}}$ and $\log p_{\mathrm{CH_4}}$, and complete it at high oxygen with their modern point, $k_{\mathrm{eff}} = 3\times10^{-9}$ Tmol^{-1} yr^{-1} at 0.21 bar. Outside the tabulated range we use the edge value. At $\nu = 0.715$ methane is below the tabulated range in 18,492 of 22,615 evaluations of k_{eff}, all of them after the onset of the first glaciation, by which time methane has already collapsed and oxidation exceeds escape by orders of magnitude for any k_{eff}; oxygen is below its tabulated range in 3,795 evaluations. Two slightly different oxygen inventories per PAL are used, $n_{\mathrm{O_2}} = 3.7\times10^{19}$ *mol* in (S1) and $0.21\,N_{\mathrm{atm}}$ inside Ω, the second larger by two percent, and the difference does not affect any result reported here.

The last term of (S2) is the loss of methane to hydrogen escape. Escape is limited by diffusion above the tropospheric cold trap, and the diffusion-limited flux is proportional to the total mixing ratio of hydrogen in every form that reaches that level (Claire et al., 2006, their eqs. 9 and 10): in oxygen equivalents

$$E_{\mathrm{H}} = \Phi_0\, f_T, \qquad \Phi_0 = 3340\ \mathrm{Tmol\,yr^{-1}}, \qquad f_T = f_{\mathrm{H_2}} + 2f_{\mathrm{CH_4}} + \ldots, \tag{S2d}$$

where f_T is the total hydrogen mixing ratio in H_2 equivalents, in which a methane molecule counts for two. With $f_{\mathrm{CH_4}} = N/N_{\mathrm{atm}}$ the methane-borne part of (S2d) is $2\Phi_0 N/N_{\mathrm{atm}} = k_{\mathrm{esc}}N$, which defines $k_{\mathrm{esc}} = 2\Phi_0/N_{\mathrm{atm}} = 3.7\times10^{-5}$ yr^{-1} (Claire et al., 2006, their eq. 12); $k_{\mathrm{esc}}N$ is at once that flux in oxygen equivalents and the methane, in Tmol yr^{-1}, whose hydrogen is lost, because the four hydrogen atoms of a methane molecule amount to one oxygen equivalent. The carbon atom left behind is oxidized to CO_2. Where the air holds oxygen the net oxidant is O_2, and Claire et al. (2006) subtract one O_2 from the oxygen budget per escaping methane molecule (their eq. 14), a net loss of one oxygen equivalent of reducing power per molecule. Where it holds none the oxidant is water, through the OH and O that photolysis of water vapor and carbon dioxide supplies; the net reaction is $CH_4 + 2H_2O \rightarrow CO_2 + 4H_2$, and the redox budget then depends on whether the two hydrogen molecules that the water contributes escape or are consumed. In our integrations these two molecules escape as well: each methane molecule lost then removes two oxygen equivalents and consumes no oxygen, which is (S2) as written, with no escape term in (S1). Escape at that rate, $E_{\mathrm{H}} = 2k_{\mathrm{esc}}N$, requires by (S2d) an H_2 mixing ratio in the air of $f_{\mathrm{H_2}} \simeq 2f_{\mathrm{CH_4}}$: on the Archean plateau of Section S1.3, 555 ppmv of H_2 beside 279 ppmv of methane, together $f_T = 1.1\times10^{-3}$. The model does not track this hydrogen and assigns it no greenhouse effect, and if its supply stopped it would be lost within $1/k_{\mathrm{esc}} \approx 27$ kyr; its escape is an assumption of the model, not a result. The opposite assumption is that methanogens consume this hydrogen as they consume volcanic hydrogen ($4H_2 + CO_2 \rightarrow CH_4 + 2H_2O$); models that couple Archean photochemistry to a methanogenic ocean come close to this limit, with methane-to-hydrogen ratios of 2 to 45 in the air, limited by the rate of gas transfer into the ocean (Kharecha et al., 2005), against one half here. All hydrogen above the cold trap is then methane-borne, with $f_T = 2f_{\mathrm{CH_4}}$ and $E_{\mathrm{H}} = k_{\mathrm{esc}}N$ as in Claire et al. (2006); half of the methane destroyed is regenerated by the methanogens, the escape term of (S2) becomes $\frac{1}{2}k_{\mathrm{esc}}N$, and the same loss of reducing power then requires twice as much methane in the air. We integrate the model under both assumptions in Section S1.3; the two Archean methane levels differ by a factor of two, and no glaciation date shifts by more than 2.7 Myr between them.

The prescribed crossing epoch $t_\times$ is the age at which the declining reductant supply $R + 2G$ falls to the level of the marine organic burial B_{mar} (equation (3) of the main text); the redox budget of the anoxic atmosphere before $t_\times$, in which hydrogen escape carries the whole excess of the reductant supply over burial, is given in Section S1.3. Prescribing $t_\times$ fixes the Archean amplitude of the hydrogen-fed methane source at $G_A = 1.64$ Tmol CH_4 yr^{-1}, equivalent to a hydrogen supply of 6.56 Tmol H_2 yr^{-1}, which is 0.49 standard deviations above the modern volcanic hydrogen flux of Holland (2002), 4.8±3.6 Tmol H_2 yr^{-1}. Two quantities follow directly from k_{esc} and the rate surface and are not independent results: the methane-borne escape $k_{\mathrm{esc}}N$ is 0.997 of $2\Phi_0 f_{\mathrm{CH_4}}$ at every instant, the ratio of the rounded $k_{\mathrm{esc}}N_{\mathrm{atm}} = 6660$ to $2\Phi_0 = 6680$ Tmol yr^{-1}, and the modern methane lifetime $N/(\Omega + k_{\mathrm{esc}}N)$ is 8.8 yr, which corresponds to the modern calibration point of Claire et al. (2006).

Archean methane has left no direct rock record, and the model's methane can therefore be compared only with other models and with one indirect archive, atmospheric xenon. While the nickel series is at its plateau, at ages older than 2.7 Ga, the model air holds 279 ppmv of methane (Section S1.3), at the low end of published Archean estimates (Catling and Zahnle, 2020) and 0.68 of the 409 ppmv that the atmosphere–ecosystem model of Kharecha et al. (2005) gives at the same net hydrogen input. Under the opposite assumption about the photochemical hydrogen, which is nearer the one made by Kharecha et al. (2005), the plateau methane of our model is 1.36 times theirs. Methane falls with the nickel-dated hydrogen supply to 4.4 ppmv on the eve of the first glaciation (8.8 ppmv under that opposite assumption, the methane-only case of Section S1.3) and stays below 0.026 ppmv after the transition, so methane-borne hydrogen escape effectively ends with the methane collapse. If the hydrogen that the model counts as lost under the ice (Section S1.8) escapes to

space, loss continues through each glaciation at roughly the subaerial reductant flux. Xenon isotopes were still evolving late in the Archean and had reached their modern composition by the middle Paleoproterozoic (Avice et al., 2018), which Zahnle et al. (2019) interpreted as hydrogen escape "preceding and ending with" the Great Oxidation, xenon leaving as an ion dragged by hydrogen at a total mixing ratio above about one percent. In the model, too, hydrogen escape ends with the Great Oxidation, but the model's total hydrogen on the plateau, $f_T = 1.1 \times 10^{-3}$ under either assumption, is a factor of 9 below the one percent those authors require, so either the late-Archean atmosphere held hydrogen the model does not contain, in the transient episodes they invoke, or the model's Archean methane is too low.

S1.3 The redox budget without free oxygen

Equations (S1) and (S2) are the budgets of two reservoirs, free oxygen and methane, and with no oxygen consumed by escaping methane they combine into one conservation law for the reducing power of the ocean–atmosphere system, measured in oxygen equivalents (two per mole of methane, minus one per mole of free oxygen),

$$\frac{d}{dt}\left(2N - n_{\mathrm{O}_2} O\right) = R + 2G - B_{\mathrm{net}} - E_{\mathrm{H}}, \qquad B_{\mathrm{net}} = B_{\mathrm{mar}} + B_{\mathrm{land}}\phi(O) - W_{\mathrm{ox}} O^{1/2}, \tag{S2a}$$

in which the terrestrial methane terms cancel. Volcanic and metamorphic gases add reducing power at the rate $R + 2G$, organic burial removes it at the rate B_{net} because burial leaves oxygen behind, and hydrogen escape removes it at the rate E_{H} of (S2d), which is $2k_{\mathrm{esc}}N$ under the assumption adopted here (Section S1.2): each methane molecule lost takes with it its own four hydrogen atoms and the four that water gives up in oxidizing its carbon. The oxidation Ω removes one mole of methane and two moles of oxygen together, and therefore cancels from (S2a).

While the air holds oxygen, the quasi-steady state of (S1) is $B_{\mathrm{net}} = R + 2\Omega$ with $\Omega \geq 0$, in which the oxygen supplied by net burial is consumed partly by the reductant flux and partly by methane oxidation. When $R > B_{\mathrm{net}}$ there is no such state: under (S1) the oxygen reservoir empties from its initial $O = 10^{-7}$ PAL in about 8.5 yr, and thereafter the part of the reductant flux that the oxygen from burial cannot consume, $R - B_{\mathrm{net}}$ in oxygen equivalents or $\frac{1}{2}(R - B_{\mathrm{net}})$ in methane equivalents, remains unoxidized. The model counts R as hydrogen (Section 2.2 of the main text), and hydrogen that meets no oxygen is available to the same methanogens that make G; we therefore add it to the methane source and hold oxygen at zero,

$$O = 0, \qquad \dot{N} = G + \tfrac{1}{2}\left(R - B_{\mathrm{net}}\right) - k_{\mathrm{esc}}N \qquad (R > B_{\mathrm{net}}), \tag{S2b}$$

which is equation (2′) of the main text. Equation (S2a) is unchanged, and the steady state of (S2b) is the anoxic balance of Claire et al. (2006), in which hydrogen escape carries off the excess of the reductant supply over burial,

$$k_{\mathrm{esc}}N = G + \tfrac{1}{2}\left(R - B_{\mathrm{net}}\right) = \tfrac{1}{2}\left(R + 2G - B_{\mathrm{net}}\right). \tag{S2c}$$

Before the nickel decline $R = R_A = 2.505$ (rounded to 2.5 in Table 1 of the main text and Table S2), $G = 1.64$ and $B_{\mathrm{net}} = N_A = 2.07$ Tmol yr^{-1}, so that the escape is 1.86 Tmol $\mathrm{CH_4}$ yr^{-1}, larger than the methane source G by the 0.22 Tmol yr^{-1} of excess hydrogen, and the air holds $N = 5.0 \times 10^4$ Tmol of methane, or 279 ppmv, of which 33 ppmv represent that excess. Routing the excess through the methane source adds no hydrogen to the budget (S2a) and affects only whether the excess is present in the air as methane or as molecular hydrogen before it escapes. The reductant flux falls below burial at 2.64 Ga; from then until the crossing epoch $t_\times$ the air holds the small amount of oxygen at which methane oxidation takes up the difference, $2\Omega = B_{\mathrm{net}} - R$, and after $t_\times$, when $B_{\mathrm{net}} > R + 2G$, oxygen accumulates.

In the numerical solution (S1), (S2) and (S2b) are integrated as one system, in which the oxidation term $\Omega = k_{\mathrm{eff}}\, n_{\mathrm{O}_2} O N$ is evaluated with a signed oxygen variable and, whenever that variable is below the lowest tabulated oxygen level, with k_{eff} at that level. Once the oxygen reservoir is empty that variable settles within a year at a small negative value of no physical meaning, about -2×10^{-13} PAL before the nickel decline and never below the solver's tolerance of -10^{-11} PAL, at which $2\Omega = B_{\mathrm{net}} - R$; the term $-\Omega$ in (S2) then equals $+\frac{1}{2}(R - B_{\mathrm{net}})$, so that (S2) coincides with (S2b). The value at which it settles is more than seven orders of magnitude below the lowest oxygen threshold used in this work (10^{-5} PAL), and we describe such states as oxygen-free.

Three alternative treatments of the hydrogen budget on the anoxic branch give Archean methane between 246 and 558 ppmv, on either side of the adopted 279 ppmv, and none of them moves the beginning or end of a glaciation by more than 2.7 Myr from the dates of Table 2 of the main text. The first, which has the largest effect, concerns the photochemical hydrogen of Section S1.2. If methanogens consume it, the escape terms of (S2), (S2b) and (S2c) are halved and $E_{\mathrm{H}} = k_{\mathrm{esc}}N$ in (S2a); the steady state (S2c) becomes $k_{\mathrm{esc}}N = R + 2G - B_{\mathrm{net}}$, the same hydrogen escape carried by methane alone, and the plateau air holds

558 ppmv of methane instead of 279 and no free hydrogen. The published atmosphere–ecosystem models lie near this limit: their methane-to-hydrogen ratios correspond to between 0.75 and 0.99 of the photochemical hydrogen returning as methane (Kharecha et al., 2005), or to plateau methane between 447 and nearly 558 ppmv here. Our integrations keep the escape assumption of Section S1.2, which is one limiting case; the alternative just described, with all escaping hydrogen carried by methane, is the other, called the methane-only case in the main text. Every quantity that depends on this choice is given under both cases, and no outcome of the comparisons with the rock record in Table 2 of the main text changes between them.

We repeated the integrations with the escape term halved, that is, with the photochemical hydrogen consumed by methanogens. The methane forcing is then larger by 0.66 $\mathrm{W\,m^{-2}}$ on the plateau and by 0.96 $\mathrm{W\,m^{-2}}$ at 2.6 Ga, and because the silicate-weathering balance sets the surface temperature, carbon dioxide falls until the decrease in its forcing offsets most of the added methane forcing. At $\nu = 0.715$ every glaciation begins and ends between 0.8 and 2.7 Myr later than in Table 2 of the main text, the permanence date 2.6 Myr and the first oxic air 0.3 Myr later. The interglacial oxygen medians change by less than 6 percent and the interglacial carbon dioxide minima by less than 0.3 times the pre-industrial level, and the third glaciation ends 22.4 instead of 20.7 Myr after the Gordon Lake bound. The number of glaciations changes with ν as it does under the adopted treatment: at the resolution of Section 2.4 of the main text the four-glaciation interval and its midpoint are unchanged, and integrations spaced 0.0025 apart in ν locate both of its edges one such step lower, at 0.70625 and 0.72125 against 0.70875 and 0.72375, with the width unchanged. At the correspondingly shifted midpoint the dates of Table 2 are recovered to within about 1.1 Myr. The differences from the adopted treatment are larger in the methane history itself: methane falls through the 8 ppmv of the sulfur criterion of Zahnle et al. (2006) (Section S3.2) at 2.458 instead of 2.475 Ga, still before deposition of every anomaly-bearing sample cluster that the model fails to match under that criterion, and through ten ppmv, 12 instead of 31 Myr before the first glaciation. At the onset of that glaciation methane still supplies 1.3 $\mathrm{W\,m^{-2}}$ of forcing, against 0.75 under the adopted treatment, so that the air enters the glaciation at 0.88 of the methane-free carbon dioxide threshold (against 0.93), and for the same reason a single first glaciation survives to $\nu = 0.839$ instead of 0.7975. Equation 14 of Claire et al. (2006) subtracts in addition one O_2 from the oxygen budget per escaping methane molecule where the air holds oxygen (Section S1.2); by the time oxygen appears methane has collapsed and this term, at most $k_{\mathrm{esc}}N$, is small beside the other terms of (S1), and the same integrations with it included move no date by more than 0.02 Myr.

The second alternative concerns the excess volcanic hydrogen itself: if it escaped as H_2 without being converted to methane, the escape flux and (S2a) would be the same, because the diffusion-limited flux (S2d) depends only on the total hydrogen mixing ratio, whichever molecule carries the hydrogen. Only the greenhouse forcing would then differ, with 33 ppmv of the Archean methane replaced by about 65 ppmv of radiatively inactive hydrogen. The third concerns R: if part of it were sulfur gases or dissolved ferrous iron, which the model does not represent, the unoxidized excess of that part would be buried in reduced form and would then drop out of the balance (S2a) altogether. We therefore also repeated the integrations with the excess counted as inert, that is, with $O = 0$ and $\dot{N} = G - k_{\mathrm{esc}}N$ on the anoxic branch, so that $k_{\mathrm{esc}}N = G$ and the Archean methane is 246 ppmv instead of 279. The inert and the adopted treatments differ only before 2.64 Ga, after which neither has any excess hydrogen, and the offset in CO_2 that compensated the difference in their methane greenhouse forcing then decays within a few silicate-weathering response times (Section S1.5). At $\nu = 0.715$ every glaciation of the inert treatment therefore begins and ends within about 12 yr of the dates in Table 2 of the main text, the permanence date is unchanged, and the date of first oxic air moves by 0.09 Myr. At the end points of the interval of Section 2.4 of the main text the inert treatment gives four glaciations by 2.22 Ga and one later at $\nu = 0.7075$, and four with none later at $\nu = 0.7225$. The adopted treatment gives the same numbers at the adjacent exponents 0.705 and 0.72 respectively, and the glaciation dates shift with ν in the same way, so that the four-glaciation interval is unchanged to within its resolution of 0.005.

Under ice the unoxidized reductant is treated differently (Section S1.8): it is counted as hydrogen lost to space and does not enter the methane reservoir. No oxygen or methane reaches the air through the ice, so that the subaerial reductant flux meets no oxygen at all, and it cannot reach the methanogens either, since they live below the ice and the cover that keeps their methane out of the air also keeps atmospheric hydrogen away from them. Counted as methane instead, that flux would add a methane greenhouse during the glaciations, which the venting fraction $\theta = 0$ excludes by assumption.

S1.4 Seafloor weathering

For seafloor weathering, the low-temperature alteration of ocean crust that precipitates carbonate in its pore space, we use the functional form and posterior parameter values of Krissansen-Totton and Catling (2017) as generalized by Krissansen-Totton et al. (2018). The flux depends on crustal production through the relative

heat flow Q, on seawater acidity through C, and on pore-water temperature through an Arrhenius factor,

$$F_{\mathrm{sfw}} = F_d\, Q(t)^b\, C^{\gamma/2} \exp\left[\frac{E_a}{R_g}\left(\frac{1}{T_{p,0}} - \frac{1}{T_p}\right)\right], \qquad Q(t) = \left(1 - \frac{t}{4.5\ \mathrm{Gyr}}\right)^{-n}. \tag{S5}$$

The modern flux $F_d = 0.459\ \mathrm{Tmol\,C\,yr^{-1}}$, the activation energy $E_a = 75\ \mathrm{kJ\,mol^{-1}}$ and the exponent $\gamma = 0.27$ are their posterior medians, and R_g is the gas constant. The pore-water temperature T_p is the deep-water temperature, $1.02\,T_s - 16.67$ K for surface temperature T_s, bounded below by the freezing point (271.15 K), plus a geothermal offset (9 K today) that scales with Q and sediment thickness; $T_{p,0}$ is its present value. We chose the spreading exponent $b = 1$, the early relative sediment thickness $f_{\mathrm{sed}} = 0.6$ and the heat-flow exponent $n = 0.73$ inside the ranges those authors sample, and the number of Paleoproterozoic glaciations does not depend on these three values. Under ice the surface temperature is at its lower bound and the deep water is at the freezing point; seafloor weathering continues at that temperature and removes about 10–11% of the sub-ice outgassing ($1.44\ \mathrm{Tmol\,C\,yr^{-1}}$ under the first glaciation). The outgassing law of the main text and (S5) both depend on the heat-flow history $Q(t)$, and the combination of exponents we use lies slightly outside the range that Krissansen-Totton et al. (2018) sample, since with $\nu = 0.715$ and $n = 0.73$ the implied ratio $m = \nu/n = 0.98$ is 2% below their sampled range $m \geq 1$. The exponent n enters only through Q in F_{sfw}, which under ice is about a tenth of the outgassing, and with $n = \nu$ ($m = 1$) the model still gives four glaciations, (4, 0) beginning before and after 2.22 Ga respectively.

S1.5 Carbon partition and the modern weathering flux

The factor β_w in (S3) is the ratio of the change in total ocean–atmosphere carbon to the accompanying change in atmospheric CO_2, both measured in units of the pre-industrial atmospheric inventory. The model has no dissolved-inorganic-carbon or alkalinity variable, and β_w stands in for the ocean's carbonate system near the present state. We fix β_w through a time scale, since a small CO_2 perturbation decays under (S3) with the e-folding time

$$\tau_{\mathrm{sil}} = \frac{n_{\mathrm{C}}\,\beta_w}{n_0\,W_0}, \qquad n_0 = \left.\frac{\partial \ln W_{\mathrm{sil}}}{\partial \ln C}\right|_{t=0} = 0.68, \tag{S6}$$

and τ_{sil} is set to 380 kyr, the slow end of the 170–380 kyr that Colbourn et al. (2015) find for the silicate-weathering feedback, which gives $\beta_w = 29.6$. We chose the slow end independently of the Paleoproterozoic glacial record, and the number and durations of the model's glaciations depend on this choice. At the central value, 240 kyr, the model at $\nu = 0.715$ produces six glaciations of 15–16 Myr before 2.22 Ga and one after it, although a shifted outgassing exponent again gives a glacial era resembling the recorded one (Section 4.5 of the main text; Supplementary Text S4). The e-folding temperature of silicate weathering in equation (7) of the main text, $T_e = 11.1$ K, is the Walker–Berner value tabulated by Graham and Pierrehumbert (2020); it lies inside the conventional range of 5–15 K and near the low end of the 10–40 K over which Krissansen-Totton et al. (2018) sample it. The number of glaciations also depends on this value, since at $T_e = 13.9$ K the model at $\nu = 0.715$ gives (6, 12) glaciations beginning before and after 2.22 Ga respectively. Over a range of T_e around the adopted value the model still reproduces the recorded glacial era at some other ν, fixed again by the number of glaciations (Section 4.5 of the main text and Supplementary Text S4).

The modern silicate-weathering flux $W_0 = 5.73\ \mathrm{Tmol\,C\,yr^{-1}}$ is fixed by the requirement that $C = 1$ today, $W_0 = V_{\mathrm{out}}(0) + W_{\mathrm{ox}} - B_{\mathrm{mar}}(0) - B_{\mathrm{land}}(0)\phi(1) - F_{\mathrm{sfw}}(0)$. This value lies inside the range 4.9–6.65 $\mathrm{Tmol\,C\,yr^{-1}}$ that long-term carbon-cycle models use on a carbonate-burial basis (Berner and Kothavala, 2001), and at about half (0.49) of the 11.7–12 $\mathrm{Tmol\,C\,yr^{-1}}$ of silicate CO_2 consumption computed from river chemistry (Gaillardet et al., 1999). We do not use W_0 as a test of the model, because the requirement $C = 1$ determines it from the modern outgassing V_{mod}, which we take from within its published range, and from fluxes already set to their modern values.

S1.6 Radiative forcing and the glaciation thresholds

The forcings $F_{\mathrm{CO_2}}(C)$ and $F_{\mathrm{CH_4}}(p_{\mathrm{CH_4}})$ of equation (8) of the main text are interpolated in the logarithm of abundance from the tabulated line-by-line values that Byrne and Goldblatt (2014) computed for an anoxic atmosphere with 1 bar of nitrogen, relative to their references of 278 ppmv of CO_2 and 0.715 ppmv of CH_4. We use no CO_2–CH_4 overlap term, which they find minimal, and no N_2O. At methane abundances below the reference value the tables give small negative forcings, at most about 0.84 $\mathrm{W\,m^{-2}}$ in magnitude at the methane levels the model reaches; we set these to zero, so that a methane-free atmosphere is compared with the glaciation threshold without subtracting the forcing of the absent pre-industrial methane. The absorbed sunlight today is $Q_\odot = 238.17\ \mathrm{W\,m^{-2}}$, the solar luminosity is $s(t) = [1 + \frac{2}{5}\,t/(4.57\ \mathrm{Gyr})]^{-1}$ (Gough, 1981), and the climate sensitivity $\lambda = 0.69$ K per $\mathrm{W\,m^{-2}}$ of equation (7) of the main text is 3 K per doubling of

CO_2 on these tables. We assume a nitrogen inventory near one bar. On the same authors' half-bar tables the model at $\nu = 0.715$ gives five glaciations before 2.22 Ga and ten after it; the range of nitrogen inventory compatible with the glacial record is given in Section 4.5 of the main text.

The glaciation threshold $D^* = 10.1\ \mathrm{W\,m^{-2}}$, held constant, is the forcing deficit below the present pre-industrial state at which the atmosphere–ocean general circulation model of Voigt et al. (2011) with low-latitude Marinoan continents passes into a snowball. It is the lowest of the published thresholds and therefore the most favorable to glaciation; the same model with modern continents and two other general circulation models put the transition at 17.9, 21.4 and 30.2 $\mathrm{W\,m^{-2}}$ (Voigt et al., 2011; Yang et al., 2012), and a model of intermediate complexity traced through Earth history implies 15.8 $\mathrm{W\,m^{-2}}$ for the early Paleoproterozoic (Feulner et al., 2023). At 15.8 $\mathrm{W\,m^{-2}}$ the model has no glaciation at $\nu = 0.715$, and above 14.7 $\mathrm{W\,m^{-2}}$ no value of ν gives a glacial era resembling the recorded one (Section 4.5 of the main text). Teitler et al. (2014) simulated the onset of low-latitude glaciation under Paleoproterozoic boundary conditions (reduced CO_2, enlarged continents, a collapsing methane greenhouse) in a general circulation model; their experiments are not on the scale of those thresholds, and we extract no value of D^* from them. An equivalent statement of the threshold is the methane-free CO_2 level $H(t)$ at which $F_{\mathrm{CO_2}}(H) = [1 - s(t)]Q_\odot - D^*$, which is 72 times pre-industrial at the first glaciation and falls as the Sun brightens. With methane present the open-water branch persists at CO_2 levels below H. In the model methane falls from 279 to ten ppmv by 2.482 Ga, 30.5–31.9 Myr before the first glaciation over the values of ν consistent with the rock record, and that glaciation begins when the forcing of the last 2.1 ppmv is lost while CO_2 stands at 0.93 of H (Section S4.4). These values hold under the escape assumption of Section S1.2; in the methane-only case of Section S1.3, at $\nu = 0.715$, methane falls to ten ppmv 12 Myr before the first glaciation, which begins when the last 3.8 ppmv of methane are lost while CO_2 stands at 0.88 of H. That route to glaciation was proposed on photochemical grounds by Pavlov et al. (2000), Kopp et al. (2005), Zahnle et al. (2006) and Claire et al. (2006) (see also Bekker and Kaufman, 2007; Haqq-Misra et al., 2008), and is reviewed by Catling and Zahnle (2020).

Deglaciation requires a separate threshold, because under ice the surface albedo is that of a snowball. We take that threshold from the simulations of Abbot et al. (2012), six general circulation models with surface albedo 0.6 at 0.94 of present insolation, in which clouds bring the CO_2 needed to melt a snowball down to the 0.01–0.1 bar that the geochemical proxies allow (Hoffman et al., 2017). The ice persists until the CO_2 forcing above the deglaciation level, together with any methane forcing, makes up the deficit in absorbed sunlight relative to those simulations,

$$r\,[F_{\mathrm{CO_2}}(C) - F_{\mathrm{CO_2}}(C_X)] + F_{\mathrm{CH_4}}(p_{\mathrm{CH_4}}) \;\geq\; [s_{\mathrm{cal}} - s(t)]\,Q_{\mathrm{ice}}. \tag{S7}$$

Here C_X is the deglaciation level $X = 0.01$ bar in pre-industrial units (36), $s_{\mathrm{cal}} = 0.94$, and $Q_{\mathrm{ice}} = 136.1\ \mathrm{W\,m^{-2}}$ is the sunlight a snowball absorbs today at albedo 0.6. The factor $r = 0.686$ rescales the CO_2 forcing of the tables to the amplitude of the snowball models, 40 $\mathrm{W\,m^{-2}}$ across the CO_2 range of their suite against 58.3 in the tables. The older the epoch, the fainter the Sun relative to the calibration and the more CO_2 above X the thaw requires, about 280 times pre-industrial (0.08 bar) during the first glaciation. Two quantities in (S7), the deglaciation level X and the amplitude r, are assumptions that affect the number of glaciations. We set X at the low end of the proxy range independently of the Paleoproterozoic glacial record; at 0.028 bar, near the geometric midpoint of that range, the model at $\nu = 0.715$ produces three glaciations, and at its upper end two. The amplitude r is that of the snowball models; with the tables' full amplitude the model produces five glaciations, and with a log-linear slope fitted to the same simulations three.

S1.7 Alternative laws for the post-crossing reductant sink

The form given to the reductant sink after $t_\times$ in equation (4) of the main text is one of four alternatives, each of which we integrated in full (Table S4). The alternatives are a continuation of the nickel proxy after $t_\times$, a sink proportional to outgassing that declines on the linear mantle-redox trend of Kadoya et al. (2020b), a sink in constant proportion to outgassing, and the isotope law of equation (4) itself, in which the sink equals the net organic burial implied by the carbonate-isotope mass balance. We fixed the selection criterion before integrating the alternatives: the adopted law must give carbonate $\delta^{13}C$ after $t_\times$ consistent with the carbonate isotope record and a modern net organic burial consistent with the isotope mass balance. The isotope law satisfies the criterion by construction, because its sink is computed from the same carbonate $\delta^{13}C$ record, and for that reason we do not use its agreement with that record after $t_\times$ as support for the model. Each of the other three also has an outgassing exponent at which four glaciations occur, and each then gives a modern carbonate $\delta^{13}C$ several per mil below the measured Phanerozoic mean and a modern net burial below the range allowed by the isotope mass balance. The glacial durations are nearly the same under all four laws, each at its own exponent (Table S4), and the choice of sink law determines instead the oxygen level and the carbon isotopes after the transition.

Table S4: The four laws integrated for the oxygen-independent reductant sink after the crossing epoch $t_\times$, each at the outgassing exponent ν at which it gives four Paleoproterozoic glaciations, with the two quantities of the selection criterion: modern carbonate δ^{13}C against the Phanerozoic mean of Krissansen-Totton et al. (2015), 1.75 ± 0.19 per mil, and modern net organic burial against the 1.50–2.15 Tmol C yr^{-1} that the isotope balance allows at the model's outgassing. Only the isotope law meets the criterion, which it does by construction because its sink is derived from the same isotope record. Durations are the range over the four glaciations; "first oxic air" is the age at which the model air first exceeds 10^{-5} PAL.

Sink law after $t_\times$	ν	δ^{13}C today (per mil)	net burial today (Tmol C yr^{-1})	durations (Myr)	first oxic air (Ga)
Isotope law, $S = f_{\mathrm{org}} V_{\mathrm{out}}$ (adopted)	0.715	1.72	1.82	23.6–25.7	2.353
Nickel proxy continued	0.9725	−4.11	0.24	24.8–26.5	2.426
Linear mantle-redox trend (Kadoya et al., 2020b)	0.96	−3.10	0.51	24.0–25.6	2.424
Constant proportion to outgassing	0.8425	−0.60	1.19	23.7–25.5	2.413

Because the adopted sink is computed from the carbonate δ^{13}C record, every carbonate δ^{13}C after $t_\times$ and the modern net burial are inputs to the model and are reproduced by it. The Proterozoic oxygen level is then set by the difference between the marine burial, which stays at its Archean value N_A, and the declining sink $S(t)$, with no redox feedback. Burial and sink become nearly equal in the Tonian when the δ^{13}C of the input carbon ($\delta_{\mathrm{in}} = -5 \pm 1$ per mil) is taken at the heavy end of its range, and the model air then dips briefly below the sulfur-isotope threshold. Under the adopted law the reductant sink is tied to two different dated records, the nickel proxy before $t_\times$ and the carbonate isotope record after it, joined at the transition that the nickel-dated decline produces. The reductant consumed per unit of outgassed carbon falls with the nickel-dated decline before $t_\times$ and rises with the organic burial fraction after it, and its minimum therefore lies at the join of the two laws (0.36 mol O_2 per mol C on the Archean plateau, 0.15 at $t_\times$, 0.23 today). We do not identify the physical carriers of the reductant flux after $t_\times$; among the candidates, recycled crustal reducing power is expected to grow with time relative to outgassing, as the adopted law requires, whereas the contributions of the cooling mantle and of hydrothermal systems decline.

S1.8 Carbon, oxygen and methane under the ice

During a glaciation we treat the ocean surface as capped by ice. The oxygen and methane that sub-ice production would supply are multiplied by a venting fraction θ, which we set to zero, corresponding to complete consumption of both gases below the ice. The oxygen-consuming terms of (S1) act only on the oxygen present, with kerogen oxidation and marine burial at 0.25 of their open-water rates; reductant in excess of the available oxygen is assumed to leave as hydrogen, which the model counts as lost rather than as methane (Section S1.3 gives the open-water counterpart), and the methane remaining in the air decays by hydrogen escape. The air under every glaciation is therefore anoxic and methane-free by assumption. The anoxia does not depend on the venting fraction: beneath the ice marine burial could supply at most $\beta_B B_{\mathrm{mar}} = 0.52$ Tmol O_2 yr^{-1} to the air (with $\beta_B = 0.25$ the sub-ice burial factor), whereas the reduced gases continue at $R = 0.55$–0.57 Tmol yr^{-1} and the hydrogen-fed methane source at $G = 0.72$–0.75 Tmol CH_4 yr^{-1} during the glacial era, so that the vented mixture is net reducing for any θ. That conclusion holds as long as sub-ice burial stays well below its open-water rate, and the ratio of the two rates, $\beta_B = 0.25$, is an assumption of the model. With $\theta = 0.01$ and 0.03 the air during the glaciations holds less than 4×10^{-13} PAL of oxygen and at most 0.75–2.3 ppmv of methane, the date of first oxic air moves by less than 0.3 Myr and each glaciation shortens by up to 2.5 Myr. The four glaciations do not require the cap to be complete, since with venting fractions of 0.01 and 0.03, and in a variant in which methane is consumed in the water column first, the numbers of glaciations beginning before and after 2.22 Ga are (4, 0), (4, 0) and (4, 0) respectively.

In the sub-ice carbon budget, equation (9) of the main text, seafloor weathering removes about 10–11% of the outgassing, and the reduced sub-ice burial and kerogen oxidation are omitted. A fraction $1/\beta_{\mathrm{ice}} = 3.4\%$ of the remainder accumulates in the air, which gains CO_2 at 8.4 times pre-industrial per Myr under the first glaciation, and the rest, 96.6%, is withheld from the air, returned to the ocean–atmosphere system at the thaw and then removed by silicate weathering over the following interglacial. Table S5a gives the resulting carbon budget of the first glaciation. Of the 3.6×10^{20} mol of carbon outgassed in 25.7 Myr, cold seafloor weathering removes 0.4×10^{20} mol and 0.1×10^{20} mol stays in the air, which holds 0.08 bar of CO_2 at the deglaciation; the remaining 3.1×10^{20} mol, 99 times the dissolved inorganic carbon of the present ocean (3.16×10^{18} mol), is stored and returned, and across the four glaciations the store is 84–99 ocean inventories. Over the following interglacial the carbon sinks of (S3), chiefly silicate weathering, remove 21.2 Tmol C yr^{-1} on average against an outgassing of 13.8, and the difference, 7.4 Tmol C yr^{-1}, consumes the returned carbon in 43.4 Myr.

Because the model has no dissolved-inorganic-carbon or alkalinity variable, the size of the sub-ice carbon store is not derived from seawater chemistry. It follows from setting β_{ice} equal to the warm partition $\beta_w = 29.6$ and applying that partition unchanged to an ice-covered ocean under as much as 281 times more CO_2. The warm partition is the carbonate-compensated response of the modern ocean–atmosphere system near one pre-industrial atmosphere of CO_2, fixed through the 380-kyr weathering response time (Section S1.5). Seawater chemistry alone would store much less carbon: an ocean of fixed alkalinity in equilibrium with the sub-ice atmosphere takes up 5×10^{18} mol, 1.7% of the store ($\beta_{\mathrm{ice}} = 1.34$–$1.52$), and seawater held at carbonate saturation gives β_{ice} between 4.5 and 2.7 over the sub-ice range of CO_2. Held as bicarbonate, the store would raise dissolved inorganic carbon by 0.22 mol kg^{-1} and would require at least 0.22 eq kg^{-1} of new alkalinity, 95 times that of the modern ocean (0.44 eq kg^{-1} if dissolving carbonate supplies it, since each carbonate ion dissolved adds a carbon atom of its own), delivered under the ice while continental weathering is shut off. We considered four carriers that might hold a store of this size and return it at the thaw. (i) Dissolution of shelf carbonate ($CaCO_3 + CO_2 + H_2O \rightarrow Ca^{2+} + 2HCO_3^-$) would store one outgassed CO_2 per carbonate dissolved and release it again when the carbonate re-precipitates after the thaw, which is the exchange the model assumes. It would require, however, 3.1×10^{20} mol of carbonate per glaciation, 1.1×10^7 km^3 or 760 m over the 15×10^6 km^2 of shelf that Le Hir et al. (2008a) adopt, which is twenty times the largest sub-glacial dissolution those authors could justify for a Neoproterozoic ocean (1.5×10^{21} g, or 35 m over the same area). In the early Paleoproterozoic there was no pelagic carbonate to draw on, the platforms were exposed by the glacial fall in sea level, and the same mass would have to be redeposited after each of the four thaws. Paleoproterozoic cap carbonates are known, but none on that scale has been described. (ii) Cations released by the sub-ice alteration of seafloor basalt, which Hoffman et al. (2017) describe as "a sink for CO_2 and a source of alkalinity", are taken up by carbonate precipitated within the crust once the pore waters saturate, so that the net alkalinity flux to the ocean is close to zero and the carbon does not return (Le Hir et al., 2008a). Mills et al. (2011) nevertheless assumed an exchange of this kind, with return at the thaw, in their model of Neoproterozoic glacial cycling. (iii) In the carbon–alkalinity model of Le Hir et al. (2008b,a) the sub-ice ocean acidifies to a pH near 6 and low-temperature alteration of the ocean crust rises until it consumes the whole outgassing flux; 18% of the outgassed carbon is airborne after 30 Myr (0.26 bar) and the rest is sequestered permanently. It is the one published mechanism of the required capacity, and it does not return the carbon; the seafloor-weathering law we use (Krissansen-Totton et al., 2018) has no dependence on seawater pH and removes only a tenth of the outgassing under ice, a factor of about ten below the uptake of that mechanism. (iv) CO_2 ice, which Hoffman et al. (2017) note cannot be dismissed for an early Paleoproterozoic glaciation under the fainter Sun, would return to the air at the thaw, but its capacity has not been quantified. We therefore have no carrier for an exchangeable store of this size, and the store remains, with the glaciation threshold and the nitrogen inventory, the model's largest physical assumption. The only empirical support for the store is the dated Marinoan duration (below), and that check constrains the deglaciation level X and β_{ice} only in combination.

The uptake of carbon by the store under the ice and its return at the thaw control different features of the model chronology (Table S5b). The amount withheld from the air under the ice sets the glacial duration but hardly affects the rest of the chronology: with the uptake efficiency of Le Hir et al. (2008a) ($\beta_{\mathrm{ice}} = 5.55$, 18% airborne) and deglaciation at $X = 0.1$ bar the glaciations last about 23 Myr whether or not the carbon returns, with a carbonate-saturated partition at that X about 10 Myr, and with a fixed-alkalinity ocean and no other carrier 1.2–1.3 Myr. The amount returned at the thaw sets the length of the interglacials, and with it the spacing of the glaciations, their number at a given ν, the value of ν fixed by the glaciation count, the date of the last deglaciation and the CO_2 level after each thaw.

We integrated the model with the crustal carrier, mechanism (iii), under which the carbon taken up beneath the ice, at the efficiency of Le Hir et al. (2008a), stays in the ocean crust. With this carrier we set the deglaciation level at $X = 0.1$ bar in (S7), at which the thaw comes at 0.30 bar of CO_2 under the Sun of that age (0.08 bar with the adopted $X = 0.01$ bar), and only the airborne excess and the equilibrium share of a fixed-alkalinity ocean return at the thaw (7.6×10^{19} mol per glaciation returned, 2.1×10^{20} mol sequestered). For that case we repeated the sweep of the outgassing exponent, with 20 integrations at exponents 0.005 apart and 0.0025 apart wherever the number of glaciations changes. The Paleoproterozoic glacial era still comes to an end, and as ν rises the number of glaciations again decreases one at a time, the youngest glaciation being lost first: five begin by 2.22 Ga below $\nu = 0.716$ (with a sixth, later one below 0.706), four with a fifth after 2.22 Ga between 0.716 and 0.719, four with none later for $\nu = 0.719$–0.732 (with the adopted store 0.7075–0.7225), three for 0.732–0.744 and two or fewer above. At $\nu = 0.725$, the middle of that four-glaciation interval, the glaciations last 22.5–23.1 Myr, the interglacials shorten from 43.4–48.8 to 33.0–38.9 Myr and the spacing from 68.3–72.9 to 56.2–61.6 Myr. At each thaw the returned carbon, most of it the airborne excess, is divided between air and ocean by the warm partition β_w (Section S1.5), so that CO_2 falls from 1083 times pre-industrial under the ice to 119 immediately after the first thaw (114 one Myr later, Table S5c), against 281 with the adopted store, and then to 56–66 before the next glaciation. Section S1.9 gives the carbon

and alkalinity budget of the re-partition at the thaw and the chronology that results when that re-partition is spread over time. Oxic air first appears 13 Myr after the second deglaciation, at 2.358 Ga, and the first interglacial stays anoxic; oxygen becomes permanent at the last thaw, 2.252 Ga, and the oxygen level after the glacial era is about a tenth higher than with the adopted store.

Because the interglacials are shorter under the crustal carrier, the model chronology in that case meets a different subset of the dated bounds (Table S5c). The span from the first deglaciation to the third is 113.6 Myr, within the 114.1 Myr that separate the MAK-D diamictite age from the Gordon Lake bound (135.8 Myr with the adopted store), so that the third glaciation ends at 2.313 Ga, 3.3 Myr inside the bound that the adopted case misses by 20.7 Myr. The last deglaciation, whose date follows from the glaciation count as in the adopted case, falls inside the Hekpoort window. However, the fourth glaciation begins at 2.2745 Ga, 12.5 Myr before the upper Timeball Hill tuffs allow, the open interval before it lasts 38.9 Myr whereas the Timeball Hill shale requires at least 48 Myr, and the first glaciation ends 2.8 Myr before the MAK-D age (1.0 Myr with the adopted store). The spacing lengthens toward the upper edge of the interval, and at $\nu = 0.73125$ the third glaciation ends 2.0 Myr after the Gordon Lake bound, the fourth begins 5.4 Myr after the upper Timeball Hill bound with 51.4 Myr of open water before it, and the last deglaciation is at 2.234 Ga. That integration meets the Ongeluk age (at 2σ), the upper Timeball Hill tuffs, the 48-Myr open interval and the Hekpoort window together, which no integration with a returned store does at the climate assumptions of the main text (Supplementary Text S4), and misses the Gordon Lake and MAK-D ages by 2.0 and 2.5 Myr; its first oxic air, at 2.360 Ga, is still 8 Myr later than the Kaapvaal sulfur record allows under the oxygen-only criterion. Between these two members, at $\nu = 0.730$, the third glaciation ends 0.8 Myr after the Gordon Lake bound and the fourth begins 1.0 Myr before the upper Timeball Hill bound, with 46.2 Myr of open water before it, so that no member of the interval meets both bounds. The 20.7-Myr Gordon Lake discrepancy of the main text therefore depends on the returned store as much as on the smooth outgassing law, because it reflects the length of the interglacials, and that length is set by the amount of carbon returned at each thaw.

We keep the returned store as the principal case and give the chronology under the crustal carrier beside it, at the middle and near the upper edge of its four-glaciation interval (Table S5b–c; Table 3 of the main text). The change of carrier leaves the number of glaciations and their durations nearly unchanged but moves their dates, because the dates are set by how much carbon returns at each thaw and by the warm partition applied to that carbon. Under neither carrier does the model chronology meet every dated bound at one value of ν. With the returned store it misses the Gordon Lake bound, with the crustal carrier at mid-interval it meets that bound and misses the upper Timeball Hill tuffs and the open interval instead, and with the crustal carrier near the upper edge of its interval it meets those bounds and the Hekpoort window and misses the Gordon Lake and MAK-D ages by 2.0 and 2.5 Myr; in all three cases oxic air first appears later than the Kaapvaal sulfur record allows. We retain the returned store as principal because the crustal case sets the deglaciation level at the top of its proxy range instead of the bottom and adds a rule for the share of the sub-ice carbon returned at the thaw, a share that it re-partitions between air and ocean at once (Section S1.9). We do not count the closer agreement of the crustal member near the upper edge of its interval with the dated beds for or against either case: if the Gordon Lake, upper Timeball Hill and Hekpoort ages were used to place ν there, those ages would join the glaciation count as calibration data, and we would then report them as calibration rather than as tests. With no carrier beyond a fixed-alkalinity ocean, and everything returned, the model becomes a fast oscillator, with twelve glaciations of 1.2–1.3 Myr separated by 11–30 Myr beginning by 2.22 Ga at $\nu = 0.715$ and one later, which the glacial record excludes at that exponent. The interglacials do not vanish when little carbon returns, because most of an interglacial is spent close to the glaciation threshold, where the net carbon sink is small and the approach is paced by the warm partition β_w. That partition is fixed by the modern state (Section S1.5), and a smaller value at high CO_2 would shorten the interglacials further; Section S1.9 gives the chronology under the partition of calcite-saturated seawater.

We integrated one other sub-ice rule, in which a fixed fraction 1.7% of the sub-ice outgassing, the fraction that reproduces the dated Marinoan duration under the model's thresholds, accumulates in the air. Because atmospheric CO_2 is continuous through the thaw and the warm branch then obeys (S3) with β_w, this rule leaves the same exchangeable inventory to the interglacial as the adopted one (3.2×10^{20} mol removed after the first thaw). It differs from the adopted rule only in the slower accumulation of CO_2 in the air under the ice, which lengthens the glaciations to 41–44 Myr while the interglacials stay at 43–45 Myr. With glaciations that long only three begin by 2.22 Ga at $\nu = 0.715$, and lowering ν adds a glaciation younger than 2.22 Ga before it adds a fourth one older than that age. The number of Paleoproterozoic glaciations is still below four at $\nu = 0.69$, and at $\nu = 0.685$ the number of glaciations of all ages already exceeds four, so that under the isotope sink law no exponent gives four with none later. Under the nickel-proxy sink of Table S4 there is such an exponent, $\nu = 0.955$, with glaciations of 36–39 Myr, but that sink fails the isotope criterion. We adopted the rule of equation (9) over this one by a criterion fixed before either was integrated: the Marinoan duration it implies must fall inside the dated range, and some exponent must give four Paleoproterozoic glaciations

with none later. The second condition uses the glacial record, so that the glaciation count calibrates the sub-ice rule together with ν, and the four-glaciation interval of the main text is conditional on Marinoan-scale sub-ice uptake; where that interval lies in ν depends on how much of the carbon returns at the thaw (Table S5b–c).

The parameters of (S7) and of the sub-ice budget with the exchangeable store were not adjusted to the Cryogenian glaciations; the Marinoan duration entered only as one of the two conditions under which we adopted that store. When we apply the same entry, exit and seafloor-weathering laws at the Marinoan, with the glaciation beginning at the midpoint of the dated range for its onset (644.5 Ma), the model gives a duration of 5.1 Myr against the dated 4–15 Myr (Hoffman et al., 2017). The model Marinoan deglaciates at 31 times pre-industrial CO_2 (0.0085 bar), just below the proxy range, because at that age the Sun is brighter than in the calibration of (S7). This Marinoan comparison is a single check and does not determine the pair $(X, \beta_{\mathrm{ice}})$, since at $X = 0.01$ bar every β_{ice} from 23 to 86 reproduces the dated duration. Under the same laws the model Sturtian lasts 5.3 Myr against the dated 57–59 Myr (Hoffman et al., 2017); the Sturtian is thus not reproduced, and no single value of β_{ice} fits the durations of both Cryogenian glaciations.

Within the family of stores returned at the thaw, the Paleoproterozoic chronology depends on how much carbon is stored per glaciation more than on where the deglaciation level X is set within its proxy range. At $X = 0.1$ bar with the uptake efficiency of Le Hir et al. (2008a,b) but the store still returned, the model again gives four glaciations of about 23 Myr over the same interval of ν as in the main text, and a Marinoan of 11.1 Myr; a partition computed instead from carbonate-saturated seawater chemistry at that X (the calcite-saturation partition of the main text) shortens the glaciations to about 10 Myr and gives four of them at $\nu = 0.7325$. Across these combinations the durations vary by a factor of about 1.3, and by about 2.5 when the calcite-saturation partition is included (the individual simulations are listed in Supplementary Text S4); the crustal-carrier case lies outside this family because it returns less carbon than it withholds, and the fixed-alkalinity case because it withholds almost none.

S1.9 Carbon and alkalinity through deglaciation

The model has no dissolved-inorganic-carbon or alkalinity variable, so the division of carbon between air and ocean at a deglaciation is prescribed by the partition rule of each storage case. Under the adopted store the sub-ice and open-water partitions are the same number, $\beta_{\mathrm{ice}} = \beta_w = 29.6$: a share $1/\beta_w$ of the net sub-ice input accumulates in the air, the rest is assigned to the ocean side of the exchangeable reservoir, atmospheric CO_2 is continuous through the thaw (281 times pre-industrial at the first deglaciation), and the sinks of (S3) then remove the whole inventory over the following interglacial. Nothing is transferred between air and ocean at the thaw itself (the store is returned in the sense that the open-water sinks act on the whole exchangeable inventory from then on), and the open question for this case is the carrier of the store (Section S1.8). Under the crustal carrier the carbon taken up beneath the ice stays in the crust, and at the thaw the exchangeable carbon is the airborne excess together with the equilibrium share of a fixed-alkalinity ocean, 7.6×10^{19} mol at the first deglaciation; the model applies the open-water partition β_w to that carbon at once, so that CO_2 falls from 1083 to 119 times pre-industrial. This step moves 4.8×10^{19} mol of carbon, 89% of the airborne CO_2 and 15 times the dissolved inorganic carbon of the modern ocean, out of the air instantaneously (Table S5d).

Seawater by itself cannot take up the carbon that leaves the air at the crustal thaw, because before the thaw the ocean already holds its equilibrium share at fixed alkalinity, 2.54×10^{19} mol of dissolved CO_2. To hold a further 4.8×10^{19} mol as bicarbonate it would have to gain 35 mmol kg^{-1} of dissolved inorganic carbon (for an ocean of modern mass) and 4.8×10^{19} eq of alkalinity, 15 times the modern ocean's inventory; if dissolving carbonate supplied that alkalinity, one $CaCO_3$ per CO_2 taken up (9.6×10^{19} eq, each carbonate bringing a carbon of its own), 119 m of carbonate would have to dissolve over the 15×10^6 km^2 of shelf of Le Hir et al. (2008a), against the 35 m those authors could justify beneath the ice. Warming at the thaw acts in the opposite sense, since the solubility of CO_2 falls and saturated seawater precipitates carbonate. In carbon–alkalinity models of the glacial aftermath the excess CO_2 therefore leaves the air by a different route: silicate weathering under the hot, CO_2-rich climate delivers cations, carbonate is buried, and carbonate weathering restores the saturation of the ocean within about 20 kyr of the thaw (Le Hir et al., 2008a). Le Hir et al. (2008a) obtain a silicate-weathering flux 7 times the present one after a Neoproterozoic deglaciation at 0.26 bar of CO_2 and a return toward the pre-glacial level in about 3 Myr, whereas Higgins and Schrag (2003) had assumed higher weathering rates and a return in about 200 kyr. With a general circulation model driving a mechanistic weathering model, Le Hir et al. (2009) find that runoff hardly increases, that the weathering flux is at most about 10 times the modern one, and that CO_2 falls from 400 to about 70 times its present level within the first Myr in their preferred soil case, the recovery taking a few Myr. Hoffman et al. (2017), following Mills et al. (2011), put the further decline to the threshold for polar ice at about 10^7 yr, which in our model is the interglacial itself. At 7 times the present-day consumption of CO_2 by silicate weathering that Le Hir et al. (2008a) adopt, 6.8 Tmol C yr^{-1}, the 4.8×10^{19} mol moved out of the air at the

crustal thaw would be removed in 1.0 Myr, and their peak post-glacial carbonate-weathering flux of about 2.1×10^{14} mol yr^{-1}, at one $CaCO_3$ dissolved per CO_2 taken up, would deliver the alkalinity to hold it as bicarbonate in 0.23 Myr. The instantaneous re-partition is thus a stand-in for a drawdown that takes 10^5 to a few times 10^6 yr in these carbon–alkalinity models, short beside the model's interglacials of 33.0–38.9 Myr. It differs from that drawdown in keeping the returned carbon in the exchangeable reservoir, to be removed over the whole interglacial by weathering at about 119 times pre-industrial CO_2 and below (a mean net sink of 2.3 Tmol C yr^{-1}), whereas weathering during a hothouse of finite length buries part of that carbon at once.

We integrated two variants of the crustal case to find how the chronology depends on the treatment of the thaw (Table S5e; 57 integrations in all, on the ν grid of Section S1.8 refined to half its step near the edges and midpoints of the intervals below, and including those of the adopted rule under the second variant's partition). In the first variant the re-partition is spread over a finite time after each thaw. The effective partition of the exchangeable carbon then relaxes from its value at the thaw, $r_0 = 1.5$ (the airborne excess plus the ocean's dissolved share, divided by the airborne excess), to β_w with an e-folding time τ,

$$\beta_{\mathrm{eff}}(t) = \beta_w - (\beta_w - r_0)\, e^{-(t-t_{\mathrm{thaw}})/\tau}, \qquad C = C_{\mathrm{entry}} + S/\beta_{\mathrm{eff}}, \tag{S8}$$

where S is the exchangeable inventory above the state at glacial entry and obeys (S3) with the sinks evaluated at the actual CO_2; $\tau \to 0$ recovers the instantaneous rule, and an integration with $\tau = 1$ kyr reproduces its glacial dates to 0.02 Myr. The airborne share $1/\beta_{\mathrm{eff}}$ relaxes faster than β_{eff}, with an e-folding time of $0.083\,\tau$ from the uptake alone, and the model's silicate-weathering law removes airborne CO_2 faster still, since it has no runoff limit and reaches 64 times W_0 at 1083 times pre-industrial CO_2 (8 times W_0 at the 281 times pre-industrial CO_2 of the adopted first thaw; the ceiling found by Le Hir et al. (2009) is about ten times W_0). For $\tau = 0.3$, 1, 3 and 10 Myr the excess of CO_2 above its re-partitioned value then decays with e-folding times of 0.02, 0.06, 0.13 and 0.20 Myr and falls to a tenth within 0.10, 0.25, 0.44 and 0.59 Myr. The chronology is changed by the carbon consumed while that excess decays: five Myr after the first thaw the exchangeable inventory is smaller than under the instantaneous rule by 6, 19, 35 and 49% of the returned amount, and the first interglacial at $\nu = 0.725$ shortens from 33.0 to 31.7, 28.8, 21.2 and 7.9 Myr, while the glaciations keep their length of about 22.8 Myr because the sub-ice budget is unchanged.

With $\tau = 0.3$ and 1 Myr the model still gives four glaciations with none later at $\nu = 0.725$; with 3 and 10 Myr it gives five and six, and the interval of ν giving four, whose position is fixed by the glaciation count, moves from 0.719–0.732 to 0.721–0.732, 0.724–0.734, 0.729–0.739 and 0.734–0.742, its width staying at 0.008–0.011. Inside those intervals the shorter interglacials bring the later glaciations still closer in age to the first, as the crustal case already does relative to the adopted one (Table S5c). At the integrated members nearest the midpoints of those intervals, $\nu = 0.7275$, 0.72875, 0.735 and 0.740 for $\tau = 0.3$, 1, 3 and 10 Myr (Table S5e), the third glaciation ends 3.9, 8.5, 16.6 and 38.2 Myr inside the Gordon Lake bound and the fourth begins 12.5, 20.4, 31.7 and 56.5 Myr before the upper Timeball Hill tuffs allow, with 39.4, 36.1, 33.0 and 29.7 Myr of open water before it against the 48 required. The last deglaciation, whose date follows from the glaciation count, falls at 2.252 Ga for $\tau = 0.3$ Myr, inside the Hekpoort window (2.220–2.256 Ga), but at 2.260, 2.271 and 2.296 Ga for $\tau = 1$, 3 and 10 Myr, before that window by 3.9, 15.3 and 40.1 Myr; oxic air first appears at 2.359, 2.359, 2.362 and 2.348 Ga. At fixed ν the shortening of successive interglacials adds up, so that the last deglaciation moves earlier by 4.4 and 14.2 Myr at $\nu = 0.725$ for $\tau = 0.3$ and 1 Myr. Since ν follows from the glaciation count, however, we compare each treatment's member nearest the midpoint of its interval with the instantaneous rule's (Table S5e): no glacial date then differs by more than 0.6 Myr for $\tau = 0.3$ Myr, but by up to 8.0 Myr for $\tau = 1$ Myr and by up to 19.3 and 44.2 Myr for $\tau = 3$ and 10 Myr. The subset of the dated bounds that a given member meets is more sensitive to the treatment of the thaw than its dates are. At $\nu = 0.73125$, the crustal member that meets the upper Timeball Hill and open-interval bounds under the instantaneous rule (Table S5c), the third glaciation ends inside the Gordon Lake bound with $\tau = 0.3$ Myr, but the fourth then begins before the upper Timeball Hill tuffs allow and the open interval falls below the 48 Myr required, while the last deglaciation stays inside the Hekpoort window.

In the second variant the open-water partition itself is replaced by the one that calcite-saturated seawater of constant calcium content would have, $\beta(C) = 1 + (\beta_w - 1)/\sqrt{C}$, the form used for the carbonate-saturated sub-ice partition of Section S1.8 (Table S5b); at $C = 1$ this is β_w, close to the $1 + \mathrm{DIC}/2n_{\mathrm{C}} = 33$ of the modern ocean at saturation, and at a hundred times pre-industrial CO_2 it is 3.9. The sub-ice uptake of the crustal case is unchanged and the thaw re-partition is solved under the same law. The ocean then takes up only 2.3×10^{19} mol at the first thaw, CO_2 falls from 1083 to 626 times pre-industrial and halves in 0.46 Myr under the model's weathering, reaching 89 three Myr later, and because the approach to the glaciation threshold is paced by β near that threshold the interglacials last 6.3 Myr (median) instead of 33.0–38.9. At $\nu = 0.725$ the model then gives eight glaciations by 2.22 Ga and two later; four with none later occur only for $\nu = 0.759$–0.764, and there the four glaciations, each about 22.2 Myr long and separated by interglacials of 8.2–9.6 Myr, span about 115 Myr, the last ending at 2.333 Ga. No member with three or four glaciations has one beginning after 2.352 Ga or an interglacial longer than 12 Myr, whereas the Rietfontein diamictite

lies above the upper Timeball Hill tuffs and its glaciation began after 2.262 Ga. The recorded spacing is therefore not reproduced at any ν under that partition. Applied under the ice as well, as the adopted rule ($\beta_{\mathrm{ice}} = \beta_w$) would require, the same law gives a Marinoan glaciation of 1.6 Myr, outside the dated 4–15 Myr by which the sub-ice rule was chosen, and, at the adopted deglaciation level $X = 0.01$ bar, Paleoproterozoic glaciations of 2.8 Myr, 28 of them by 2.22 Ga at $\nu = 0.715$ (about 10 Myr at $X = 0.1$ bar, Table S5b).

The first conclusion we draw from these variants concerns the instantaneous re-partition, which represents as a single step a drawdown that takes 10^5–10^6 yr in published models: if the ocean side of the exchangeable reservoir takes up its share within a few 10^4 to a few 10^5 yr, as the re-saturation and carbonate-weathering times of Le Hir et al. (2008a) suggest ($\tau \lesssim 0.3$ Myr above), the chronology of Table S5c changes by 0.6 Myr at most, once ν is again fixed by the glaciation count; if the uptake instead takes the 1.0 Myr of the silicate route ($\tau = 1$ Myr), the dates move by up to 8.0 Myr and the last deglaciation falls 3.9 Myr outside the Hekpoort window. The second is that the length of the interglacials, and with it the agreement between four model glaciations and the recorded span of the glacial era, from the Makganyene to the Rietfontein diamictite, rests on the returned carbon remaining in an exchangeable ocean–carbonate reservoir whose response to CO_2 near the glaciation threshold is close to the modern, carbonate-compensated $\beta_w = 29.6$. If post-glacial weathering buried a third to a half of the returned carbon the interglacials would shorten by a third to three quarters, and with the response of calcite-saturated seawater alone they would last at most 12 Myr. The chronology therefore depends on a second carbon-cycle assumption besides the sub-ice store: that Paleoproterozoic seawater and shelf carbonate kept the returned carbon exchangeable, with a response to CO_2 close to the modern one. The model adopts this response through the partition β_w and does not derive it from the seawater chemistry of that time.

S1.10 Later schedules

Several inputs act only after the Paleoproterozoic and set the magnitude of the Neoproterozoic rise to modern oxygen, to which we do not apply the model (Section 4.4 of the main text); all of them are assumptions taken from the literature. Marine phosphorus burial appears low until the late Neoproterozoic (Reinhard et al., 2017), while phosphorus-to-iron ratios in iron formations suggest elevated Precambrian phosphate with a Cryogenian peak (Planavsky et al., 2010). We include both features without reconciling them, multiplying W_P by 3 between 0.75 and 0.635 Ga and weakening the iron trap from $k_0 = 10$ before 0.72 Ga to 1.67 after 0.55 Ga. The glacial chronology is insensitive to the strength of the iron trap, since with $k_0 = 60$ or 4 before the Neoproterozoic every glaciation onset and termination is unchanged to within 1.8×10^{-8} Gyr and first oxic air moves by at most 0.12 Myr; the bound that the phosphorus budget puts on k_0 is derived in Supplementary Text S6. We omit any dependence of the riverine phosphate delivery on continental emergence. The productivity factor $p(t)$ rises linearly from p_A at 0.75 Ga to one at 0.65 Ga, an interval chosen to match the rise of planktonic algae (Brocks et al., 2017). The constant productivity before that rise is an assumption on which the later oxygen level depends: with $p = 0.2$ after the transition, marine burial falls below the reductant sink, the middle Proterozoic is anoxic and oxygen is permanent only from 0.74 Ga, with the four glaciations unchanged (4, 0). Terrestrial burial and terrestrial methane are introduced with land plants over 0.47–0.40 Ga at their measured modern values (Section S1.1).

S1.11 Numerics and the present-day steady state

We integrate the system in age from 3.0 Ga to the present with a variable-order backward-differentiation (stiff) integrator at relative tolerance 10^{-8} and absolute tolerance 10^{-10}, steps of at most 2 Myr, the logarithm of oxygen as the state variable under ice, the untransformed, signed oxygen variable in open water (Section S1.3), and restarts at the 17 ages at which a forcing or its time derivative is discontinuous. Glacial entry and exit are located by the integrator's event detection as crossings of the glaciation condition of equation (8) of the main text and of the deglaciation condition (S7). The onset and permanence of atmospheric oxygen are determined on the integrator's own steps as crossings of 10^{-5} of the present oxygen level; the onset is the oldest upward crossing, and the permanence date is the upward crossing after which no downward crossing occurs. Glaciations are identified from the changes of the ice state and counted separately as those beginning at or before 2.22 Ga and those beginning after. The initial data (oxygen at 10^{-7} PAL, methane and phosphate away from their steady states, CO_2 from the open-water balance) excite transients; oxygen reaches the anoxic branch of Section S1.3 within about 8.5 yr, and the methane, phosphate and CO_2 transients decay before the nickel decline begins, after which the initial values no longer affect the solution.

We repeated all simulations reported in the main text, at $\nu = 0.715$, at both edges of the four-glaciation interval and for the alternative configurations, with a second, implicit Runge–Kutta integrator (Radau) at tolerance 10^{-8} on the untransformed state. The two integrators agree in every glaciation onset and termination and in the permanence date to within 0.001 Myr, and in the date of first oxic air to 0.25 Myr at

$\nu = 0.715$ (0.37 Myr at the interval's lower edge), which we take as the numerical uncertainty of that date. Where the first upward crossing follows a thaw by more than 1 Myr and oxygen drifts slowly through the threshold, the date of first oxic air is less well determined and differs between the two integrators by at most 0.5 Myr. The one exception is the calcite-saturation partition of Section S1.8, for which the two dates of first oxic air are 0.54 Myr apart and the other dates agree as above. For the simulations with a nonzero venting fraction θ of the sub-ice gases the first integrator fails with the logarithmic oxygen variable, and those cases are computed with the Radau integrator alone.

Table S6 compares the model's present-day state and its carbonate δ^{13}C with the budget of Holland (2002) and the compilation of Krissansen-Totton et al. (2015), and states how each quantity enters the model. Kerogen oxidation W_{ox} is set to close the oxygen budget at one PAL today, and the value so obtained reproduces Holland's independent estimate within its uncertainty. Net burial and the carbonate values after $t_{\times}$ enter as inputs under the isotope law (Section S1.7), and the pre-glacial carbonate values are reproduced by calibration, because the burial fraction was taken from the same δ^{13}C compilation. Under the isotope law the oxygen-independent reductant sink follows from the Phanerozoic burial fraction and the modern outgassing and was not set to a modern estimate. Its value today, 1.82 Tmol of O_2 equivalent per year, lies inside Holland's volcanic and hydrothermal estimate of 2.4 ± 1.8 (-0.32σ), an agreement that shows those two inputs to be consistent with Holland's budget and is not an independent test of the model. Across the transition the model's carbonate δ^{13}C changes by $+0.29$ per mil, whereas the measured change across the Lomagundi–Jatuli excursion is about $+7.9$ (Edmonsond and Dyer, 2026), and the model has no mechanism for the excursion.

Table S5: The sub-ice carbon store. (a) Carbon budget of the first Paleoproterozoic glaciation in the model (2.4509–2.4251 Ga, $\nu = 0.715$), the alkalinity the store would require if held in seawater of modern mass, and the capacities of the candidate carriers. (b) Glacial duration, interglacial length and number of glaciations under the adopted store and under the alternatives integrated: the carbon withheld from the air under the ice sets the duration, and the carbon returned at the thaw sets the interglacial length and with it the number of glaciations at a given ν. "All" in the fifth column means that the whole store returns to the ocean–atmosphere system at the thaw. The fixed-fraction rule has no variable for a store; the inventory in its row is the one implied by the warm partition applied to the airborne excess after the thaw (Section S1.8). Panels (c), the dated beds under the adopted store and under the crustal carrier, and (d)–(e), the carbon moved at the first deglaciation and the calendar of the crustal case under other treatments of the thaw (Section S1.9), follow on the next pages. Modern dissolved inorganic carbon of the ocean, 3.16×10^{18} mol.

(a) first glaciation, 25.7 Myr, outgassing 14.0 Tmol C yr^{-1} quantity	value	from
carbon outgassed under the ice	3.6×10^{20} mol C	equation (6) of the main text
removed by cold seafloor weathering	0.4×10^{20} mol (10–11%)	(S5) at the freezing point
left in the air (0.08 bar of CO_2 at the thaw)	0.1×10^{20} mol	equation (9), $1/\beta_{ice} = 3.4\%$
withheld from the air and returned at the thaw (the store)	3.1×10^{20} mol, or 99 times the modern ocean's dissolved inorganic carbon	equation (9), $\beta_{ice} = \beta_w = 29.6$
if held as seawater bicarbonate: added dissolved inorganic carbon; alkalinity required	+0.22 mol kg^{-1}; +0.22 eq kg^{-1}, 95 times the modern ocean's, 3.0×10^{20} eq in all (0.44 eq kg^{-1} if dissolving carbonate supplies it)	carbonate chemistry
uptake by an ocean of fixed alkalinity in equilibrium with the sub-ice air	5×10^{18} mol, 1.7% of the store	Henry's law at the freezing point
shelf carbonate that would have to dissolve under the ice and re-precipitate at the thaw	3.1×10^{20} mol $CaCO_3$, 1.1×10^7 km^3, 760 m over 15×10^6 km^2 of shelf	stoichiometry; shelf area of Le Hir et al. (2008a)
largest sub-glacial carbonate dissolution justified for a Neoproterozoic ocean	1.5×10^{21} g, 35 m over the same area	Le Hir et al. (2008a)
low-temperature alteration of ocean crust under an acidified sub-ice ocean (pH near 6)	consumes the whole outgassing; 18% airborne after 30 Myr; no return	Le Hir et al. (2008b,a)
removed over the following interglacial by the sinks of (S3) in excess of outgassing	3.2×10^{20} mol in 43.4 Myr (21.2 removed less 13.8 outgassed, net 7.4 Tmol C yr^{-1})	(S3)

(b) uptake and return sub-ice case	β_{ice}	X (bar)	ν	carbon returned at the thaw	glaciations by 2.22 Ga (and later)	duration (Myr)	interglacials (Myr)
adopted store	29.6	0.01	0.715	all	four (none)	23.6–25.7	43.4–48.8
smaller store	23	0.01	0.72	all	four (none)	18.5–20.0	42.6–47.4
uptake at the crustal-alteration efficiency, store returned	5.55	0.1	0.715	all	four (none)	22.6–23.4	42.4–47.2
calcite-saturation partition (carbonate-saturated seawater)	4.4–1.9	0.1	0.7325	all	four (none)	9.9	40.2–44.8
fixed airborne fraction 1.7% (the other sub-ice rule; no explicit store)		0.01	0.715	none stored; CO_2 continuous through the thaw, and the warm partition then implies 3.2×10^{20} mol exchangeable, as under the adopted store	three (none)	41–44	43–45
crustal carrier: only the airborne excess returned (swept in ν, Sec. S1.8)	5.55	0.1	0.719–0.732 0.715; 0.735	7.6×10^{19} mol (2.1×10^{20} mol kept in the crust)	four (none) for 0.719–0.732; five at 0.715, three at 0.735 (none)	22.5–23.4	33.0–38.9 at 0.725; 30–40 at the two others
fixed-alkalinity ocean, no other carrier	1.34–1.52	0.01	0.715	all	twelve (one)	1.2–1.3	11–30

Table S5: (continued) (c) The dated beds of Table 2 of the main text under the adopted store ($\nu = 0.715$) and under the crustal carrier at the middle ($\nu = 0.725$) and near the upper edge ($\nu = 0.73125$) of its four-glaciation interval: four glaciations of nearly the same length occur in all three columns, and the dated beds met differ between them. At the middle of the crustal interval the third glaciation ends inside the Gordon Lake bound and the last deglaciation inside the Hekpoort window, while the fourth glaciation begins before the upper Timeball Hill tuffs allow and the open interval before it is shorter than the Timeball Hill shale requires; near the upper edge the upper Timeball Hill, open-interval and Hekpoort bounds are met and the Gordon Lake and MAK-D ages are missed by 2.0 and 2.5 Myr (Table 3 of the main text adds the sulfur and permanence rows). Ages in Ga, intervals in Myr; "met by" and "missed by" give the margin to the bound; "met at 2σ": the first glaciation overlaps the dated range of the Ongeluk lavas but has ended by their central age, which the adopted first glaciation contains. Under either sub-ice case the last-deglaciation date follows from the glaciation count. The last row is the ice-free CO_2 from one Myr after a thaw to the minimum before the next glaciation.

(c) dated beds under the adopted store and under the crustal carrier bound (Table 2 of the main text)	adopted store, $\nu = 0.715$	crustal carrier, $\nu = 0.725$	crustal carrier, $\nu = 0.73125$
first glaciation: begins no earlier than 2.454, ice at the Ongeluk age and still at the MAK-D age 2.4241	2.4509–2.4251: Ongeluk met, MAK-D missed by 1.0	2.4500–2.4269: Ongeluk met at 2σ, MAK-D missed by 2.8	2.4496–2.4266: Ongeluk met at 2σ, MAK-D missed by 2.5
third glaciation over by 2.310 (Gordon Lake)	ends 2.289: missed by 20.7	ends 2.313: met by 3.3	ends 2.308: missed by 2.0
first to third deglaciation at most 114.1 (MAK-D to Gordon Lake)	135.8	113.6	118.6
fourth glaciation begins after 2.262 (upper Timeball Hill tuffs)	begins 2.2405: met by 21.5	begins 2.2745: missed by 12.5	begins 2.2566: met by 5.4
open interval before the fourth glaciation at least 48 (Timeball Hill shale)	48.8: met	38.9: missed	51.4: met
last deglaciation 2.256–2.220 (Hekpoort)	2.217: young by 3.1	2.252: met	2.234: met
first oxic air by 2.368 (Kaapvaal sulfur record, oxygen-only criterion)	2.353: late by 15	2.358: late by 10	2.360: late by 8
ice-free CO_2 ($\times$ pre-industrial), after a thaw $\rightarrow$ before the next glaciation	$253 \rightarrow 53$	$114 \rightarrow 56$	$116 \rightarrow 54$

Table S5: (continued) (d) Carbon at the first deglaciation under the two storage cases: carbon in the air and on the ocean side of the exchangeable reservoir before and after the thaw, the alkalinity that holding the carbon in seawater would require, and published post-glacial rates (Section S1.9). (e) The Paleoproterozoic calendar of the crustal case when the thaw re-partition is spread over an e-folding time τ of the effective partition (equation S8) and when the open-water partition is that of calcite-saturated seawater, $\beta - 1 \propto C^{-1/2}$. The ν intervals are those giving four glaciations by 2.22 Ga with none later, so that within each row the dates follow from the glaciation count as in panel (c); the member shown for each treatment is the integrated member nearest the midpoint of its interval (at the midpoint for $\tau = 1$ Myr). "Met by" and "early by" give absolute margins in Myr; the third column is the exchangeable carbon consumed within five Myr of the first thaw in excess of that under the instantaneous rule, as a share of the returned amount, evaluated at $\nu = 0.725$. Ages in Ga, intervals in Myr; CO_2 in multiples of pre-industrial.

(d) the first deglaciation under the two storage cases

quantity	adopted store, $\nu = 0.715$	crustal carrier, $\nu = 0.725$ (instantaneous re-partition)
CO_2 at the deglaciation → just after the thaw	281 → 281 (continuous)	1083 → 119
carbon moved out of the air at the thaw	none	4.8×10^{19} mol, 89% of the airborne CO_2, 15 times the modern ocean's dissolved inorganic carbon
ocean-side inventory above the entry state, before → after the thaw	3.1×10^{20} mol, the store, in place throughout	2.54×10^{19} mol (fixed-alkalinity share) → 7.36×10^{19} mol
kept in the crust	none	2.1×10^{20} mol
alkalinity to hold that carbon in seawater as bicarbonate	the store: 3.0×10^{20} eq, 95 times the modern ocean's (panel a)	the transfer: 4.8×10^{19} eq, 15 times the modern ocean's (+35 mmol kg^{-1} of dissolved inorganic carbon); 119 m of carbonate over 15×10^6 km^2 of shelf if dissolution supplies it (at most 35 m, Le Hir et al., 2008a)
removal over the following interglacial	net 7.4 Tmol C yr^{-1} over 43.4 Myr	net 2.3 Tmol C yr^{-1} over 33.0 Myr
published post-glacial drawdown	silicate weathering 7 times the present flux, CO_2 back near its initial level in about 3 Myr, ocean re-saturated 20 kyr after the thaw (Le Hir et al., 2008a); weathering discharge at most about 10 times the modern, recovery in a few Myr (Le Hir et al., 2009); about 200 kyr (Higgins and Schrag, 2003); at 7 times the present silicate flux of Le Hir et al. (2008a), 6.8 Tmol C yr^{-1}, the crustal transfer would be consumed in 1.0 Myr, and their peak carbonate weathering, one $CaCO_3$ per CO_2, would supply its alkalinity in 0.23 Myr	

(e) crustal carrier: the calendar under other treatments of the thaw

thaw treatment	CO_2 excess after the thaw: e-folding time; time to a tenth	carbon consumed within five Myr beyond the instantaneous rule	four glaciations, none later, for ν	member ν	ice-free intervals	third glaciation ends (Gordon Lake: by 2.310)	fourth begins (upper Timeball Hill: after 2.262)	open interval (≥ 48)	last deglaciation (Hekpoort 2.256–2.220); first oxic air
instantaneous re-partition at β_w (panel c)	none (at once)	–	0.719–0.732	0.725	33.0–38.9	2.313: met by 3.3	2.2745: early by 12.5	38.9	2.252; 2.358
$\tau = 0.3$ Myr	0.02; 0.10	6%	0.721–0.732	0.7275	32.6–39.4	2.314: met by 3.9	2.2745: early by 12.5	39.4	2.252; 2.359
$\tau = 1$ Myr	0.06; 0.25	19%	0.724–0.734	0.72875	30.1–36.1	2.319: met by 8.5	2.2824: early by 20.4	36.1	2.260; 2.359
$\tau = 3$ Myr	0.13; 0.44	35%	0.729–0.739	0.735	25.1–33.0	2.327: met by 16.6	2.2937: early by 31.7	33.0	2.271; 2.362
$\tau = 10$ Myr	0.20; 0.59	49%	0.734–0.742	0.740	10.4–29.7	2.348: met by 38.2	2.3185: early by 56.5	29.7	2.296; 2.348
calcite-saturation open-water partition, re-partition at once	CO_2 halves in 0.46	–	0.759–0.764	0.760	8.2–9.6	2.365: met by 55.0	2.3554: early by 93.4	9.6	2.333; 2.365

Table S6: The present-day steady state and the carbonate carbon isotopes of the model compared with published estimates, and the way each quantity enters the model. Every modern quantity but one is set to its modern value when the model is built or is an input; the exception is the oxygen-independent reductant sink, which follows from two published inputs under the isotope law and falls inside the estimate of Holland (2002) without having been set to it. Model $\delta^{13}C$ uses the era fractionations of Krissansen-Totton et al. (2015); the record columns are that compilation's era means and the excursion chronology of Edmonsond and Dyer (2026). Fluxes in $\mathrm{Tmol\,yr^{-1}}$ (the reductant sink in O_2 equivalents); σ is the model-minus-comparator difference in units of the comparator's uncertainty.

(a) modern budget, model against Holland (2002)			
quantity	model	comparator (σ)	how it enters
organic burial (marine, land)	10.0 (6.67, 3.33)	10.0 ± 3.3	identity
kerogen oxidation W_{ox}	8.19	7.5 ± 2.5 (+0.27)	identity of $O(0) = 1$; reproduces the independent estimate within its uncertainty
net organic burial	1.82	2.5 ± 1.0 (−0.68); 1.2 ± 0.8 (+0.77)	input under the isotope law
O_2-independent reductant sink	1.82	volcanic and hydrothermal 2.4 ± 1.8 (−0.32)	follows from f_{org} and V_{mod}; agreement not by construction
silicate weathering W_0 ($\mathrm{Tmol\,C\,yr^{-1}}$)	5.73	4.9–6.65 (Berner and Kothavala, 2001); 11.7–12 (Gaillardet et al., 1999)	identity of $C(0) = 1$; not used as a test
O_2 today (PAL); CO_2 today (× pre-industrial)	1.000; 1.001	unity by construction	identities of the requirements $O(0) = 1$, $C(0) = 1$
CH_4 today (ppmv)	0.70	natural source 218 $\mathrm{Tg\,yr^{-1}}$ (Saunois et al., 2020)	input, through the photochemical surface
CH_4 lifetime today (yr); methane-borne escape as a fraction of its diffusion limit	8.8; 0.997	Claire et al. (2006)	identities of the methane constants

(b) carbonate $\delta^{13}C$ (per mil), model against the record			
epoch	model	record	how it enters
isotope reference age $t_{ref} = 2.65$ Ga	−0.57	-0.59 ± 0.36	identity
pre-glacial interval (source on to first glaciation)	−1.0 to −0.3	within ±2 of baseline	calibration
change across the transition (eve of first ice to excursion peak age)	+0.29	+7.9 (peak 7.3, 6.1–8.1, at 2130 Ma)	not predicted (no excursion mechanism)
middle-Proterozoic node, 1.40 Ga	+0.03	$+0.04 \pm 0.21$	input
today	+1.72	$+1.75 \pm 0.19$	input

S2 Inputs and provenance

Every quantity that enters the model is a published measurement or law used without adjustment, an identity of the present-day steady state, a prescribed date or amplitude, an assumption, or the outgassing exponent ν, which the Paleoproterozoic glacial record fixes. An assumption, in the sense of the main text, is an input value chosen inside a published range. For the assumptions of Table S9 the model produces the four Paleoproterozoic glaciations at the chosen value and may fail to produce them at another value in the same range, whereas those of Table S10 do not affect the glaciations. Table S7 lists the drivers with their measured histories and the way each enters the equations, and Tables S8–S10 list every ingredient of the model with its value, its published range where one exists, and which of the five kinds of input named above it is. Fig. 2 of the main text plots the same quantities against their published ranges. Section S2.3 gives the nickel series in full, with the published interpretations of its decline and the other geochemical series that could date the decline of the volcanic reductant supply. In Section S2.4, published outgassing histories converted to the exponent ν are compared with the interval of ν that gives four glaciations, and the mechanisms that we integrated and did not adopt are listed in Section S2.5.

S2.1 Driver histories

Each forcing of the model has a measured history, either a time series or a dated event with its uncertainty, and a definite role in the equations of the main text (Table S7). Four of the drivers act before or during the transition, namely the marine oxygen source, the decline of the volcanic reductant supply (dated by the nickel series), continental emergence with the shift to subaerial volcanism, and the organic burial fraction, while volcanic outgassing supplies carbon throughout. The phosphorus, productivity and land-plant forcings act after the transition and set the size of the later rise of oxygen toward its modern level, to which we do not apply the model although we integrate it to the present (Section 4.4 of the main text). The Proterozoic oxygen level before that rise is compared with the paleosol proxies in the same section and in Supplementary Text S3. Of the modern fluxes in the row labeled "Modern budget", organic burial and natural methane enter the present-day steady state as inputs, whereas organic-carbon oxidation and the volcanic and hydrothermal reductant flux serve only as comparators for the model's present-day values (Supplementary Text S1). The last three rows of Table S7 list dated events and proxy records that do not force the model and are used only as checks.

Oxygenic photosynthesis is on early. Molybdenum isotopes record oxygen accumulating in shallow marine settings no less than 2.95 Gyr ago (Planavsky et al., 2014a), transition-metal enrichments dated by rhenium-osmium geochronology record a "whiff" of environmental oxygen at 2501 ± 8 Ma (Anbar et al., 2007), a reading contested for that core by Slotznick et al. (2022), who attribute the enrichments to post-depositional fluids along fractures, answered by Anbar et al. (2023) and re-answered by Slotznick et al. (2023), with the dispute open, and molecular clocks place crown Cyanobacteria in the Archean, with oxygenic photosynthesis evolving at least several hundred million years before the Great Oxidation (Fournier et al., 2021). Nothing in the model rests on the whiff: the source switches on at 2.95 Ga on the shallow-marine datum, and the contested enrichments enter only as a bracket.

S2.2 Every ingredient of the model

Table S8 lists the published values and the present-day identities, Table S9 the outgassing exponent ν with the prescribed quantities and the assumptions, and Table S10 the conventions that have no effect on the Paleoproterozoic chronology, together with the units and the numerics. Where we changed one input at $\nu = 0.715$ with all others held at their tabulated values, the outcome is given as the number of glaciations beginning before 2.22 Ga and the number beginning after. The intervals over which some value of ν restores three or four glaciations, and the outcome when the assumptions are varied jointly, appear in Section 4.5 of the main text and Supplementary Text S4. Besides ν in the first row of Table S9, three inputs are set from the Paleoproterozoic record, namely the crossing epoch $t_\times$ (inside the dated onset window of the Great Oxidation), the completion of continental emergence (at the first glaciation) and the sub-ice carbon rule (chosen between two by the criterion of Supplementary Text S1). Apart from these four, no input was adjusted to a Paleoproterozoic datum.

Every measured input enters at its published value, and where the literature gives a range we chose a value at a definite position inside it. We set the weathering response time τ_{sil} at the slow end of the 170–380 kyr range of Colbourn et al. (2015), the deglaciation CO_2 at the low end of the 0.01–0.1 bar proxy range (Hoffman et al., 2017), and the glaciation threshold at the lowest published value (Voigt et al., 2011). The modern outgassing is the midpoint of the 6–10 $\mathrm{Tmol\,C\,yr^{-1}}$ prior of Krissansen-Totton et al. (2018), three seafloor-weathering parameters take values inside the ranges of Krissansen-Totton and Catling (2017)

Table S7: Forcings of the model and their measured histories. Every forcing in the model has a measured history, a series or a dated event with its uncertainty; a mechanism inferred from a series is attributed to its authors and is not treated as a measurement. The last column lists the way each driver enters the model: as a published value used without adjustment, a present-day steady state, a prescribed date or amplitude, an assumption examined in Section 4.5 of the main text, or, for the outgassing exponent, as the quantity fixed by the Paleoproterozoic glacial record.

Driver	Measured history	Role in the equations	How it enters
Oxygenic photosynthesis	shallow-marine oxygen by 2.95 Ga (Planavsky et al., 2014a); end-Archean molybdenum and rhenium enrichments ("whiff") (Anbar et al., 2007), contested (Slotznick et al., 2022; Anbar et al., 2023; Slotznick et al., 2023)	marine oxygen source on at 2.95 Ga	dated event; switch-on age prescribed inside the proxy bracket; nothing rests on the whiff
Ni decline (mantle-cooling and hydrogen-supply proxy)	dissolved nickel reconstructed from the Ni/Fe of banded iron formations: about 400 nM before 2.7 Ga, below 200 nM by 2.5 Ga, about 9 nM by 0.55 Ga (Konhauser et al., 2009, 2015)	normalized shape $r_{\mathrm{Ni}}(t)$ of the reductant sink R and the methane source G up to the crossing epoch only	trend and timing of the published series used without adjustment (not the absolute concentrations); the proportionality of R and G to it is assumed
Continental emergence	stepwise decrease of shale triple-oxygen-isotope values at about 2.50 Ga, interpreted as rapid emergence (Bindeman et al., 2018)	weatherability f_w: $0.5 \to 1$ over 2.55–2.45 Ga	form of Krissansen-Totton et al. (2018); completion age prescribed at the onset of glaciation in the rock record, which sets the date of the model's first glaciation; four glaciations are kept for completion by 2.38 Ga or earlier
Subaerial volcanism	shift from submarine toward subaerial eruption at the Archean–Proterozoic boundary, 2.51–2.45 Ga (Kump and Barley, 2007)	subaerial reductant flux $\times 0.5$ from 2.5 Ga	assumed step; no effect on the glaciations ($\times 0.7$, no step: (4, 0), (4, 0))
Organic burial fraction f_{org}	carbonate-isotope mass balance: 0.137 ± 0.011 (2.8–2.5 Ga), 0.179 ± 0.007 (1.80–1.00 Ga), 0.228 ± 0.006 (0.54–0.00 Ga) at $\delta_{\mathrm{in}} = -5 \pm 1$ per mil (Krissansen-Totton et al., 2015)	Archean net burial N_A; the post-crossing sink $S = f_{\mathrm{org}} V_{\mathrm{out}}$	published value used without adjustment; carbonate $\delta^{13}\mathrm{C}$ after $t_\times$ enters as an input, so reproducing it is not a test
Outgassing	$V_{\mathrm{out}} = V_{\mathrm{mod}}(1 - t/4.5\,\mathrm{Gyr})^{-\nu}$, V_{mod} 6–10 $\mathrm{Tmol\,C\,yr^{-1}}$, $\nu \in [0, 1.46]$ (Krissansen-Totton et al., 2018)	carbon supply throughout	law and range published; V_{mod} at the prior's midpoint, an assumption; ν fixed by the glacial record
Modern budget	organic burial 10.0 ± 3.3, organic-carbon oxidation 7.5 ± 2.5, volcanic and hydrothermal reductant 2.4 ± 1.8 $\mathrm{Tmol\,O_2\text{-}eq\,yr^{-1}}$ (Holland, 2002); natural methane 218 $\mathrm{Tg\,yr^{-1}}$ (Saunois et al., 2020)	present-day steady state	burial and methane used as published; the oxidation and reductant fluxes are comparators for the model's present-day values (Supplementary Text S1)
Phosphorus delivery and burial	marine phosphorus burial low until the late Neoproterozoic (Reinhard et al., 2017); phosphorus-to-iron peak in the Cryogenian (Planavsky et al., 2010)	riverine pulse $\times 3$ over 0.75–0.635 Ga; iron trap k_0 $10 \to 1.67$ between 0.72 and 0.55 Ga	dated intervals; amplitudes assumed; the two records disagree in sign and both are used
Algal rise	Cryogenian rise of eukaryotic steranes (Brocks et al., 2017)	productivity $p(t)$: $p_A \to 1$ over 0.75–0.65 Ga	dated event; schedule assumed; sets the later oxygen level (compared with the proxies in Supplementary Text S3)
Land plants	earliest cryptospores, Ordovician (Rubinstein et al., 2010; Morris et al., 2018)	land burial 3.33 $\mathrm{Tmol\,C\,yr^{-1}}$ and land methane 13.6 $\mathrm{Tmol\,yr^{-1}}$ on over 0.47–0.40 Ga	dated event; modern values published
Cryogenian glaciations	Sturtian 717 → 659 Ma; Marinoan 644.5 (onset-bracket midpoint) → 635 Ma (Hoffman et al., 2017)	the two epochs at which the sub-ice carbon rule is applied (the Marinoan is its one check; the Sturtian is not reproduced)	dated events, not inputs
Seawater sulfate	micromolar in the Archean (Crowe et al., 2014); millimolar after the transition (Blättler et al., 2018)	none (no sulfur cycle)	two measured levels only, used to judge the set-aside sulfur-cycle alternatives
CO_2 proxies	two paleosol barometer schools about an order of magnitude apart across the transition (Sheldon, 2006; Kanzaki and Murakami, 2015); Mesoproterozoic halite fluid inclusions (Park et al., 2025)	none	tests, not inputs (Section 4.4 of the main text; Supplementary Text S8)

and Krissansen-Totton et al. (2018), and the weathering e-folding temperature is the Walker–Berner value tabulated by Graham and Pierrehumbert (2020). Because we take the heat-flow exponent n, which the outgassing and seafloor-weathering laws share, at the upper end of its range, the implied $m = \nu/n = 0.98$ lies 2 percent below the range of m that Krissansen-Totton et al. (2018) sampled; setting m inside that range leaves the glacial chronology unchanged (Table S10). The modern silicate-weathering flux implied by the present-day identity lies within the range of the carbonate-burial-based estimates and is about half the river-chemistry totals (Supplementary Text S1). The methane-borne hydrogen escape is at the diffusion limit because k_{esc} is itself the diffusion-limited value (Table S8). In anoxic air, water oxidizes the carbon of the escaping methane and frees an equal amount of hydrogen, which we assume also escapes, so that the total hydrogen escape is $E_{\mathrm{H}} = 2k_{\mathrm{esc}}N$ (Supplementary Text S1). The phosphorus-trap constant lies inside its published range at a value that does not affect the glacial chronology.

S2.3 Nickel and other proxies of the reductant decline

The molar nickel-to-iron ratio of banded iron formations falls from about 2.7 Ga, and the dissolved nickel concentration reconstructed from it runs from roughly 400 nM through much of the Archean to below 200 nM by 2.5 Ga and to near-modern values (roughly 9 nM) by about 0.55 Ga (Konhauser et al., 2009, 2015). Its compilers attribute the decline to cooling upper-mantle temperatures and a reduced eruption of nickel-rich ultramafic rocks; this attribution is one of several published interpretations (komatiites, the nickel-rich ultramafic rocks in question, are a volumetrically minor part of most Archean greenstone belts). In their enlarged compilation Konhauser et al. (2015) report that the decline between 2.7 and 2.5 Ga "remains clear" while its redox consequences are "admittedly complex". We use the series as the normalized shape $r_{\mathrm{Ni}} = 1$, 0.5 and 0.0225 at those three ages, log-linear between them, and make the reductant sink R and the hydrogen-fed methane source G proportional to it up to the crossing epoch. The model uses the trend and its timing, not the absolute concentrations, and the interpretation of the series that we adopt is given in Section 2.1 of the main text.

The cause of the nickel decline and the sign of its effect on the atmospheric redox budget each have more than one published interpretation (Konhauser et al., 2015; Wang et al., 2019; Kasting, 2013). Because nickel is an enzyme cofactor for methanogens, the decline was first interpreted as a methanogen famine that lowered the biogenic methane flux (Konhauser et al., 2009). As a mechanism for the rise of oxygen that hypothesis was set aside on redox-budget grounds by Kasting (2013), who concluded that "this mechanism cannot have contributed to the rise of atmospheric O_2". From nickel isotopes, Wang et al. (2019) argue that sulfide-derived nickel buffered the famine across the transition, writing that "Nickel derived from sulfides may have been the safety net that prevented even more severe Ni limitation of methanogens". Dissolved nickel estimated from greenalite, an archive independent of the iron-formation Ni/Fe ratio, is a few nanomoles per kilogram shortly before the model's first glaciation (Nke et al., 2025), consistent with nickel limitation of methanogens being established by then. These interpretations play no part in the model, whose equations contain nickel only through the proxy shape $r_{\mathrm{Ni}}(t)$ and not as a nutrient.

Which measured series is used to date the decline of the volcanic reductant supply is a modeling choice, and the mantle-cooling interpretation of the nickel series has published alternatives. By the mantle-cooling interpretation we mean specifically the one in which the hydrogen source declines with the volume of ultramafic seafloor (Kasting, 2013), and that volume itself has no measured history. In the gas-speciation calculation of Kadoya et al. (2020a) cooling by itself makes volcanic emissions more reducing rather than less ("as the mantle cools, volcanic emissions contain a greater proportion of reducing gases"), and in a mantle-redox model the timing of the Great Oxidation is "relatively insensitive to the mantle potential temperature" (Kadoya et al., 2020b). The mantle oxygen-fugacity evolution reconstructed by Kadoya et al. (2020b) is a published reductant forcing that is already tied to a measured history: in its standard case reducing volcanic gases keep atmospheric oxygen low until close to the Archean–Proterozoic boundary, and its linear redox trend is one of the sink laws integrated and set aside in Supplementary Text S1. Five published models of the transition specify the decline of their reductant flux in different ways. Claire et al. (2006) ground it in crustal oxidation by time-integrated hydrogen escape, Zahnle et al. (2006) use no time-dependent reductant law, Krissansen-Totton et al. (2018) sweep the outgassing history as an unknown, Minsky et al. (2026) hold the reductant input constant within each simulation, and Daines and Lenton (2016) prescribe it as an external forcing. None of the five grounds the decline in mantle cooling, and our log-linear interpolation through the dated nickel values is a prescribed forcing in the same sense as theirs.

D. T. Johnston asked whether other geochemical proxies of mantle cooling and of the volcanic hydrogen supply corroborate the nickel series, and we summarize a survey of them here. In iron formations and shales, zinc and copper are flat through the Precambrian while nickel falls in the same rocks (Robbins et al., 2013, 2026; Scott et al., 2013; Chi Fru et al., 2016), which argues against a generic partitioning artifact. A re-evaluation of nickel partitioning into iron oxides would place the drop somewhat later, nearer the

Table S8: Every ingredient of the model, I: quantities taken from the literature and used at their published values, with their sources, and the identities of the present-day steady state. A present-day steady-state quantity is one fixed by requiring $O = 1$, $C = 1$ and Holland's organic burial today; where an independent modern estimate exists it is printed beside the value as a comparator and is not used as a test. Fluxes in $\mathrm{Tmol\,yr^{-1}}$; O in PAL; C in multiples of pre-industrial CO_2.

Ingredient	Value or form	How it enters	Source
Escape constant k_{esc}; inventory N_{atm}	3.7×10^{-5} $\mathrm{yr^{-1}}$ (methane-borne escape $k_{\mathrm{esc}}N$ at the diffusion limit; total hydrogen escape E_{H} of (S2d)); 1.8×10^{20} mol per bar; one map from the methane variable to $p_{\mathrm{CH_4}}$	published value; the map an identity	Claire et al. (2006), eqs. 11–12
Methane oxidation $k_{\mathrm{eff}}(p_{\mathrm{O_2}}, p_{\mathrm{CH_4}})$	tabulated surface, bilinear in the logarithms, plus the modern point 3×10^{-9} $\mathrm{Tmol^{-1}\,yr^{-1}}$ at 0.21 bar; edge value outside the table	published (one-dimensional photochemistry)	Claire et al. (2006), Fig. 3
O_2 consumed by escaping CH_4; fate of the hydrogen freed by water; modern CH_4 lifetime; methane-borne escape as a fraction of its diffusion limit	none; assumed to escape ($f_{\mathrm{H_2}} = 2f_{\mathrm{CH_4}}$; alternative in Supplementary Text S1); 8.8 yr; 0.997	term of the oxygen budget; an assumption; identities of the escape and photochemistry constants	
Terrestrial CH_4 source S_{land}	218 (183–248) $\mathrm{Tg\,yr^{-1}}$ = 13.6 $\mathrm{Tmol\,yr^{-1}}$, on with land plants; sets $p_{\mathrm{CH_4}}(0) = 0.70$ ppmv	published value	Saunois et al. (2020)
Radiative forcing $F_{\mathrm{CO_2}}$, $F_{\mathrm{CH_4}}$	line-by-line tables, 1 bar N_2, references 278 and 0.715 ppmv; $F_{\mathrm{CH_4}} = 0$ below 0.715 ppmv (neglected forcing $\leq$0.84 $\mathrm{W\,m^{-2}}$); no N_2O; $Q_\odot = 238.17$ $\mathrm{W\,m^{-2}}$	published spectra; the methane floor assumed; the nitrogen inventory an assumption (Table S9)	Byrne and Goldblatt (2014)
Solar luminosity $s(t)$	$[1 + \frac{2}{5}\,t/4.57\ \mathrm{Gyr}]^{-1}$	standard	Gough (1981)
Snowball deglaciation experiments	albedo 0.6; insolation 0.94 of present; CO_2 forcing 40 $\mathrm{W\,m^{-2}}$ across their suite ($r = 0.686$); $Q_{\mathrm{ice}} = 136.1$ $\mathrm{W\,m^{-2}}$	published model suite (r: Table S9)	Abbot et al. (2012)
Deglaciation CO_2 proxies	0.01–0.1 bar	published range; X at its low end (Table S9)	Abbot et al. (2012); Hoffman et al. (2017)
Nickel decline $r_{\mathrm{Ni}}(t)$	1 ($\geq$2.7 Ga) $\rightarrow$ 0.5 (2.5) $\rightarrow$ 0.0225 (0.55 Ga), log-linear	published shape; proportionality assumed; used to $t_\times$ only	Konhauser et al. (2009, 2015)
Burial fractions f_{org}	0.137 ± 0.011 (2.8–2.5 Ga), 0.179 ± 0.007 (1.80–1.00), 0.228 ± 0.006 (0.54–0.00) at $\delta_{\mathrm{in}} = -5 \pm 1$ per mil	published value; band varied (Table S9); not a test after $t_\times$, where the later values enter as inputs	Krissansen-Totton et al. (2015), Table 3
Archean net organic burial N_A	$f_A\,V_{\mathrm{out}}(t_{\mathrm{ref}}) = 2.07$, $t_{\mathrm{ref}} = 2.65$ Ga	follows from the published f_A given ν; t_{ref} assumed	idem
Modern organic burial: marine, land	6.67, 3.33 (Holland's 10.0 ± 3.3 split $\frac{2}{3}/\frac{1}{3}$)	published value; the total is the present-day burial	Holland (2002); Burdige (2005)
Kerogen oxidation $W_{\mathrm{ox}}O^{1/2}$	$W_{\mathrm{ox}} = 8.19$ closes $\dot{O} = 0$ at $O = 1$; independent estimate 7.5 ± 2.5	law published; amplitude a present-day identity that reproduces the independent estimate within its uncertainty ($+0.27\ \sigma$)	Laakso and Schrag (2014); Holland (2002)
Modern O_2-independent sink $S(0)$	1.82 O_2-eq; volcanic + hydrothermal 2.4 ± 1.8	returned by the isotope law from f_{org} and V_{mod}; inside the independent estimate ($-0.32\ \sigma$) without having been set to it	Holland (2002)
Outgassing law	$V_{\mathrm{mod}}(1 - t/4.5\ \mathrm{Gyr})^{-\nu}$, $\nu = nm$, $n \in [0, 0.73]$, $m \in [1, 2]$; V_{mod}, ν: Table S9	published law and range	Krissansen-Totton et al. (2018)
Continental weathering	$W_0 f_w C^\beta e^{\Delta T/T_e}$, $\beta = 0.3$ (sampled 0.1–0.5), $\Delta T = \lambda F$, $\lambda = 0.69$ K/($\mathrm{W\,m^{-2}}$) = 3 K per doubling (assumed); T_e: Table S9	form and β published	Krissansen-Totton et al. (2018)
Modern silicate weathering W_0	5.73, closes $C(0) = 1$; literature 4.9–6.65 on a carbonate-burial basis (inside), 11.7–12 from river chemistry ($\times$0.49)	present-day identity; agreement not used as a test	Berner and Kothavala (2001); Gaillardet et al. (1999)
Seafloor weathering F_{sfw}	$F_d Q^b C^{\gamma/2} e^{(E_a/R_g)(1/T_{p,0} - 1/T_p)}$: $F_d = 0.459$, $E_a = 75$ $\mathrm{kJ\,mol^{-1}}$, $\gamma = 0.27$; $T_D = 1.02\,T_s - 16.67$ K, floor 271.15 K; pore offset 9 K	published posterior medians; b, n, f_{sed}: Table S10	Krissansen-Totton and Catling (2017); Krissansen-Totton et al. (2018)
Cryogenian check epochs	Marinoan 644.5 $\rightarrow$635 Ma; Sturtian 717 $\rightarrow$659 Ma	dated events; one check; Sturtian not reproduced	Hoffman et al. (2017), Table 1
Modern state	$O(0) = 1.000$, $C(0) = 1.001$, burial 10.0	identities	

Table S9: Every ingredient of the model, II: the exponent fixed by the Paleoproterozoic glaciation count (first row; the number of glaciations therefore belongs to the calibration and is not a test), the prescribed dates and amplitudes, and those assumptions (inputs chosen inside published ranges, some at the midpoint or an end of the range) that can affect whether the four glaciations occur. Outcomes of changing one input at $\nu = 0.715$ are given as (glaciations beginning before 2.22 Ga, after); the intervals over which some ν restores three or four glaciations are those of Section 4.5 of the main text and Supplementary Text S4.

Ingredient	Value	How it enters; outcome when changed	Source
Outgassing exponent ν	0.715; four glaciations on $(0.7075, 0.7225) = 1.0\%$ of $[0, 1.46]$; three or four to 0.7388 (= 2.1%) if the three glaciations of the older correlation are admitted	fixed by the glacial record (four beginning at or before 2.22 Ga, none after); edge values 0.71 and 0.72 used in every comparison	Section 2.4 of the main text; Fig. 6
Modern outgassing V_{mod}	8 Tmol C yr^{-1} (prior 6–10)	midpoint of the published prior, an assumption; at 6 / 10 four glaciations occur at $\nu = 0.735$ / 0.7025	Krissansen-Totton et al. (2018)
Crossing epoch $t_\times$	2.4425 Ga in the onset window 2.46–2.43	prescribed; the model computes no crossing epoch of its own; seven values across the window keep the four glaciations and shift the chronology by $\leq$9 Myr from its dates at the tabulated $t_\times$	Gumsley et al. (2017); Warke et al. (2020)
Methane scale G_A	1.64 Tmol CH_4 yr^{-1} at $r_{\mathrm{Ni}} = 1$ ($g_G = 0.0983$; 0.0946–0.1010 across the window)	follows analytically from $t_\times$: $B_{\mathrm{mar}} = R + 2G$ at $t_\times$	eq. (3) of the main text
Reductant R_A; step at 2.5 Ga	2.5 Tmol O_2-eq yr^{-1} at $r_{\mathrm{Ni}} = 1$; $\times$0.5 from 2.5 Ga	prescribed amplitude, held fixed; no effect on the chronology under the isotope sink law; step $\times$0.7 or none: (4, 0), (4, 0)	Kump and Barley (2007)
Post-crossing sink law	$S = f_{\mathrm{org}} V_{\mathrm{out}}$; nodes $(t_\times, 0.148)$, $(1.40, 0.179)$, $(0.27, 0.228)$	chosen among four integrated laws by the carbonate-isotope criterion of Supplementary Text S1; values published; carriers not identified	eq. (4) of the main text
Reference epoch t_{ref}; f_A band	2.65 Ga (bin 2.8–2.5); $f_A \pm 1$ s.e.	assumed: t_{ref} 2.8 / 2.5 (4, 1) / (3, 0); f_A −/+1 s.e. (3, 0) / (4, 1)	Krissansen-Totton et al. (2015)
Emergence weatherability f_w	0.5 → 1 over 2.55–2.45 Ga	form published; completion prescribed at the onset of glaciation in the rock record, which sets the date of the model's first glaciation; four glaciations kept for completion by 2.38 Ga or earlier; Kump and Barley dates (4, 0), Bindeman et al. span (0, 0)	Krissansen-Totton et al. (2018)
Glaciation threshold D^*	10.1 W m^{-2}, constant (other transitions 17.9, 21.4, 30.2; 15.8 for the early Paleoproterozoic)	assumption, lowest published value: 15.8 (0, 0); drifting (1, 0); some ν gives three or four up to 14.7	Voigt et al. (2011); Yang et al. (2012); Feulner et al. (2023)
Nitrogen inventory	1 bar	assumption: 0.5 bar (5, 10); some ν gives three or four down to 0.57 bar	Byrne and Goldblatt (2014)
Deglaciation level X	0.01 bar (36 × pre-industrial)	low end of the proxy range; assumption: midpoint (3, 0), top (2, 0) (at $\beta_{\mathrm{ice}} = \beta_w$)	Abbot et al. (2012)
Exit-rule amplitude r	0.686	the snowball models' amplitude; assumption: full-table amplitude (5, 0), log-linear slope (3, 0)	Abbot et al. (2012)
Weathering e-folding temperature T_e	11.1 K (conventional 5–15; nominal 10–40)	assumption on which the glaciations depend: 13.9 K (6, 12); 17.7 K (7, 26); some ν gives three or four for 6.6–19.6 K	Graham and Pierrehumbert (2020); Krissansen-Totton et al. (2018)
Weathering response time τ_{sil}; partition β_w	380 kyr (published 170–380) $\Rightarrow \beta_w = 29.6$	slow end of the published range; assumption: 240 kyr (6, 1), 15–16-Myr glaciations	Colbourn et al. (2015)
Sub-ice carbon rule	eq. (9) of the main text, $\beta_{\mathrm{ice}} = \beta_w$, airborne share 3.4%, store returned at the thaw	chosen between two integrated rules by the criterion of Supplementary Text S1 (the other rule, a Marinoan-derived airborne fraction 1.7% with glaciations lasting 41–44 Myr, does not give four glaciations with none later at any value of ν under the isotope sink law); store kept in altered ocean crust instead and only the airborne excess returned (the crustal case of Table 3 of the main text, which gives the glaciation dates): four glaciations and none later for $\nu = 0.719$–0.732; a parameterization and, with D^* and the nitrogen inventory, the model's largest physical assumption; no identified carrier for the returned store (budget in Supplementary Text S1); Marinoan check 5.1 Myr in [4, 15]; Sturtian 5.3 not reproduced	Hoffman et al. (2017); Le Hir et al. (2008a)
Sub-ice venting θ	0 (O_2 and CH_4 consumed below the ice)	limiting case; assumption: $\theta = 0.01$, 0.03, methanotrophy first: (4, 0), (4, 0), (4, 0)	

Table S10: Every ingredient of the model, III: assumed conventions with no effect on the Paleoproterozoic chronology (outcomes as in Table S9), the units, the Lomagundi productivity surge (which the model omits), and the numerics.

Ingredient	Value	How it enters; outcome when changed	Source
Seafloor values chosen in published ranges	$b = 1$, $f_{\mathrm{sed}} = 0.6$ (midpoints); $n = 0.73$ (upper end; implied $m = \nu/n = 0.98$)	assumed; $n = \nu$ ($m = 1$): (4, 0)	Krissansen-Totton et al. (2018)
Productivity schedule $p(t)$	$p_A = 0.332$ (derived) flat to 0.75 Ga, linear to 1 by 0.65 Ga	assumed; an oxic middle Proterozoic needs $p \gtrsim 0.30$ after the transition (at 0.2: (4, 0) but an anoxic middle Proterozoic); sets the Proterozoic O_2 level, which lies below the paleosol floor (Supplementary Text S3)	
Phosphate and iron trap	nutrient factor 0.93 → 0.99; pulse ×3 on 0.75–0.635 Ga; $k_0 = 10$ (>0.72 Ga) → 1.67 (<0.55); trap off above $O_d = 0.3$ PAL	assumed inside published ranges; $k_0 = 60$, 4: (4, 0), (4, 0); bounded above by the phosphorus budget (Supplementary Text S6)	Planavsky et al. (2010); Reinhard et al. (2017)
Sub-ice throttles; O_2 floor scale	weathering and burial ×0.25 under ice; 10^{-8} PAL	assumed; no effect	
Fire suppression of land burial	$O_f = 0.75$ PAL, exponent 5; land burial ramps on over 0.47–0.40 Ga; zero before land plants	published form; no part in the Paleoproterozoic	Belcher and McElwain (2008)
Kerogen law at high O_2	$O^{1/2}$ unbounded	assumed; a ceiling at 0.1 PAL: (4, 0), chronology unchanged, but interglacial and Proterozoic O_2 about tenfold lower through the W_{ox} identity and first oxic air at 2.126 Ga; bears on the oxygen dates	
Photosynthetic source	on from 2.95 Ga	switch-on prescribed inside the proxy bracket	Planavsky et al. (2014a)
Lomagundi productivity surge	not in the model	excursion not predicted; an imposed surge ×1.5 on 2.22–2.06 Ga leaves the chronology unchanged ((4, 0)); roles of an imposed excursion in Supplementary Text S5	
Units	flux unit 1.67×10^{13} mol yr^{-1}; O unit 1×10^{-3} PAL; 1 PAL $O_2 = 3.7 \times 10^{19}$ mol (in the methane sink $0.21 N_{\mathrm{atm}}$ per PAL, two percent more); $C = 1 = 5 \times 10^{16}$ mol of atmospheric carbon	conventions	
Initial data; integration	$O = 10^{-7}$ PAL, methane and phosphate transients, C from the open-water balance at 3.0 Ga; backward differentiation $10^{-8}/10^{-10}$, steps ≤2 Myr, ln O under ice, 17 restart ages; a second implicit Runge–Kutta integrator at every reported value; onset and permanence dates taken where O crosses 10^{-5} PAL	initial transient decays before the nickel decline begins; numerics (Supplementary Text S1)	

first glaciation (Eickhoff et al., 2014). The cobalt records of iron formations and of pyrite disagree with each other, and chromium, uranium and molybdenum track weathering and redox conditions rather than mantle cooling. Among crustal proxies, basalt chemistry, upper-crustal MgO and sedimentary Cr/U show the compositional change beginning earlier and proceeding more smoothly than the break in the nickel series (Keller and Schoene, 2012; Tang et al., 2016; Smit and Mezger, 2017). Petrological estimates of mantle potential temperature (Herzberg et al., 2010) and the argument for near-constant surface heat flow (Korenaga, 2008) disagree on absolute Archean temperatures but agree that surface heat flux is only weakly sensitive to mantle temperature. Paleomagnetic constraints on the thermal history of the core (Brenner et al., 2022) are a further line of evidence on the cooling history, one that D. T. Johnston favors. The model uses none of these series; to corroborate the nickel chronology, another proxy of the same cooling would have to reproduce the factor by which $R + 2G$ falls from its constant Archean value to its value at the crossing epoch, that is, from 5.79 to 2.07 Tmol O_2-eq yr^{-1}.

Four exploratory simulations made with the solver of the main text after the model was specified (Table S11) show that, for a given crossing epoch, the glacial chronology does not depend on how R and G decline before that epoch. In these simulations R, G or both are made to follow the relative heat flow of the outgassing law instead of the nickel shape, or G is held constant up to the crossing epoch, with G_A re-derived from the crossing identity at the prescribed $t_\times$ and everything after $t_\times$ unchanged. Each keeps the four glaciations beginning before 2.22 Ga and none after, no glacial date moves by more than 1.8 Myr, the date of first oxic air is unchanged within its uncertainty, and only the Archean methane level differs among them. This insensitivity follows from re-deriving G_A in each simulation so that the crossing still falls at the prescribed $t_\times$, and it is therefore not independent support for the nickel chronology. If instead the amplitudes R_A and G_A are held fixed and the crossing epoch is computed from them, the source overtakes the sinks inside the dated onset window of the Great Oxidation only when both fluxes follow the nickel shape. When R or G is given the heat-flow shape, the crossing falls hundreds of millions of years later or does not occur

Table S11: Decoupling of the two fluxes that follow the nickel series (exploratory simulations at $\nu = 0.715$ with the solver of the main text; in each of them G_A is re-derived so that $B_{\mathrm{mar}} = R + 2G$ at the prescribed $t_\times$, and after $t_\times$ both fluxes follow the carbonate-isotope sink law of equation (4) of the main text). "Heat flow" is the relative heat flow of the outgassing law normalized at 2.7 Ga. The four variants have the same glacial chronology as the main-text simulation (first row) and differ from it only in the Archean methane level.

$R(t)$ before $t_\times$	$G(t)$ before $t_\times$	glaciations beginning before, after 2.22 Ga	first oxic air	Archean CH_4 (ppmv)
nickel shape (main text)	nickel shape	four, none	2.353 Ga	279 [a]
heat flow	nickel shape	four, none	unchanged	194
nickel shape	constant to $t_\times$	four, none	unchanged	145
heat flow	heat flow	four, none	unchanged	121
nickel shape	heat flow	four, none	unchanged	162

[a] Under the escape assumption of Section 2.2 of the main text, as in every row; 558 ppmv in the methane-only case of Section S1.3.

at all.

We take the methane source G to be hydrogenotrophic, that is, produced by methanogens from volcanic hydrogen, both in the crossing identity and in the simulations of Table S11, so that G enters equation (3) of the main text with a factor of two, $B_{\mathrm{mar}} = R + 2G$. With R_A prescribed and G_A set by the crossing epoch, methane then accounts for 72% of the oxygen-independent sink at $t_\times$. If G were instead methane fermented from photosynthate it would be oxygen-neutral, and the crossing would come from R alone, near 2.64 Ga, a date that follows directly from the prescribed input histories. Hydrogen escape adds no oxygen to the instantaneous atmospheric balance, but in the long-term planetary budget (Catling et al., 2001) the escape integrated between 3.0 and 2.2 Ga leaves behind 1.65×10^{21} mol O_2-equivalent of oxidizing power, 0.69–1.19 times the surface inventory of excess oxidants estimated by Hayes and Waldbauer (2006). The model has no crustal or mantle reservoir to hold this oxidizing power and cannot be used to test whether the decline of methanogenesis delayed the oxidation by slowing hydrogen escape, as Kasting (2013) argued (Section 5.2 of the main text).

S2.4 Published outgassing histories converted to the exponent

Krissansen-Totton et al. (2018) sample $\nu = nm$ over $[0, 1.46]$ and do not determine it inside that range. Their prior, a product of two uniform variables, has median 0.53 and central range 0.03–1.24; 68% of the prior mass lies below $\nu = 0.715$ and the four-glaciation interval holds 1.4% of its mass (3.0% for three or four glaciations). To ask whether published outgassing histories determine the exponent independently, we examined 29 sources and converted the 17 that state a history or adopt a value to this exponent at one age (Table S12). A history whose outgassing at age $t_L = 2.45$ Ga is $\mathcal{R}$ times the present value is assigned the level-equivalent exponent $\nu_L = \ln \mathcal{R} / [-\ln(1 - t_L/4.5\ \mathrm{Gyr})] = \ln \mathcal{R} / 0.786$. These are our conversions of the published curves, not determinations by their authors. On the same scale the four-glaciation interval corresponds to $\mathcal{R}$ between 1.744 and 1.765, $\nu = 0.715$ to $\mathcal{R} = 1.75$ and a decline of 3.5 percent per hundred million years at that age, and the upper edge of the published range to $\mathcal{R} = 3.15$.

The converted exponents ν_L scatter over a range much wider than the four-glaciation interval, and none of them lies inside it. A group of conversions lies at ν_L of 0.70–0.79, a range that contains $\nu = 0.715$ although no single conversion falls inside the four-glaciation interval. Its members are the standard heat-flow exponent of Sleep and Zahnle (2001) with outgassing proportional to heat flow, the same value adopted by Claire et al. (2006), the heat-flow history of Canfield (2004) taken linearly, and the preferred slowing factor of Holland (2009), who chose it to place the hydrogen crossover of his model near the Great Oxidation. These conversions share one assumption, that total outgassing is proportional to a conventionally declining surface heat flow, and none of them is a measurement; the outgassing law of Krissansen-Totton et al. (2018) used here is built on the same assumption. No source in the group gives an uncertainty, and where the same authors vary the assumption the spread in ν_L is of order one half to one (0.48–1.12 for Holland's alternatives, 0.79–1.58 for Canfield's).

Outgassing histories built on plate-tectonic scalings of the heat flow (spreading proportional to heat flow squared, deeper melting under a hotter mantle) convert to larger exponents, ν_L of about 1.03–2.16. Archean atmospheric xenon is the only measured proxy among the sources, and it implies mantle degassing equivalent to $\nu_L \simeq 2.90$–3.07 or a burst near 2.93, subject to the caveat of Krissansen-Totton et al. (2018, 2021) that metamorphic and recycled-arc CO_2 need not scale with mantle degassing. For comparison, at $\nu = 0.715$ the mean outgassing over the interval covered by those xenon budgets is only 1.50 times the present value. The models with near-constant surface heat flow and slow early plates convert to $\nu_L \simeq 0.00$, the lower edge of the

published range.

For the Paleoproterozoic glacial era itself, published geological reconstructions show no smooth outgassing trend of either sign. Proposals include a magmatic lull beginning near the first glaciation and lasting through much of the glacial era (Condie et al., 2009), a degassing burst, a step increase in volcanic CO_2 at the Archean–Proterozoic boundary, and a secular rise of total CO_2 input after the transition (Table S12). Plate-model flux reconstructions do not extend back to the Paleoproterozoic, and two recent reviews name the outgassing history as the dominant and poorly constrained uncertainty (Catling and Zahnle, 2020; Isson et al., 2020). Within this ensemble of published histories, whose spread in ν is of order unity, the value of ν fixed by the glaciation count corresponds to one convention from the literature, namely total outgassing proportional to the standard declining mantle heat flow.

S2.5 Alternatives integrated and set aside

Besides the alternatives already described (the four sink laws, the two sub-ice carbon rules and the crustal storage case of Supplementary Text S1; the seven crossing epochs and two emergence chronologies of Table S9), we integrated and set aside several further mechanisms proposed in the literature or by D. T. Johnston during the development of the model (Table S13). We integrated them on an earlier configuration of the model, which included a sulfate reservoir that the present model lacks, and therefore report their outcomes qualitatively, without numbers. These negative results are the reason the present model has no sulfur or iron cycle, uses nickel as a dated proxy and not as a mechanism, and keeps the abiotic continental weathering law of Krissansen-Totton et al. (2018); the two measured levels of seawater sulfate were used only to judge the alternatives that include a sulfur cycle.

Table S12: Published outgassing and heat-flow histories converted to the exponent ν of the outgassing law of the main text at $t_L = 2.45$ Ga ($\nu_L = \ln \mathcal{R}/0.786$, with $\mathcal{R}$ the outgassing at t_L relative to today). The conversions are ours, not the authors' determinations. The four-glaciation interval is $(0.7075, 0.7225)$ and the published range $[0, 1.46]$; no converted value lies inside the interval.

Source	Quantity and basis	ν_L	Remark
Sleep and Zahnle (2001); Zahnle and Sleep (2002)	relative heat flow $Q = (1 - t/4.5\,\mathrm{Gyr})^{-\mu}$ with metamorphic $CO_2 \propto Q$; their standard and low exponents	0.70 (standard)	assumed law; the origin, through Krissansen-Totton et al. (2018), of the form used here
same	mid-ocean-ridge $CO_2 \propto$ seafloor creation ($\propto Q^2$) $\times$ degassing depth	1.16–2.16	ridge term only
Claire et al. (2006)	volcanic and metamorphic CO_2 both $\propto Q$ with the standard exponent of Sleep and Zahnle (2001)	0.70	adopted value, same form
Krissansen-Totton et al. (2018)	$\nu = nm$, $n \in [0, 0.73]$ spanning declining to near-constant heat flow, $m \in [1, 2]$ spanning outgassing $\propto Q$ to crustal production $\propto Q^2$	$[0, 1.46]$ (prior; median 0.53)	sampled range, not a determination; source of the law
Krissansen-Totton et al. (2021)	the same law with wider priors on both exponents; inverse fit to carbonate $\delta^{13}C$ with a xenon-based Archean mantle outgassing datum; posterior shown graphically	wider than the range of Krissansen-Totton et al. (2018) (prior)	the same group's later paper widened the range
Canfield (2004)	volcanic and hydrothermal fluxes $\propto$ a radiogenic heat-flow history, taken linearly or squared (plate velocity)	0.79; 1.58	sulfur-cycle model; assumed scaling
Hayes and Waldbauer (2006)	mantle carbon input scaled to spreading-center heat flow	1.03	juvenile mantle carbon only; recycled CO_2 separate
Lowell and Keller (2003), as used by Mills et al. (2014)	plate-creation rate from plate-tectonic heat-loss models, Archean roughly tenfold present	above the interval; no value at t_L obtained	cited through Mills et al. (2014)
Holland (2009)	"slowing of the Earth system" factor e^{-kt} on degassing and recycling; the preferred k puts his hydrogen crossover near the Great Oxidation	0.77 (preferred); 0.48–1.12	tectonic factor chosen by the author
Kadoya and Tajika (2014); Kadoya and Tajika (2015)	degassing $\propto$ spreading rate $\times$ melt-generation depth from parameterized convection; converted as if degassing tracked radiogenic heat production	1.06	converted from their scaling law alone
Avice et al. (2017)	radiogenic ^{129}Xe: mantle degassing integrated over the last three billion years several times present, expressed as a power law with that mean	2.90–3.07	mantle volatile flux, not total CO_2; at $\nu = 0.715$ that mean is 1.50 times present
Marty et al. (2019)	^{129}Xe deficit: degassing at the end of the Archean at least an order of magnitude above present, as a burst	2.93 as a level	mantle flux; a transient rise inside the modeled glacial era
Korenaga (2008, 2018)	near-constant surface heat flux; slower early plates	0.00 (the $n = 0$ edge)	heat flow, not outgassing
Franck et al. (2000)	volcanic source $\propto$ spreading rate from boundary-layer theory	no value at t_L obtained	structure: $m = 2$ on mantle heat flow
Dasgupta (2013)	hotter mantle above the carbonated solidus: more efficient outgassing per unit flux	positive, unquantified	
Condie et al. (2009); Spencer et al. (2018)	zircon and greenstone record: a magmatic lull beginning near the first glaciation, ended by a flare-up	episodic, not a power law	magmatic proxy, qualitative for CO_2
Eguchi et al. (2020)	scenario: a tectonic transition at the Archean–Proterozoic boundary raising volcanic CO_2	opposite sign	assumed forcing
Lee et al. (2016)	growth of the continental carbon reservoir raising the total CO_2 input after the transition	negative for the later trend	total input, driven by reservoir growth
Fuentes et al. (2019)	ridge CO_2 from convection with carbonated melting; sluggish to active lid	non-monotonic; no value obtained	ridge only
Tajika (2007)	isotope mass balance: Proterozoic global glaciations from decreasing degassing together with organic burial	positive, unquantified	
Rushby et al. (2018)	adopt the standard heat-flow exponent with spreading $\propto Q^2$	as the first two rows	derivative of the first row
Mills et al. (2011, 2017); Williams et al. (2019); Dutkiewicz et al. (2024); Mills et al. (2014); Wong et al. (2019)	CO_2-flux reconstructions from full-plate models and Neoproterozoic degassing forcings	none reaches the Paleoproterozoic	the only reconstructions tied to plate configurations; they begin more than a billion years after the Paleoproterozoic glaciations
Catling and Zahnle (2020); Isson et al. (2020)	reviews: the outgassing history is omitted or named as the dominant uncertainty		

Table S13: Alternative mechanisms integrated and set aside (Section S2.5), one line each with its outcome. None is part of the present model, and no number from these simulations is used here.

Alternative	Source of the proposal	Outcome
Rising seawater sulfate as the driver of the methane decline (competitive exclusion of methanogens by sulfate reducers) in place of the declining hydrogen supply	literature (Zahnle et al., 2006; sulfate chronology of Crowe et al., 2014, Luo et al., 2016 and Blättler et al., 2018)	the sulfate rise in the rock record follows the loss of the sulfur-isotope signal rather than preceding it, so a sulfate-driven methane decline comes too late to begin the transition; set aside on the chronology of the rock record
Anaerobic oxidation of methane coupled to a sulfate reservoir, the methane source reduced by the fraction intercepted	D. T. Johnston	with Archean sulfate at its measured scarcity the intercepted fraction is small before the transition; the coupling did not change any date and worsened that configuration's account of the later sulfate rise
Pyrite-burial decline as the mechanism of the post-transition sulfate rise	Luo et al. (2016), implemented at its published form	reproduces those authors' short lag between the loss of the isotope signal and the sulfate rise when started from that loss, and not when started from the model's first oxygenation; informative about a sulfur cycle the present model does not include
A finite, depletable crustal sulfide inventory behind the oxidative-weathering sink	D. T. Johnston	the weathering sink depends on instantaneous oxygen only; a sulfide inventory sized from the literature did not change the timing of the sulfate rise in that configuration
One weathered-rock driver for phosphorus delivery, sulfide oxidation and iron, tied by crustal P:S:Fe ratios	D. T. Johnston	the crustal and shale ratios exist but disagree with each other and with the measured modern fluxes, so weathering is not congruent, and the coupled iron share overproduces the ferric-iron inventory; not adopted
Sulfate-dependent hydrothermal reducing power modulating $R(t)$	D. T. Johnston, after Kump and Seyfried Jr. (2005) and Kump and Barley (2007)	consistent with the rock record where it was integrated but not required by any datum; it shifted the onset date systematically without improving any comparison
Sulfate-controlled hydrothermal iron delivery compared with the banded-iron-formation chronology	D. T. Johnston	every variant failed the iron-formation chronology on that configuration's sulfate history; the present model has no iron cycle
A threshold-crossing komatiite model of the reductant decline (plume excess temperature falling through the komatiite threshold as the mantle cools)	our follow-up to D. T. Johnston's question on the nickel mechanism, with published plume-temperature estimates	reproduces the break in slope of the nickel decline and an oscillatory glacial era but makes oxygen permanent too early in every variant; excluded in that minimal form, and nickel remains a dated proxy

S3 Geological data and the comparisons with the rock record

The comparisons of Section 4 of the main text rest on three bodies of data, which we set out here with their sources and the criteria we apply to them. The first is the set of dated beds that bound the Paleoproterozoic glaciations, with the correlations under which they give four glaciations or three (Section S3.1). The second is the Transvaal compilation of mass-independent sulfur isotope fractionation ($\Delta^{33}S$) of Uveges et al. (2023), with the statistic by which we count its changes of state and the per-core counts behind it (Sections S3.2–S3.4). The third is the later oxygen record, for which the choice between two mid-Proterozoic upper limits determines whether one oxygenation step or two are needed to describe it (Section S3.5). We then state what was fixed before the integrations reported here, give every comparison in full, including those that the model fails, together with the check that the archived code reproduces earlier outputs of the same equations (Section S3.6), and list the integrations made afterwards (Section S3.7).

S3.1 Dated beds and the correlation of the cratons

We compare the model's dates with individual dated beds, each of which bounds a model date from one side only, and where a date is bounded from both sides we call the interval between the two bounds a window. A maximum depositional age below a diamictite shows that the glaciation began later, a dated lava within it that ice was present at some age inside the lava's uncertainty, and a tuff or shale above it that the glaciation had ended. Table S14 lists every bed we use with its 2σ uncertainty, the bound it supplies at the lenient edge of that uncertainty, and its source, and Fig. 3 of the main text plots each of them against the model's glaciations. In Section 4.2 of the main text we rely mainly on three bounds derived from pairs of these beds. On the Kaapvaal craton the Heynskop maximum depositional age below the Makganyene diamictite (Senger et al., 2023) and the Ongeluk lavas interfingering with its top (Gumsley et al., 2017) constrain the first glaciation to begin at or after 2.454 Ga, to have ice present at some age between 2.4281 and 2.4229 Ga, and to last at most 31.1 Myr plus the unmeasured duration of the lavas. The third glaciation ended before deposition of the Gordon Lake tuffs above the Gowganda diamictite (Rasmussen et al., 2024, 2013) and of the basal Timeball Hill shale and tuff (Hannah et al., 2004; Rasmussen et al., 2013), and was therefore over by 2.310 Ga. From Kaapvaal ice still being deposited at 2.4241 Ga (Senger et al., 2023) to that date the beds leave at most 114.1 Myr for the first interglacial, the second glaciation, the second interglacial and the third glaciation together. The upper Timeball Hill tuffs below the Rietfontein diamictite (Rasmussen et al., 2013) put the start of the fourth glaciation at or after 2.262 Ga and make the open-water interval after the third at least 48 Myr long.

Two of the dated bounds, those on the Hekpoort lavas and on the Mooidraai Formation, are weaker than the others, because neither rests on a U–Pb age of an igneous unit. The window for the last deglaciation, 2.220 to 2.256 Ga, therefore has at its lower edge an age model for the Hekpoort lavas above the Rietfontein diamictite (Schröder et al., 2016; Poulton et al., 2021), with a tolerance of ±15 Myr. The Kaapvaal window for the first oxygenated air, 2.4241 to 2.368 Ga, closes on a whole-rock carbonate date for the Mooidraai Formation, whose sulfur state rests on 10 samples that Gumsley et al. (2017) tabulate with a question mark. Two further bounds constrain oxygen rather than ice: detrital uraninite and pyrite in the Mississagi Formation cap oxygen during the first Huronian interglacial below 1.53×10^{-4} of the present atmospheric level (PAL), a limit its authors call purposefully conservative (Johnson et al., 2014), and on Kola the sulfur anomaly is lost below the Polisarka diamictite, before 2.4336 Ga and before the local ice (Warke et al., 2020). The Kola glacial cycle lasted at most 9 Myr (Brasier et al., 2013; Warke et al., 2020), and if the Polisarka and Makganyene diamictites record one glaciation, as Warke et al. (2020) correlate them, the two cratons' ages conflict by at least 9.5 Myr. The conflicting pair is the tuff above the Polisarka and the youngest dated bed within the Makganyene (Senger et al., 2023): the tuff is the older of the two, and both ages come from the same chronometer. That conflict lies within the rock record itself and does not depend on the model, and we note it wherever a comparison involves the Kola ages.

How many glaciations the Transvaal records depends on the correlation of the Duitschland and Rooihoogte formations, which is not settled. In the correlation of Gumsley et al. (2017) and Millikin et al. (2024) the two formations are successive units, four Paleoproterozoic glaciations are counted across the cratons, and the sulfur anomaly returns after its first loss. In the alternative of Havsteen et al. (2023) and Beukes and Schröder (2024) the two formations are one unit traced around the basin, with a single basal diamictite deposited between 2.371 and 2.309 Ga; the loss of the anomaly is then one step, the formations record "only a single glacial event at their base, and a unidirectional trend of oxidation" (Beukes and Schröder, 2024), and no oscillation is required. We compare the model under the first correlation; four glaciations across the cratons are common to both correlations, and the model's third glaciation ends late under either (Section 4.2 of the main text). An older correlation that matched the Transvaal diamictites to the upper two of the three Huronian glacial formations gave three glaciations in all (Bekker et al., 2004; Rasmussen et al., 2013),

Table S14: The dated beds against which the model's glaciations and oxygenation are compared (Sections 4.2–4.4 of the main text, whose Fig. 3 plots every row). Each bed bounds a model date from one side, and the bound is taken at the lenient 2σ edge of the date. Only the last-deglaciation window has an age model rather than a dated bed at one edge, and the two Kola rows conflict with the Kaapvaal rows by at least 9.5 Myr, a disagreement internal to the rock record. Ages in Ma with 2σ uncertainties; bounds in Ga; PAL, present atmospheric level.

Bed (craton)	Age	Bound supplied	Source
Heynskop Fm., open water below the Makganyene diamictite (Kaapvaal)	2451.5 ± 2.5 (max. depositional)	first glaciation begins ≤ 2.454	Senger et al. (2023)
Ongeluk lavas, interfingering with the diamictite (Kaapvaal)	2425.5 ± 2.6	ice at some age in [2.4229, 2.4281]; with the Heynskop bed, first glaciation ≤ 31.1 Myr plus the lava duration	Gumsley et al. (2017)
Diamictite bed below the Ongeluk contact (Kaapvaal)	2423.1 ± 1.0	ice still depositing at ≤ 2.4241	Senger et al. (2023)
Mississagi Fm. detrital uraninite and pyrite (Superior)	first Huronian interglacial	$pO_2 < 3.2 \times 10^{-5}$ atm (1.53×10^{-4} PAL)	Johnson et al. (2014)
Hotazel Fm. Ce anomaly; none in the Mooidraai carbonates above (Kaapvaal)	Mooidraai whole-rock Pb–Pb 2394 ± 26, U–Pb 2392 ± 23	first oxygenated air in [2.368, 2.4241] (young edge a carbonate date; 10 sulfur samples, tabulated 'No MIF-S?')	Gumsley et al. (2017)
Gordon Lake Fm. tuffs above the Gowganda diamictite (Superior)	2318 ± 8; 2310 ± 5	third glaciation over by ≥ 2.310	Rasmussen et al. (2024)
Lower Timeball Hill Fm.: basal shale Re–Os; tuff (Kaapvaal)	2316 ± 7; 2310 ± 9	third glaciation over by ≥ 2.309 / 2.301; with the diamictite bed below the Ongeluk, at most 114.1 Myr from first Kaapvaal ice to the end of the third glaciation	Hannah et al. (2004); Rasmussen et al. (2013)
Upper Timeball Hill tuffs below the Rietfontein diamictite (Kaapvaal)	2266 ± 4; 2256 ± 6	fourth glaciation begins ≤ 2.262; open water after the third ≥ 48 Myr; last deglaciation ≤ 2.256	Rasmussen et al. (2013)
Hekpoort lavas above the Rietfontein diamictite (Kaapvaal)	Pb–Pb 2236 ± 38; Rb–Sr 2224 ± 21; best estimate 2247 ± 20; no igneous U–Pb	last deglaciation ≥ 2.220 (age model; ± 15 Myr tolerance specified in advance)	Altermann (2019); Schröder et al. (2016); Rasmussen et al. (2013)
Imandra lopolith below, tuff above the Polisarka diamictite (Kola)	2441 ± 1.6 (maximum age); 2434.8 ± 1.2 (± 6.6 in Warke et al., 2020)	local cycle ≤ 9 Myr; Kola deglaciation ≥ 2.4336 Ga against Kaapvaal ice at ≤ 2424.1 Ma	Warke et al. (2020); Brasier et al. (2013)
Loss of the sulfur anomaly below the Polisarka diamictite (Kola)	after 2501.5 ± 1.7, before the upper tuff	first oxygenated air on Kola in [2.4336, 2.5032], before the local ice	Warke et al. (2020)
Paleosols, iron retention (compilation)	2.2–2.0 Ga	$pO_2 \geq 0.03$ atm (0.14 PAL) reached (semiquantitative)	Rye and Holland (1998)
Paleosols, profile barometer	2.15, 2.08, 1.85 Ga	$\log_{10} pO_2$ (atm) in $[-5.0, -2.5]$, $[-5.2, -1.7]$, ≥ -4.6	Kanzaki and Murakami (2016)
Last loss of the sulfur anomaly (Kaapvaal)	∼2.22 Ga; 2.32 and 2.33 Ga in the other studies	permanence; a disagreement between studies, printed as a disagreement (Sections 1, 3.2 and 5.2 of the main text)	Poulton et al. (2021); Bekker et al. (2004); Luo et al. (2016)

and the number became four when tuff ages showed the Rietfontein diamictite to be younger than all three (Rasmussen et al., 2013). Where the number of glaciations bounds the outgassing exponent (Section 2.4 of the main text) it enters as a minimum, at least four glaciations beginning by 2.22 Ga or at least three under the older correlation, combined with the absence of any glacial deposit between 2.22 Ga and the Cryogenian, and we give the interval of the exponent under both counts.

Hoffman (2013) proposed a further correlation built on the sulfur isotope record itself, on the stated assumptions that the loss of the anomaly was a single event connected in time with one severe glaciation, under which the glacial units group into three epochs. His remark that an oscillation of the kind Claire et al. (2006) had modeled was not observed in the sulfur isotope data referred to the compilation then available, which he described as too coarse to test the connection with stratigraphic precision. The studies that report re-crossings (Luo et al., 2016; Poulton et al., 2021; Uveges et al., 2023) postdate it, and we treat his scheme as one correlation among several. Glacial deposits and returns of the anomaly can be lost from the rock record but not added to it, apart from the possibility of structural repetition considered in Section S3.3. Following the advice of one of us (D.T.J.), we therefore treat both the dated number of glaciations and the number of sulfur-state reversals as lower bounds on how many such events the transition contained, and we do not require the model to reproduce the reversal count as a total. The number of glaciations, treated as a lower bound, selects the same interval of ν as the calibration of Section 2.4 of the main text when the other inputs take their Table 1 values. At least four glaciations by 2.22 Ga require $\nu < 0.7225$, and the absence of later glacial deposits requires $\nu > 0.7075$; on the interval between these bounds the model has exactly four glaciations, because its glaciations follow one another every 68.3–72.9 Myr from a first glaciation whose date is set by continental emergence, so that a fifth would begin only after 2.22 Ga (at 2.174 Ga for $\nu = 0.705$; Section S4.1). An unrecorded glaciation is thus compatible with the calibration only if it is younger than the dated ones, and each such glaciation would shift the allowed interval of ν downward by about the interval's own width, to 0.6925–0.7075 for one additional glaciation, and would bring the model's last deglaciation to 2.15–2.17 Ga. The preservation assumption on which the lower limit of ν rests is therefore the absence of glaciation above the Hekpoort lava, which Section 5.3 of the main text lists as a test.

S3.2 The Transvaal compilation and the reversal statistic

The compilation of Uveges et al. (2023) collects 1,689 published $|\Delta^{33}S|$ measurements from the Transvaal basin with depositional ages spanning the transition, each with an analytical uncertainty and a published age interval (Fig. S1). No $\Delta^{33}S$ value entered the model's construction, and the counting rule described next was defined before the model was compared with the compilation. The treatment of the age uncertainties (one age draw per dating unit with stratigraphic order kept, in place of an independent draw per sample) and the tail probabilities used to judge synthetic histories were adopted afterwards; they affect the resolution experiment of Fig. S2 but not the comparison with the model at the dated clusters. To count changes of state we average the measurements in five-million-year bins and compare the bin means with the compilation's own high (anomaly-bearing) and low (anomaly-free) end levels, with a hysteresis band between them. We count a change of state, in either direction, when the binned series passes from one level to the other, and call the number of such changes the reversal count. A single loss of the anomaly with no return thus gives one change of state and each return followed by a renewed loss adds two; an excursion that does not reach the opposite band is not counted. The number counted at reported ages depends on the ages assigned to the samples but not on their uncertainties. To propagate the age uncertainties, in the compilation and in the synthetic compilations described in what follows, we group the samples into dating units, sets of samples whose assigned ages rest on the same age constraints (a dated formation or group of formations in the drill cores, or one outcrop series with interpolated ages; eight units when the Koegas Subgroup takes its re-dated age). For each unit we draw one age uniformly within its published limits and apply the same draw to every sample of the unit through its own interval, so that the samples of a unit move together and keep their internal order. We reject draws that violate superposition within a drill core or within a succession: the Kuruman Iron Formation below the Koegas Subgroup and both below the Ongeluk lavas at 2425.5 ± 2.6 Ma, the Mooidraai dolomite above the lavas, the Tongwane Formation and the lower Duitschland Formation below the Rooihoogte Formation, and the Tongwane and Duitschland formations below the upper Timeball Hill Formation. We take as principal the chronology in which the Koegas Subgroup is re-dated to 2450 Ma (2440–2460; Senger et al., 2023; discussed after Fig. S1) and give the compilation's published chronology as a sensitivity test. At reported ages, that is, with every sample at its assigned age and no resampling, the compilation gives 3 changes of state on the principal chronology and 7 on the published one, and under the age resampling just described a median of 5 (fifth to ninety-fifth percentile 3–7) on either. On the principal chronology the three changes are the loss of the anomaly recorded by the Tongwane and Mooidraai dolomites, which follow the anomaly-bearing Kuruman and Koegas samples, its return in the lower Duitschland and Rooihoogte samples above them, and the final loss. The number remains three when any one study or any

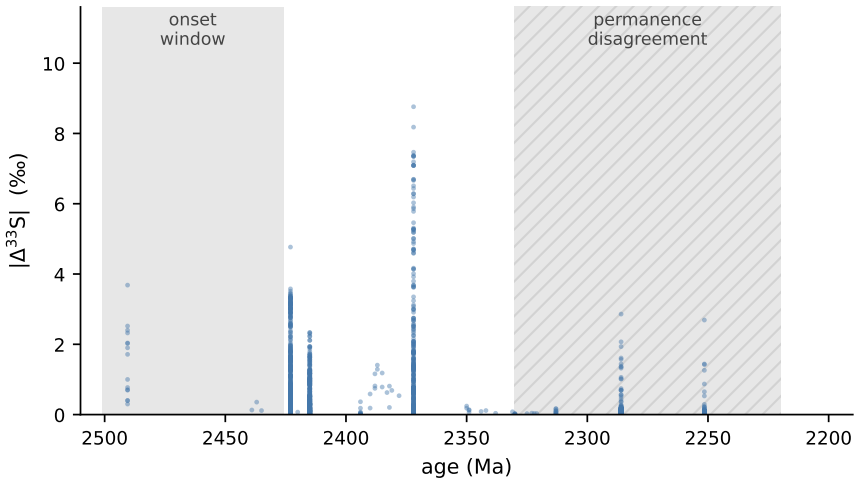

Figure S1: The 1,689 $|\Delta^{33}S|$ measurements of the Transvaal compilation of Uveges et al. (2023) at their reported ages, re-plotted with no new statistic. Most samples fall in a few age clusters, and the compilation therefore records the state of the air at only a few dated intervals. Through the transition the anomaly is lost, returns and is lost again. Shaded: the onset window, spanning the loss of the anomaly on Kola and the first Kaapvaal glaciation, and the interval over which the published permanence dates disagree (2.33 to 2.22 Ga; Table S14). Fig. 4 of the main text overlays the intervals in which the model's atmosphere permits the anomaly under two criteria for its formation.

one formation is removed from the compilation, because each change is registered by at least two dating units.

The compilation's count of changes of state rests on few of its samples, because the samples are concentrated in a small number of age clusters and facies. The 1,689 measurements share only 31 distinct reported ages and fill 20 of the five-million-year bins. Of the samples, 1,575 belong to the four largest age clusters, 22 of the 31 ages have three samples or fewer, and four of the 7 changes of state at reported ages are produced by such sparsely filled bins. On the principal chronology, likewise, each of the three changes is first registered, in order of assigned age, by a bin of seven samples or fewer (the Tongwane and outcrop Duitschland dolomites), although each is also recorded by a larger cluster (Mooidraai, Rooihoogte, Timeball Hill). Sedimentary sulfur can also inherit the anomaly of older, recycled crust, so the loss of the anomaly from sediments may lag the change in the air by 10–100 Myr (Reinhard et al., 2013); we apply a correction for this crustal memory in Section S3.4.

The reversal count also depends on the ages assigned to the Koegas Subgroup, which the compilation places at whole-rock carbonate ages of 2423 and 2415 Ma determined before the Ongeluk lavas were re-dated, whereas the subgroup lies conformably below the Makganyene diamictite (Gumsley et al., 2017) and the Heynskop age now puts it near 2450 Ma (2440–2460; Senger et al., 2023). With the 960 Koegas samples moved to the re-dated position the compilation gives 3 changes of state at reported ages instead of 7. On the published chronology four of the 7 changes of state are produced by four single dolomite samples of one study (Guo et al., 2009) whose ages interleave with the older Koegas assignments. For these reasons we use the re-dated chronology as principal, in the resolution experiment and in the comparison with the model, and report the published chronology beside it.

We measured what the reversal count can resolve on synthetic compilations built on the samples of the real one (Fig. S2). Each sample keeps its reported age, its dating unit and its analytical uncertainty, and takes the compilation's high or low $|\Delta^{33}S|$ end level according to an imposed history of anoxic and oxic intervals evaluated at its unit's drawn age; the synthetic compilation is binned at the reported ages and its changes of state are counted as for the real one. For each number k of oxic–anoxic cycles we imposed 20,000 square-wave histories at random positions through the transition (onset of oxic air uniform between 2.47 and 2.42 Ga; anoxic intervals of 10–30 Myr after oxic intervals of 20–60 Myr for $k \leq 5$, shorter for $k \geq 6$; last thaw before the compilation's youngest sample), with one age draw per unit per history. From these histories we computed the two tail probabilities of the compilation's own count k_{obs}: the probability $P(K \geq k_{\mathrm{obs}} \mid k)$ that an imposed history gives at least as many changes of state as the compilation, which is small when the compilation has more reversals than k cycles produce at its sampling, and the probability $P(K \leq k_{\mathrm{obs}} \mid k)$ that it gives at most as many, which is small when the compilation has fewer. On the principal chronology ($k_{\mathrm{obs}} = 3$) neither probability is below 0.05 for any k from one to six ($P(K \geq k_{\mathrm{obs}} \mid 1) = 0.63$; $P(K \leq k_{\mathrm{obs}} \mid k) = 0.43$, 0.14 and 0.057 for two, four and six cycles), and eight or ten short cycles are rejected at that level, though not strongly ($P(K \leq k_{\mathrm{obs}} \mid k) = 0.025$ and 0.016). A single loss of the anomaly with no

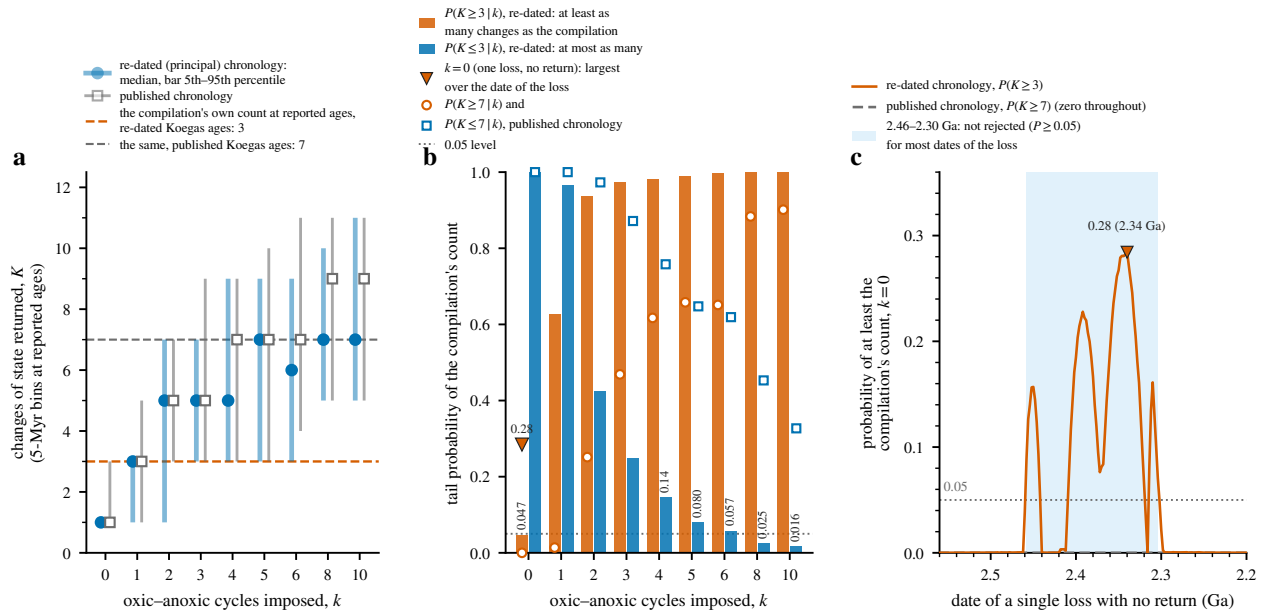

Figure S2: Resolution of the reversal statistic of Section S3.2 on synthetic compilations built on the samples, dating units and analytical uncertainties of the compilation of Uveges et al. (2023), with one age draw per dating unit and stratigraphic order kept. (a) Count of changes of state obtained when a square-wave history of k oxic–anoxic cycles is imposed at random positions through the transition (median and fifth to ninety-fifth percentile over 20,000 histories per k): filled symbols, the principal chronology, on which the Koegas Subgroup samples take their re-dated age; open symbols, the published chronology. Dashed lines mark the compilation's own count at reported ages on each chronology, 3 and 7. (b) Tail probabilities of that count under each k: on the principal chronology $P(K \geq 3 \mid k)$ (orange bars) and $P(K \leq 3 \mid k)$ (blue bars), the triangle marking the largest $P(K \geq 3)$ over the date of a single loss with no return ($k = 0$); open symbols, the same probabilities on the published chronology ($k_{\mathrm{obs}} = 7$). (c) The case $k = 0$ resolved by the date of the loss: the probability that a single loss with no return at that date gives at least the compilation's count, on either chronology; shaded, loss dates between 2.46 and 2.30 Ga. Dotted lines mark the 0.05 level. On the principal chronology no history with one to six cycles is rejected at that level, eight or ten short cycles are rejected through the lower tail only, and a single loss with no return is not rejected for most dates of the loss between 2.46 and 2.30 Ga (it is rejected for a loss dated between 2.44 and 2.41 Ga, near 2.32 Ga, or outside that range). On the published chronology a single loss with no return is rejected for every date of the loss and one cycle is disfavored ($P = 0.014$).

return gives 3 or more changes with probability 0.047 averaged over the date of the loss but up to 0.28 for particular dates: it is not rejected at the 0.05 level for most dates of the loss between 2.46 and 2.30 Ga, the exceptions being a loss dated between 2.44 and 2.41 Ga or close to 2.32 Ga. A history with a single loss can give as many changes of state as the compilation because the age limits of the Mooidraai and Rooihoogte clusters (±26 and ±56 Myr) overlap the interpolated ages of the outcrop Duitschland series (Guo et al., 2009), so that these samples, read in the order of their assigned ages, can appear to lose, regain and lose the anomaly through age misordering between sections alone. On the published chronology ($k_{\mathrm{obs}} = 7$) the same test rejects a single loss with no return for every date of the loss (not one of the 20,000 histories at any date reaches 7 changes), disfavors one cycle ($P = 0.014$ averaged over positions; individual one-cycle histories reach 0.16) and admits two to ten ($P \geq 0.25$), although four of the 7 changes there rest on the single dolomite samples noted above. At the compilation's dating resolution, therefore, the pooled reversal count does not measure the number of returns to anoxic air: on the principal chronology it can neither exclude a history without a return nor distinguish one cycle from six, and so it provides no evidence for or against the model's four glaciations and three interglacials. The evidence that the anomaly returned is stratigraphic and lies within single cores (Section S3.3); the comparison that can discriminate between histories uses the state of the air at the compilation's dated clusters.

We apply the same test to the model with 100,000 synthetic compilations in which each sample takes the high or low end level according to whether the model's air at its unit's drawn age is below or above 10^{-5} PAL. Sediment deposited under the ice is treated under two rules, either that it records the anoxic air above it or that only open water leaves a record (the unit's age is then drawn from the open-water part of its interval). On the principal chronology the model gives a median of 3 changes of state (fifth to ninety-fifth percentile 1–5) under the first rule and 1 (1–3) under the second, against the compilation's 3, with $P(K \geq k_{\mathrm{obs}}) = 0.90$ and $P(K \leq k_{\mathrm{obs}}) = 0.77$ under the first rule and $P(K \geq k_{\mathrm{obs}}) = 0.31$ under the second, so its count is

consistent with the compilation's. This agreement carries little weight, because the reversal count rejects no history with one to six cycles and because the model's changes of state are not the same events as the compilation's. In the model they are the first oxygenation at 2.353 Ga and, under the first rule, the return of anoxic air during the third glaciation, registered by the upper Duitschland and Timeball Hill samples whose age limits span it; in the compilation they are the loss of the anomaly recorded by the Tongwane and Mooidraai dolomites, its return in the lower Duitschland and Rooihoogte samples above them, and the final loss. Under the criterion of Zahnle et al. (2006) the anomaly ends in the model at 2.475 Ga (2.458 Ga in the methane-only case of Section S1.3), before deposition of the anomaly-bearing Koegas Subgroup, and does not return, because methane later remains below 8 ppmv; the model's synthetic compilations then have one change of state or none in nearly every draw, and that history is excluded by the compilation's 3 changes ($P(K \geq k_{\mathrm{obs}}) = 2 \times 10^{-4}$). This exclusion and the model's mismatch at the anomaly-bearing Koegas clusters under this criterion, in the comparison at the dated clusters, are one discrepancy, since both follow from the anomaly ending before the Koegas Subgroup was deposited. On the published chronology the model has fewer changes of state than the compilation's 7 under either rule and either criterion ($P(K \geq k_{\mathrm{obs}}) \leq 1 \times 10^{-4}$) and is excluded there, together with every history whose transitions do not fall among the interleaved Koegas and dolomite ages. When the age uncertainty is also propagated into the compilation's own count, by binning the real and the synthetic compilations at the same drawn ages, the probability that the model shows at least as many changes as the compilation is 0.33 on the principal chronology and 0.13 on the published one, neither of which is below 0.05.

When the model is compared with the state of the air at each of the compilation's dated sample clusters, the outcome depends on a single property of the model, the anoxic first interglacial. For each reported age with at least 10 samples we draw true ages within the published intervals and compare the model's anoxic fraction over the draws with the compilation's binned state at that cluster, counting a cluster only where the model is in one state for at least nine draws in ten. Under the oxygen-only criterion for an anomaly-forming atmosphere (oxygen below 10^{-5} PAL) the model matches 4 of 5 single-state clusters, namely the Kuruman cluster and the two Koegas Subgroup clusters, anomaly-bearing in the compilation and anoxic in the model on either chronology, and the youngest Timeball Hill cluster, anomaly-free in both. The one mismatch is the 10-sample Mooidraai cluster at 2394 ± 26 Ma, which is tabulated as anomaly-free and falls inside the model's first interglacial; the anoxia of that interglacial in the model also accounts for the late onset of oxic air reported in Section 4.3 of the main text. Under the criterion of Zahnle et al. (2006), which also requires methane at or above 8 ppmv in open water, the model matches 4 of 7 clusters on the published chronology, with the Mooidraai cluster matched and the three anomaly-bearing clusters younger than 2.475 Ga (2.458 Ga in the methane-only case), when the model's methane collapses below that level, mismatched instead. On the principal chronology the model matches 4 of 6 clusters under that criterion, the mismatched anomaly-bearing clusters being those at 2450 and 2372 Ma. It is not established whether the part of the volcanic hydrogen supply that methanogens do not convert to methane would keep that criterion satisfied after the collapse; if it does not, the methane criterion then reduces to the oxygen-only one.

S3.3 Per-core and paired counts

The pooled compilation includes a disagreement between drill cores as part of its variance, so we also give the changes of state counted in each core beside the pooled count. At reported ages on the published chronology six of the seven pooled changes of state are formation-to-formation changes across cores before and during Rooihoogte time. When changes of state are counted along the depth axis of a single core on a thirty-meter grid, core EBA-2 gives seven (fifth to ninety-fifth percentile seven to nine at one position of the grid, and five to seven across grid positions), with its reversals after Rooihoogte time. The neighboring cores KEA-4 and EBA-1 give one change at the same resolution (EBA-1 one to three across grid positions), so no single core shows, at that resolution, the oscillation implied by the pooled count. We take the core-resolved studies as the evidence that the reversals before and during Rooihoogte time are real (Poulton et al., 2021; Uveges et al., 2023), whereas the reappearances of the anomaly after Rooihoogte time rest on one core, and closely spaced neighboring cores do not show them at the same resolution (Izon et al., 2022; Uveges et al., 2023; Millikin et al., 2024). Thallium isotopes from the same core corroborate the reversal at the Rooihoogte–Timeball Hill boundary in the ocean (Ostrander et al., 2024), and the paired count, sulfur and thallium changing state together, is defined only in that boundary interval, where it is two. Higher in the core those authors regard their samples as unreliable seawater archives, so the Timeball Hill Δ^{33}S reversals cannot be tested against an ocean proxy there (cf. Heard et al., 2025).

The dated loss of the sulfur anomaly and the later report of repeated crossings in the Rooihoogte and Timeball Hill formations both come from one drill core, EBA-2. The study that dated the loss of the sulfur anomaly to 2.32 Ga rests on seven pyrite samples (twenty spot analyses) from 3.6 m of core EBA-2 (Bekker et al., 2004), and the later studies that reported the threshold crossed and recrossed sampled the same core

more densely at overlapping depths, over the whole formation rather than one boundary interval (Poulton et al., 2021; Uveges et al., 2023). Because both results come from the same core, independent confirmation of either is scarcer than the citation record suggests (Section 3.2 of the main text, following D. T. Johnston), and this applies to the reversal counts used here as much as to any published position.

The per-core count for EBA-2 rests on a stratigraphic premise that no geochemical criterion in this work can test, namely that the counted interval of the core is structurally intact. A bedding-parallel thrust with no fault rock would leave a depth series indistinguishable from stratigraphy, and a reversal repeated by it would be counted twice. None of the published descriptions of the Carletonville cores that we have read reports a fault or a repeated interval in EBA-2 (Luo et al., 2016; Poulton et al., 2021; Izon et al., 2022; Ostrander et al., 2024), although the unpublished stratigraphic reports they cite were not available to us. The one thrust repetition documented in these units that we have found is at the Duitschland Formation outcrop on the farm Langbaken in the eastern Transvaal (Warke and Schröder, 2018). A core log for the counted interval of EBA-2, with bedding angles and fault-rock notes, would settle the question, and none has been published. D. T. Johnston raised the possibility without favoring it; we do not adopt it, but it qualifies the per-core and paired counts wherever they are used.

S3.4 Western Australia

The Turee Creek Group of Western Australia, deposited in a second basin, also records the loss of the anomaly as a series of episodes. In sections of that group dated by U–Pb and Re–Os geochronology the anomaly is preserved in sulfides from about 2.45 Ga to beyond 2.31 Ga "punctuated by several episodes of MIF-S disappearance," and the episodes are asynchronous between South Africa, North America and Australia (Philippot et al., 2018). Those authors interpret the late, asynchronous signals as sulfur weathered from older anomaly-bearing crust rather than as a record of the contemporary air, and under that interpretation the Western Australian sections constrain the timing of atmospheric oxygenation less directly than the Transvaal and Huronian successions do. We therefore claim only that the two basins agree in recording a punctuated transition with reversals; this concordance is consistent with the model's oscillatory transition and places no constraint on the number of its cycles.

We tested the agreement between the two basins numerically once, and the result is inconclusive. On a Western Australian subseries of the same compilation, 1,253 measurements with published per-sample ages (Uveges et al., 2023), the reversal statistic gives a median of four changes of state at reported ages and ten when each sample's age is resampled independently within its interval, inside the range the Transvaal series gives under the same treatment. Under a correction for crustal memory, in which each sample may carry sulfur recycled from older crust with a mixing probability of one half (a neutral value, adopted after the statistic had been fixed), the Western Australian count falls to zero at reported ages and to one under that resampling, while the Transvaal reported-age count is unchanged. That contrast appears to be a property of the correction when the sample ages take only a few formation-level values, as they do in the Western Australian sections, rather than a difference between the basins, because a synthetic three-reversal history imposed at those ages is erased by the same correction while the uncorrected statistic recovers it. Sample ages resolved within the formations, a subseries from deeper drilling insensitive to recycled sulfur, or a measured mixing probability would settle the comparison. For these reasons, and following D. T. Johnston's advice that the Western Australian record is secondary for timing, the second-basin test in Table 2 of the main text is aimed at the Huronian Supergroup, where detrital minerals and sulfur isotopes in the first interglacial can be dated against the Gowganda and Gordon Lake beds.

S3.5 Step counts under two mid-Proterozoic ceilings

Whether the oxygen proxies after the transition imply more than one oxygenation step depends on which upper limit is adopted for mid-Proterozoic oxygen. After the transition the paleosol compilation of Rye and Holland (1998) puts oxygen at or above 0.03 atm (0.14 PAL) at some time between 2.2 and 2.0 Ga, a semiquantitative floor. Through the middle Proterozoic the strictest bound comes from a measurement: chromium isotopes in ironstones cap atmospheric oxygen at 10^{-3} PAL for most of a billion years (Planavsky et al., 2014b). The loosest is a model-based bound that the same paper cites as the most widely accepted upper limit, about 0.4 PAL. We retain the full range between these two limits, and a point estimate from redox-sensitive metals with a model conversion, a few percent of the present level, falls inside it (Zhang et al., 2016). In the Phanerozoic the continuous charcoal record implies oxygen at a large fraction of the present level.

We count a step as a transition to a new persistent state. Under the strict limit, the chromium ceiling, at least two separated upward steps are forced by measured and semiquantitative bounds alone, because oxygen reaches about 0.14 PAL after the transition, remains at or below 10^{-3} PAL through the middle Proterozoic,

and is near modern levels in the Phanerozoic. The same bounds require a fall of about two orders of magnitude into the middle Proterozoic, and a one-step history is excluded. Under the loose limit, the model-based ceiling near 0.4 PAL, a single protracted rise that begins with an oscillatory transition is consistent with every measured constraint, and the only statements inconsistent with it are qualitative estimates such as the judgment of Holland (2006) that mid-Proterozoic oxygen "did not change significantly." The mid-Proterozoic upper limit is therefore the largest open uncertainty in the later oxygen record, and apart from the choice between one step and two, which depends on the limit adopted, the proxies do not resolve the number of steps under either limit. A reversal does not by itself begin a new persistent state and is not a step: the resolved re-crossings of the threshold during the transition, the compilation's changes of state and the model's returns to anoxia under each of its four glaciations all describe the oscillation within the transition, and none of them enters a step count anywhere in this work. The Paleoproterozoic record does resolve repeated fast crossings of the threshold sustained over an era of roughly two hundred million years (Luo et al., 2016; Poulton et al., 2021), and a model of the transition must produce both the repetition and the speed.

S3.6 Comparisons fixed in advance and the reproducibility check

Before the integrations reported in this work were made we fixed four things, and none was changed afterwards. The first was the set of bed ages of Section S3.1, with the one-sided bound each bed supplies and the tolerance on the permanence date. The second was the list of 60 comparisons, each written as one row giving the model quantity, the rule and its direction, the bed or proxy that fixes it, and its status. The third was the solver, the code that makes the comparisons, the search procedure for the outgassing exponent, and the closed list of integrations to be made. The fourth was the value that an earlier integration of the same equations with the same inputs had given in every comparison (4,055 entries over 53 parameter sets), together with a statement naming the five comparisons independent of the glaciation count that the model was expected to fail. The fourth item is a check of numerical reproducibility and of the integrity of the archived code and inputs, and it is not a prediction: the equations had been integrated, and their behavior examined, while the model was being assembled, and the comparisons were written with that behavior known. Fixing the first three items in advance ensured that no bound, criterion or tolerance was adjusted to the outcome, and we claim no more for it. The status assigned to each comparison indicates whether its model side is independent of the glaciation count, in which case the comparison is a test of the model, or is a quantity that follows from that count to first order (the count itself, the permanence date, the spacings and the third interglacial). The remaining statuses mark the target of a prescribed date, an input or present-day identity, a comparison internal to the rock record, and a comparison whose outcome depends on the sulfur criterion.

The search procedure for the exponent was automatic, and we tested it first on synthetic profiles of the number of glaciations against ν. Starting from $\nu = 0.715$, it integrates the model on a grid of spacing 0.0025 in ν, steps outward on a fixed schedule while the number of glaciations is wrong (a total above four raises ν; any other wrong count lowers it), and bisects each edge of the four-glaciation block to 0.005, making no more than 28 integrations in all. The midpoint of the two edges is taken as the principal value. The integrations at $\nu = 0.705$, 0.710, 0.725 and 0.720 give five, four, three and four glaciations (at 0.705 one of the five begins after 2.22 Ga), so the four-glaciation interval is $(0.7075, 0.7225)$ with midpoint 0.715, and we use its two edge values 0.71 and 0.72 in every comparison as the uncertainty band of ν. We applied the same procedure to each alternative family (the model with one input changed and ν fixed again by the glaciation count). A family for which the search ends without finding four glaciations is reported as one for which no four-glaciation exponent was found from that starting value, which does not show that none exists. The closed list of integrations comprised the principal family, 17 alternative families (Supplementary Text S4), 31 single-input changes at the principal exponent, and four repeated integrations that had to reproduce the earlier outputs of the same equations identically before anything was compared. In all we made 210 integrations, of which 208 ran to completion; the integrations for the two sub-ice venting changes did not finish under the first integrator and were completed with the second integrator (Supplementary Text S1), and are labeled so wherever they appear.

The model does not meet the full set of comparisons: over the four-glaciation interval the five comparisons named in advance, whose model side does not follow from the glaciation count, fail (Tables S15–S18). The model also misses the Makganyene diamictite age, by 1.0 Myr at the central crossing epoch though not at the young end of the onset window, and under the oxygen-only criterion its MIF-S anomaly is lost too late for the Kaapvaal and Kola constraints on the onset of oxygenation (Table S16). Three of the five are the comparisons of surface oxygen between 2.2 and 2.0 Ga with the paleosol floor of Rye and Holland (1998), of the end of the third glaciation with the Gordon Lake and lower Timeball Hill dates, and of the end of the last glaciation with the Hekpoort age model, which fails over part of the interval only. The first and third of these were given the status of tests independent of the glaciation count when the comparisons were written. The first keeps that status: because the model has no redox feedback after the crossing epoch

$t_{\times}$, the oxygen level after the transition is set by two prescribed schedules (Section 4.4 of the main text), and the comparison with the paleosol floor of Rye and Holland (1998), which the model fails, therefore tests those post-transition inputs rather than the transition dynamics. The proxies for that interval are themselves divided, since the weathering-barometer windows of Kanzaki and Murakami (2016) contain the model value that the floor excludes, and Table S18 gives both comparisons. The third, the end of the last glaciation, is also the permanence date, which follows from the glaciation count (Table 2 of the main text), and for that reason alone we do not offer it as a test in the main text; Table S15 keeps the status it was given and notes this. The remaining two of the five failed comparisons are those of Archean and earliest-Proterozoic carbon dioxide with the estimate of each of the two paleosol barometer schools, which disagree with each other. The repeated integrations reproduced every earlier value for the principal parameter set. One defect was found among the expected values and corrected without a new integration: for two edge values of ν in one alternative family the expected dates had been taken from an earlier integration made with the second integrator instead of the first. As a result five of 3,951 compared entries differed by the spread between the two integrators. After the expected dates for those two edge values were relabeled, with no other change, 3,925 entries were compared and none differed, and every other outcome was unchanged.

Each value of ν fixed by the glaciation count (in the principal family and in each alternative family) and both edges of its four-glaciation interval were also integrated twice, with independent stiff methods (a variable-order backward-differentiation integrator and an implicit Runge–Kutta integrator; Supplementary Text S1). The two integrators agree to 10^{-6} Gyr in every glacial entry and exit and in the permanence date. In the date of first oxic air they agree to 0.25 Myr at the principal value and to within 0.5 Myr at every other value and edge except the exponent of the calcite-saturation partition family, where they differ by 0.54 Myr. The comparison was also repeated independently: 17 integrations covering every kind of parameter set were rerun from a copy of the solver and reproduced the original outputs identically, and the comparisons for four parameter sets, recomputed from the raw outputs, agreed with the original in all 96 entries except one rounding difference. The model code, the input tables (including the bed ages and the expected values), the comparison code and the model output behind every table here accompany this submission as a supplementary archive and will be deposited in a public repository, with a DOI added to the Data availability statement of the main text, on acceptance. Tables S15–S20 give every comparison with its status (the glacial chronology, the sulfur isotope record, the model atmosphere at standard epochs, the oxygen and carbon dioxide levels together with the Neoproterozoic durations and the modern budget terms, and each model statement with the measurement that tests it), and Table 2 of the main text summarizes them. In every table a row whose model side follows from the glaciation count is marked so and is not evidence for the model whatever its outcome, and "test" marks a comparison whose model side does not follow from that count.

S3.7 Integrations made after the comparison

Everything reported in Supplementary Texts S4–S6, and the sweep of the outgassing exponent across its published range used in Section 2.4 and Fig. 6 of the main text, was integrated after the comparison of Section S3.6 had been fixed and carried out, and forms no part of it. These later integrations used the same solver as the comparison (checksum prefix 7f22baa4), which reproduces the principal integration of the comparison identically at the principal exponent. The three added inputs they vary (the date of the reductant step under earlier emergence, the imposed burial excursion of Supplementary Text S5, the interpolation between the two tabulated nitrogen inventories) leave the trajectory unchanged at their default values. In the sweep we integrated the model at 298 parameter sets, reused 24 of the comparison's own integrations, counted glaciations with the comparison's criteria, and located every change in the number of glaciations under the principal assumptions to within ± 0.0025 in ν (the upper edge of the three-or-four interval to within ± 0.00125). We drew the Latin-hypercube samples of Supplementary Text S4 with random seeds recorded before any sample was integrated, and where the sub-ice venting fraction is nonzero the second integrator replaces the first, as in the comparison. None of these integrations adds a comparison, moves a bound or changes an outcome of Section S3.6. They give the interval of the exponent allowed under each statement of the rock record and the ranges of the model's dates across that interval, and they show whether the glacial era persists when the assumptions are varied jointly, where the prescribed crossing epoch falls relative to the first glaciation, and how the imposed burial excursion affects the model's glacial chronology and oxygen. The alternative treatments of the hydrogen budget in Supplementary Text S1 (Section S1.3) and the sub-ice carbon cases and thaw treatments of Table S5b–e were also integrated after the comparison, each with a copy of the solver that differs from it only in the treatment being varied and that reproduces the principal integration identically when the adopted treatment is restored. Like the other later integrations, they add no comparison and change no outcome of Section S3.6.

Table S15: The model's glacial chronology compared with the dated beds. The largest discrepancy is at the end of the third glaciation, 20.7 Myr after the Gordon Lake and lower Timeball Hill bound; the first glaciation contains the Ongeluk age and fits inside the Kaapvaal duration bound, and the fourth begins after the upper Timeball Hill tuffs; none of these outcomes follows from the glaciation count. With the sub-ice carbon kept in ocean crust instead of being returned at the thaw, four glaciations still occur, and which dated beds are met varies with ν inside the four-glaciation interval of that case. Under crustal storage the third glaciation ends inside the Gordon Lake bound except near the upper edge of that interval, where it is 2.0 Myr late, and the fourth begins after the upper Timeball Hill tuffs only near that edge (Supplementary Text S1, Table S5c; Table 3 of the main text). "Rock record" gives the one-sided bound and the bed that supplies it (ages in Ma with 2σ uncertainties; sources in Table S14); "model" gives the value at $\nu = 0.715$ with, in parentheses, its range over the four-glaciation interval $\nu = 0.71$–0.72. "Status" is "test" where the model side is independent of the glaciation count that fixes ν; otherwise it states that the model side follows from that count to first order (or is the count itself) or is the target of a prescribed date. Rows that follow from the count and targets of prescribed dates are not evidence for the model whatever their outcome.

comparison	rock record (bound; bed)	model	outcome	status
glaciations beginning by 2.22 Ga; after it	four dated glacial units, Transvaal–Huronian correlation; none younger (Gumsley et al., 2017; Poulton et al., 2021)	four; none	holds by construction	the count itself, which fixes ν
first glaciation begins	$\leq$ 2.454 Ga (Heynskop maximum depositional age 2451.5 ± 2.5; Senger et al., 2023)	2.4509 (2.4505–2.4513)	met	target of the prescribed emergence date
ice at the Ongeluk age	overlaps 2425.5 ± 2.6 (lava in the diamictite; Gumsley et al., 2017)	2.4509–2.4251	met at every value (depends on the prescribed dates)	test
Makganyene ice still depositing	ends $\leq$ 2.4241 Ga (diamictite zircons 2423.1 ± 1.0; Senger et al., 2023)	2.4251 (2.4249–2.4254)	missed by 1.0 Myr; met with the crossing epoch at 2.43 or 2.44 Ga	test
first glaciation length, Kaapvaal	$\leq$ 31.1 Myr + lava duration (Heynskop to Ongeluk young edges)	25.7 (25.6–25.9)	met by 5.4 Myr at every value	test
first glaciation length, Kola	$\leq$ 9 Myr (after 2441 ± 1.6, before the tuff 2434.8 ± 1.2 above; Warke et al., 2020; Brasier et al., 2013)	25.7	not met ($\times$2.9)	internal to the rock record (Kola against Kaapvaal $\geq$ 9.5 Myr); not predicted
third glaciation over	$\geq$ 2.310 Ga (Gordon Lake 2318 ± 8, 2310 ± 5; lower Timeball Hill 2316 ± 7, 2310 ± 9; Rasmussen et al., 2024; Hannah et al., 2004; Rasmussen et al., 2013)	2.2893 (2.2863–2.2919)	missed by 20.7 Myr (13–27 over the four-glaciation interval and the crossing-epoch window; 18–44 over the three-or-four interval)	test; the largest miss
Makganyene ice to third glaciation over	$\leq$ 114.1 Myr (the two bounds above)	135.8	missed by 21.7 Myr	test (the same fact)
fourth glaciation begins	$\leq$ 2.262 Ga (upper Timeball Hill tuffs 2266 ± 4, 2256 ± 6 below the Rietfontein diamictite; Rasmussen et al., 2013)	2.2405 (2.2324–2.2461)	met by 21.5 Myr at every value	test
third interglacial	$\geq$ 48 Myr (lower Timeball Hill Re–Os to upper tuffs)	48.8 (45.8–53.9)	met over part of the interval	follows from the count
start-to-start spacing	median in 62–73 Myr (spacing implied by the four-glaciation chronology of Gumsley et al., 2017)	69.1, 68.3, 72.9 (median 68.1–70.3)	met	follows from the count
last glaciation over	in $[2.220, 2.256]$ Ga (Hekpoort lava above: age model, no igneous U–Pb; tuff 2256 ± 6 below; Rasmussen et al., 2013; Schröder et al., 2016; Poulton et al., 2021)	2.2169 (2.2089–2.2223)	missed by 3.1 Myr at $\nu = 0.715$; met at $\nu = 0.71$	given the status of a test in advance; the date is the last thaw of the permanence row, which follows from the count (Table 2 of the main text); the missed edge is an age model
permanence date	2.22 Ga (Poulton et al., 2021) against 2.32 and 2.33 Ga (Bekker et al., 2004; Luo et al., 2016): a disagreement, printed	2.217 (2.2089–2.2223)	3.1, 103, 113 Myr younger	follows from the count (the last thaw)
the Makganyene zircons, Gordon Lake, Timeball Hill interval and Hekpoort together	all four bounds at once		met by no parameter set of any family	test

Table S16: The sulfur isotope comparisons; conventions as in Table S15. Only two features of the model, the anoxic first interglacial and the date of first oxic air, can be tested against the compilation, whose reversal count neither resolves the number of cycles nor, on the principal chronology, excludes a history without a return of the anomaly. Under the oxygen criterion the model's date is later than the Kaapvaal and Kola constraints allow, and under the methane criterion it falls within the Kola constraint. The first seven rows all depend on one property of the model, the anoxic first interglacial, and are not independent tests. Outcomes are given under the oxygen-only criterion for an anomaly-forming atmosphere (Pavlov and Kasting, 2002) unless a row names the methane criterion (Zahnle et al., 2006).

comparison	rock record (source)	model	outcome	status
first air $\geq 10^{-5}$ PAL, Kaapvaal	in [2.368, 2.4241] Ga: after the Makganyene zircons, before the Mooidraai Pb–Pb age 2394 ± 26 Ma ('No MIF-S?'; Gumsley et al., 2017)	2.353 (2.3507–2.3554; across the crossing-epoch window 2.341–2.365)	missed by 15 Myr (13–17; 3–27)	test; criterion- and input-dependent (met at the light end of the δ_{in} band over part of that family's four-glaciation interval)
first oxic air, Kola	before 2.4336 Ga and before the local ice (Warke et al., 2020; Brasier et al., 2013)	2.353; under the methane criterion 2.475 (2.458 in the methane-only case)	missed; met under the methane criterion	criterion-dependent; ordering conflict internal to the rock record
state at dated clusters ($n \geq 10$)	compilation of Uveges et al. (2023); Koegas re-dated (Senger et al., 2023)	4 of 5 single-state clusters	misses the Mooidraai cluster ($n = 10$)	criterion-dependent (methane criterion 4 of 7)
reversal count through the compilation's binning, re-dated chronology (principal)	3 at reported ages (960 Koegas samples at 2450 Ma; Senger et al., 2023); 5 (3–7) under one-draw-per-unit age resampling	median 3 (1–5); $P(K \geq k_{obs}) = 0.90$, $P(K \leq k_{obs}) = 0.77$; open-water rule $P(K \geq k_{obs}) = 0.31$	consistent; excluded under the methane criterion ($P(K \geq k_{obs}) = 2 \times 10^{-4}$)	weak test: the reversal count rejects no history with one to six cycles
same, published chronology	7 (Uveges et al., 2023); four of them on single samples (Guo et al., 2009)	median 3 (1–5); $P(K \geq k_{obs}) \leq 1 \times 10^{-4}$	fewer than the compilation: excluded on that chronology	superseded chronology; sensitivity only
first interglacial against detrital uraninite	$< 1.53 \times 10^{-4}$ PAL (Johnson et al., 2014; Gumsley et al., 2017)	$\leq 4.8 \times 10^{-6}$ (4.3×10^{-6}–5.2×10^{-6})	met ($\times 0.03$)	test; the same fact as the first row
Hotazel-time oxidation pulse	Mn and Ce oxidation directly above the Ongeluk (Gumsley et al., 2017)	none ($O_2 \leq 4.8 \times 10^{-6}$)	not produced	not predicted
crossing speed at the threshold		25 decades per Myr	fast	a property of the ice lid, not a test

Table S17: The model atmosphere at standard epochs at $\nu = 0.715$ (open-water values; under the ice the air holds no oxygen or methane by the sub-ice assumption of Section 2.3 of the main text), with the oxygen-independent sink S of equation (4) of the main text and its shortfall below the flat gross burial $N_A = 2.07$ Tmol yr^{-1}, which sets the oxygen level after the transition. In the Archean rows methane is near three hundred ppmv and carbon dioxide lies between the estimates of the two paleosol schools. Methane is given under the escape assumption of Section 2.2 of the main text; in the methane-only case of Section S1.3 it is 558 ppmv in the two oldest rows and 8.8 ppmv at 2.46 Ga. The oxygen values in the rows after the last thaw follow from two prescribed schedules with no redox feedback, and at 2.2 and 2.0 Ga they fail the comparison with the paleosol floor and lie inside the weathering-barometer windows (Table S18). Oxygen as a fraction of the present atmospheric level, carbon dioxide in multiples of pre-industrial, methane in ppmv, S in Tmol yr^{-1}; the last column names the proxy each row meets or misses (Table S18).

epoch (Ga)	O_2	CO_2	CH_4	S	$(N_A - S)/N_A$	against
2.9	$< 7.1 \times 10^{-11}$	143	279			
2.7	$< 7.1 \times 10^{-11}$	112	279			CO_2 10–50, mass-balance school (Driese et al., 2011): misses
2.6	$< 7.1 \times 10^{-11}$	104	152			
2.46	$< 7.1 \times 10^{-11}$	69	4.4	2.07	0	CO_2 160–490, inversion school (Kanzaki and Murakami, 2015): misses
2.2	6.3×10^{-5}	71	0.016	2.00	3.1 %	$O_2 \geq 0.14$ (Rye and Holland, 1998): misses by $\times 800$; Kanzaki and Murakami (2016) windows at 2.15–1.85 Ga: met
2.0	1.7×10^{-4}	37	0.026	1.96	5.2 %	
1.8	3.1×10^{-4}	27		1.93	7.0 %	$O_2 < 10^{-3}$ (Planavsky et al., 2014b): below (set by the two schedules)
1.4	6.0×10^{-4}	14.6	0.026	1.87	9.7 %	CO_2 4.9–19.7 (Park et al., 2025): inside (schedule)
1.0	5.4×10^{-4}	7.3		1.88	9.2 %	
0.72	0.035	4.3				Neoproterozoic productivity schedule (input)
0	1.000	1.001	0.70	1.82		present-day identities

Table S18: The oxygen and carbon dioxide comparisons, with the Neoproterozoic durations and the modern budget terms; conventions as in Table S15. The model misses the paleosol oxygen floor after the transition by a factor of about 800, and its Archean carbon dioxide lies between the estimates of the two paleosol schools and meets neither. The Marinoan duration is met when the model's sub-ice carbon rule is applied at the Marinoan onset, and the Sturtian duration is not reproduced. Rows marked identity, calibration, schedule or internal to the rock record do not test the model whatever their outcome; the oxygen rows after the transition test the two prescribed post-transition schedules rather than the transition dynamics; paired rows (two barometer schools) are never averaged.

comparison	rock record (source)	model	outcome	status
O_2 at 2.2–2.0 Ga, paleosols	$\geq$ 0.14 PAL (Rye and Holland, 1998)	$\leq 1.7 \times 10^{-4}$ (1.7×10^{-4}–1.8×10^{-4})	missed (×800 short)	test, specified in advance; failed; the level is set by two prescribed post-transition schedules with no redox feedback, so the failure bears on those inputs (Section 4.4 of the main text); paired with the next row, never averaged; the model has no oxygen-overshoot mechanism
O_2 at 2.15, 2.08, 1.85 Ga	$\log_{10} pO_2$ windows (Kanzaki and Murakami, 2016)	−4.74, −4.58, −4.24	met (low side)	partner of the row above
O_2 1.8–0.85 Ga	$< 10^{-3}$ PAL (Planavsky et al., 2014b)	3.1×10^{-4}–6.0×10^{-4}	below	set by the two post-transition schedules (given that status in advance); below the ceiling
CO_2 2.70–2.68 Ga	10–50 (Driese et al., 2011)	110–112	missed (×2.2 above)	test; paired with the next row
CO_2 2.475–2.44 Ga	160–490 (Kanzaki and Murakami, 2015); per profile 25–370	67–73	missed (×0.46 of the bottom)	partner of the row above
CO_2 1.42–1.38 Ga	4.9–19.7 (Park et al., 2025)	14.2–15.1	inside	schedule
carbonate $\delta^{13}C$ before 2445 Ma	within ±2 per mil (Edmonsond and Dyer, 2026)	−1.0 to −0.3	inside	calibration of the burial flux
Lomagundi–Jatuli excursion	+7.9 per mil at its peak (Edmonsond and Dyer, 2026)	+0.29	absent	not predicted (no internal mechanism)
Marinoan duration (same sub-ice rule at its onset)	4–15 Myr (Hoffman et al., 2017)	5.1	met	one check; degenerate along the partition family; nothing set on it
Sturtian duration	57–59 Myr (Hoffman et al., 2017)	5.3	×0.09	not reproduced; not predicted
modern volcanic reductant sink	2.4 ± 1.8 Tmol yr^{-1} (Holland, 2002)	1.82	inside (−0.32 σ)	not set by construction; follows from two published inputs
modern kerogen oxidation	7.5 ± 2.5 Tmol yr^{-1} (Holland, 2002)	8.19	inside (+0.27 σ)	identity (amplitude fixed by the present-day steady state); reproduces Holland's estimate within its uncertainty
O_2, CO_2, burial, CH_4 lifetime today		1.000, 1.001, 10.0, 8.8 yr	by construction	identities

Table S19: Model statements about the transition's ice and oxygen with the measurements that test them (the full form of the upper half of Table 2 of the main text). Each row gives a model quantity at $\nu = 0.715$ (with ranges over the four-glaciation interval where they affect the outcome), whether it follows from the glaciation count, the published measurement that tests it, and the outcome where one exists. The first glaciation's duration and its ice at the Ongeluk age, the anoxic first interglacial and the start of the fourth glaciation are met and do not follow from the glaciation count; the third glaciation ends late and the Hotazel oxidation pulse is not produced. Rows that follow from the count are not evidence for the model whatever their outcome. Bed ages as in Table S14; O_2 in units of the present atmospheric level (PAL). Rows six to nine are on the following page.

model statement	follows from the count?	deciding measurement	outcome
Four glaciations begin before 2.22 Ga and none after; the last thaw, which is the permanence date, falls at 2.217 Ga (2.2089–2.2223 over the four-glaciation interval; 2.209–2.283 over the three-or-four interval).	yes: the glaciation count fixes ν, and the date follows from it	a fifth Paleoproterozoic glacial unit, or any glacial deposit or return of the sulfur anomaly dated after 2.22 Ga, on the Kaapvaal-correlated frame	met by construction; not evidence
Each glaciation lasts 23.6–25.7 Myr.	no; assumption-dependent (set by the sub-ice partition and the exit level: 18.5–25.9 Myr across the partitions with an exchangeable store of Marinoan scale, about 10 Myr at the seawater-chemistry corner)	a glacial termination dated at the contact; Kaapvaal: onset after the Heynskop maximum depositional age 2451.5 ± 2.5 Ma, ice at the Ongeluk age 2425.5 ± 2.6 Ma, so at most 31.1 Myr plus the lava's duration (Senger et al., 2023; Gumsley et al., 2017); Kola: at most 9 Myr between the 2441 ± 1.6-Ma Imandra lopolith and the 2434.8 ± 1.2-Ma tuff (Warke et al., 2020; Brasier et al., 2013)	Kaapvaal met (25.7 Myr); Kola not met, and Kola conflicts with Kaapvaal by at least 9.5 Myr in the rock record itself
The first glaciation runs 2.4509–2.4251 Ga.	onset is the target of the prescribed emergence date; end, no	Heynskop ≤ 2.454 Ga; Ongeluk 2425.5 ± 2.6 Ma inside the ice; diamictite 2423.1 ± 1.0 Ma still under ice (Senger et al., 2023)	first two met; the diamictite date missed by 1.0 Myr at the central crossing epoch, met at its young end
Ice-free intervals of 43.4, 43.7 and 48.8 Myr; start-to-start spacing 68.3–72.9 Myr.	yes	Timeball Hill open-marine interval $\geq$48 Myr between the 2316 ± 7 Ma shale and the 2256 ± 6 Ma upper tuff (60 Myr between central ages) (Hannah et al., 2004; Rasmussen et al., 2013); start-to-start spacing 62 to 73 Myr implied by the four-glaciation chronology of Gumsley et al. (2017)	met over part of the four-glaciation interval; not evidence
The third glaciation ends at 2.289 Ga (2.2834–2.2969 over the four-glaciation interval and the crossing-epoch window; 2.266–2.292 over the three-or-four interval).	no	Gordon Lake tuffs 2318 ± 8 and 2310 ± 5 Ma above the Gowganda (Rasmussen et al., 2024); lower Timeball Hill 2316 ± 7 Ma (Re–Os) and 2310 ± 9 Ma (tuff), diamictite-free (Hannah et al., 2004; Rasmussen et al., 2013): ice gone by 2.310 Ga	**missed** by 20.7 Myr at $\nu = 0.715$, by 13–27 Myr over the four-glaciation interval and the crossing-epoch window, and by 18–44 Myr over the three-or-four interval; the largest miss

Table S19: (continued) Model statements about the transition's ice and oxygen, rows six to nine; columns as on the previous page.

model statement	follows from the count?	deciding measurement	outcome
The fourth glaciation begins at 2.2405 Ga and ends at 2.217 Ga.	onset: no (the glaciation exists for $\nu < 0.7225$ only); end: yes, the last thaw of the first row	upper Timeball Hill tuffs 2266 ± 4, 2256 ± 6 Ma below the Rietfontein diamictite (Rasmussen et al., 2013): onset $\leq$ 2.262 Ga; Hekpoort lava above it, dated only by an age model near 2.220 Ga (Schröder et al., 2016): end in $[2.220, 2.256]$	onset met; end missed by 3.1 Myr at $\nu = 0.715$, met at the interval's lower edge; an igneous U–Pb age on the Hekpoort decides
The first ice-free interval (2.4251–2.3818 Ga) is anoxic: $O_2 \leq 4.8 \times 10^{-6}$ PAL; no oxidation pulse at Hotazel time.	no (criterion- and input-dependent)	sulfur isotope state and redox proxies in dated open-marine beds of that age: the anomaly persists under the O_2 criterion (Pavlov and Kasting, 2002), is lost under the CH_4 criterion (Zahnle et al., 2006); detrital uraninite bound 1.53×10^{-4} PAL (Johnson et al., 2014); Hotazel Mn with a negative Ce anomaly read as oxygenation (Gumsley et al., 2017)	uraninite bound met (Mississagi); Hotazel reading **not met**; Mooidraai 'no MIF-S?' at 2394 ± 26 Ma not met
Air first passes 10^{-5} PAL at 2.353 Ga, 4 Myr into the second interval; interval medians rise 2.0×10^{-6}, 1.4×10^{-5}, 3.6×10^{-5} PAL.	no; the level moves with the isotope input and, tenfold, with the kerogen-oxidation closure (Supplementary Text S4)	proxies with thresholds around the sulfur isotope threshold in the three dated intervals; the Kaapvaal onset window closes at 2.368 Ga (Mooidraai young edge) or at 2434.8 Ma on Kola (Gumsley et al., 2017; Warke et al., 2020)	late by 15 Myr against Mooidraai and by 81 Myr against Kola under the O_2 criterion; inside the Kola window under the CH_4 criterion
No downward crossing of 10^{-5} PAL after 2.217 Ga; no ice between then and the Neoproterozoic.	yes up to 2.22 Ga (part of what fixes ν); schedule after	any anomaly-bearing interval or glacial deposit dated between 2.2 and 2.0 Ga	consistent with the reading of Kasting and Ji (2025)

Table S20: Model statements about chemistry and the later oxygen level, and the model's assumptions restated as measurements that could test them (the full form of the lower half of Table 2 of the main text; columns as in Table S19). The interglacial carbon dioxide prediction is untested, the carbonate baseline is met as a calibration, and the Lomagundi–Jatuli excursion is not predicted. The later oxygen level falls inside the paleosol weathering-barometer ranges and below the chromium ceiling and misses the paleosol floor, a comparison specified in advance; because the level is set by two prescribed schedules, these outcomes bear on the post-transition inputs rather than on the transition. A row marked assumption gives an input value at which the four glaciations exist; at the alternative value that was integrated they do not, and the entry in parentheses gives the number of glaciations at that value (Supplementary Text S4 gives the intervals). CO_2 in multiples of the pre-industrial level, CH_4 in ppmv. The assumption rows are on the following page.

model statement	follows from the count?	deciding measurement	outcome
Interglacial CO_2 falls from 253, 239, 221 times pre-industrial one Myr after each thaw to minima of 65, 59, 53 before the next glaciation (medians 86, 77, 65; minima 52–66 across the three-or-four interval).	no	dated interglacial paleosols of either barometer school between 2.43 and 2.24 Ga	untested; the two interior profiles computed here overlap the range, four of five central values below it (no outcome yet; Supplementary Text S8)
Each deglaciation leaves 238–281 times pre-industrial CO_2, drawn down about fourfold within the interval.	assumption-dependent (exit threshold at one end of its published bracket)	cap-carbonate, weathering-intensity or triple-oxygen-isotope barometry above each of the four diamictites; cap carbonates are reported above the basal Duitschland diamictite (Gumsley et al., 2017)	open
Archean CH_4 279 ppmv at 2.9–2.7 Ga, 4.4 ppmv at 2.46 Ga, below 0.026 ppmv after the transition (under the escape assumption of Section 2.2 of the main text; 558 and 8.8 ppmv in the methane-only case); methane-borne hydrogen escape ends with the methane collapse, before the first glaciation.	control (no rock measures CH_4)	photochemical models: within a factor of two of Kharecha et al. (2005) at the same hydrogen input; xenon isotopes still evolving in the late Archean and modern by the mid-Paleoproterozoic (Avice et al., 2018), escape requiring a hydrogen-rich upper atmosphere (Zahnle et al., 2019)	ordering consistent; the model's total hydrogen, $f_T = 1.1 \times 10^{-3}$, is below the one percent Zahnle et al. (2019) require (Supplementary Text S1)
Carbonate $\delta^{13}C$ -1.0 to -0.3 per mil before the first glaciation; step across the transition $+0.29$ per mil.	calibration before the transition; not predicted after	compiled carbonate record: baseline within ± 2 per mil before 2445 Ma, Lomagundi–Jatuli peak $+7.9$ per mil (Edmonsond and Dyer, 2026)	baseline met (calibration); Lomagundi–Jatuli excursion **not predicted**
Later O_2 6.3×10^{-5} (2.2 Ga) to 6.0×10^{-4} PAL (1.4 Ga).	no; set by the two prescribed post-transition schedules (no redox feedback)	paleosol floor ≥ 0.14 PAL at 2.2–2.0 Ga (Rye and Holland, 1998); paleosol weathering barometer at 2.15, 2.08, 1.85 Ga (Kanzaki and Murakami, 2016); chromium ceiling $< 10^{-3}$ PAL, 1.8–0.85 Ga (Planavsky et al., 2014b)	floor **missed** by a factor 800 (specified in advance; failed); barometer met; ceiling met
Implied Marinoan duration 5.1 Myr; implied Sturtian 5.3 Myr.	one check of the sub-ice carbon rule; Sturtian not predicted	Marinoan 4–15 Myr, Sturtian 57–59 Myr (Hoffman et al., 2017)	Marinoan met; Sturtian **not reproduced**

Table S20: (continued) The model's assumptions restated as measurements that could test them; columns as on the previous page.

model statement	follows from the count?	deciding measurement	outcome
Nitrogen near one bar through the transition (at half a bar: five glaciations before 2.22 Ga and ten after it).	assumption	N_2 barometry through the transition; vesicle barometry on late-Archean lavas gives at most about 0.5 bar (Som et al., 2016)	open at the transition; against the model if the late-Archean value held to the first glaciation
Emergence complete by 2.45 Ga (earlier completion keeps the four glaciations; completion later than 2.38 Ga removes them; with the 2.50–2.20 Ga span of Bindeman et al., 2018 the count occurs at no exponent).	prescribed on the first glaciation	emergence chronologies (Kump and Barley, 2007; Bindeman et al., 2018)	open
Snowball entry threshold 10.1 $\mathrm{W\,m^{-2}}$ (at 15.8: no Paleoproterozoic glaciation at all at $\nu = 0.715$, at most two glaciations at any ν).	assumption	a general circulation model at Paleoproterozoic insolation and boundary conditions (Voigt et al., 2011; Feulner et al., 2023)	open
Sub-ice O_2 and CH_4 consumed below the ice (venting at most 3 percent); outgassed carbon taken into an exchangeable store, returned at the thaw and partitioned at the modern β_w.	assumption	sub-glacial redox and carbon archives; carbon-cycle models of the snowball ocean (Le Hir et al., 2008b; Hoffman et al., 2017)	open; crustal storage (Le Hir et al., 2008b,a) gives interglacials of 31.5–51.4 Myr across its four-glaciation interval, and their length further assumes that the returned carbon stays exchangeable at the modern partition (Table S5c–e; Section S1.9)
Modern O_2 1.000, CO_2 1.001, organic burial 10.0, silicate weathering 5.73 $\mathrm{Tmol\,C\,yr^{-1}}$; kerogen oxidation 8.19, volcanic reductant 1.82 $\mathrm{Tmol\,yr^{-1}}$.	identities, except the volcanic reductant sink, which follows from two published inputs and was not set to its estimate	Holland (2002): 7.5 ± 2.5 and 2.4 ± 1.8 $\mathrm{Tmol\,yr^{-1}}$	within uncertainty ($+0.27$, -0.32 σ); identities carry no test

S4 Sensitivity to the outgassing exponent and to the assumptions

We integrate the model across the whole published range of the outgassing-decline exponent ν (Section S4.1) and vary its assumptions one at a time (Section S4.2) and jointly (Section S4.3). The model's two prescribed Paleoproterozoic dates are the crossing epoch, at which the oxygen source first exceeds the oxygen-independent sinks, and the date at which continental emergence is complete. We then examine where the crossing epoch falls relative to the first glaciation (Section S4.4) and how the glacial era depends on the emergence date (Section S4.5). All of these integrations were made after the comparison of Supplementary Text S3 (Section S3.6) and outside it, and none of them changes an outcome of that comparison (Section S3.7); their numbers are exploratory in that sense wherever they appear.

S4.1 The sweep over the exponent

We integrated the model at 90 values of ν across the published range $[0, 1.46]$ of Krissansen-Totton et al. (2018), with the other inputs at their values in Table 1 of the main text. The grid in ν was refined wherever the number of glaciations changes, so that the value of ν at each change (an edge) is bracketed to ± 0.0025 or better (Fig. 6 of the main text; Fig. S3). Because the outgassing law is tied to the modern flux, a larger ν means more volcanic carbon dioxide and a warmer Paleoproterozoic, and we find that the number of glaciations falls in steps as ν rises. At $\nu \leq 0.05$ the integration stops when oxygen reaches the model's floor value, and no glaciation count is obtained. Below $\nu \simeq 0.55$ the model gives an icehouse of thirteen to sixteen glaciations, up to eleven of them after 2.22 Ga, and its air does not pass 10^{-5} of the present oxygen level (PAL) before 0.75 Ga. As ν rises the later glaciations disappear one at a time, but at every value below 0.7075 a glaciation still begins after 2.22 Ga, later than any dated Paleoproterozoic diamictite (at 0.705 the fifth begins at 2.174 Ga). Five glaciations beginning by 2.22 Ga occur only for $\nu \leq 0.6425$, and then together with at least three later ones, so that at these inputs no value of ν gives more than four Paleoproterozoic glaciations without later ice. The four-glaciation interval given next is therefore the same whether the glacial record is taken to show exactly four Paleoproterozoic glaciations or at least four. Just below it, for $0.6925 < \nu < 0.7075$, four glaciations begin by 2.22 Ga and one after, with the fifth at 2.19–2.15 Ga and the last thaw at 2.15–2.17 Ga.

For ν above 0.7975 (above 0.839 in the methane-only case, in which all escaping hydrogen is carried by methane; Supplementary Text S1, Section S1.3) there is no glaciation at all, and oxygen rises once and permanently at 2.38–2.43 Ga. The values of ν giving this single smooth rise make up 45% of the published range (43% in the methane-only case), and the Makganyene glaciation alone excludes them. Four glaciations beginning by 2.22 Ga and none after occur for $0.7075 < \nu < 0.7225$, 1.0% of the range. Three remain up to 0.7388, two up to 0.7475 and one up to 0.7975 (0.839 in the methane-only case). The wider interval $0.7075 < \nu < 0.7388$ (2.1% of the range), which we call the three-or-four interval, also includes the values of ν that give three glaciations, the number implied by the older correlation of the Transvaal and Huronian deposits. Every range given for the "allowed interval" in the main text is taken over this three-or-four interval. We found the same four-glaciation interval with the stepping procedure of Section S3.6.

We compared the four-glaciation and three-or-four intervals with the prior from which Krissansen-Totton et al. (2018) sample ν, to show where in that prior the value of ν fixed by the glacial record lies and what fraction of the prior mass falls within the three-or-four interval, whose width is the precision of that determination. Those authors draw a heat-flow exponent n uniformly from zero to 0.73 and a power m uniformly from 1 to 2, so that $\nu = nm$ has a product-of-uniforms density, flat up to $\nu = 0.73$ and falling to zero at 1.46. Its median is 0.53 and its central ninety-five percent range 0.03–1.24, and 68% of its mass lies below the principal value $\nu = 0.715$. Under a flat prior the four-glaciation interval holds 1.0% of the mass, the three-or-four interval 2.1% and the no-glaciation range 45%, and under the product-of-uniforms prior the three fractions are 1.4%, 3.0% and 25%. Under either prior the four-glaciation and three-or-four intervals hold one to three percent of the prior mass, and their positions depend on the assumptions (Section S4.3).

At the exponent fixed by the glacial record, the glacial dates and oxygen levels that do not follow from the number of glaciations can be tested against the rock record. The eight integrations at values of ν inside the three-or-four interval show how much each of these quantities varies with the position of ν in that interval (Fig. 6b of the main text and Fig. S3). The first glaciation, whose onset is set by the prescribed emergence date, is insensitive to ν within the interval: it begins at 2.4491–2.4513 Ga and ends at 2.4240–2.4254 Ga, a spread of 2.3 Myr, always contains the Ongeluk age and lasts 25.1–25.9 Myr. Air first passes 10^{-5} PAL at 2.348–2.355 Ga, at or soon after the second thaw at every value of ν and never before it. Therefore, throughout the three-or-four interval, the first interglacial is anoxic and oxic air first appears after the younger limit of the Kaapvaal window for the first oxygenated air (Supplementary Text S3).

The dates of the later glaciations vary more across the three-or-four interval than those of the first. The third glaciation ends at 2.266–2.292 Ga, a spread of 26 Myr, and is 18 to 44 Myr later than the Gordon Lake

Table S21: The model's glacial chronology at $\nu = 0.715$, the midpoint of the four-glaciation interval. The four glaciations last about 25 Myr each, begin at 66.6–52.6 times pre-industrial carbon dioxide and end at 238–281, and are separated by interglacials of 43.4–48.8 Myr whose oxygen maxima increase from one to the next; ranges over the four-glaciation interval are in the text. Carbon dioxide in multiples of its pre-industrial pressure, oxygen as a fraction of the present level, interglacial values on the one-Myr output grid. The number of glaciations and the absence of any later one fix the exponent, so the date of the last thaw and the spacings follow from that number and are not offered as support for the model. Under the ice the air holds no oxygen or methane, by the sub-ice assumption of Section 2.3 of the main text.

glaciation	begins (Ga)	ends (Ga)	lasts (Myr)	CO_2 at entry	CO_2 at exit
first	2.4509	2.4251	25.7	66.6	281
second	2.3818	2.3571	24.6	65.1	266
third	2.3134	2.2893	24.1	59.1	252
fourth	2.2405	2.2169	23.6	52.6	238
interglacial	span (Ga)	lasts (Myr)	O_2 max (PAL)	CO_2 at thaw + 1 Myr	CO_2 median
first	2.4251–2.3818	43.4	4.8×10^{-6}	253	86
second	2.3571–2.3134	43.7	2.0×10^{-5}	239	77
third	2.2893–2.2405	48.8	4.5×10^{-5}	221	65

bound allows at every value; the largest discrepancy of Section 4.2 of the main text therefore persists under any choice of ν within the interval. The last thaw, which is the permanence date and follows from the number of glaciations, moves from 2.209 to 2.283 Ga across the interval, a spread of 74 Myr, because in the upper part of the interval there are three glaciations and the last thaw is then the third. Glacial durations stay at 23.5–25.9 Myr and interglacial durations at 42–58 Myr, the interglacial carbon dioxide minima lie between 52 and 66 times pre-industrial, and the Marinoan computed with the same sub-ice rule lasts 5.13–5.15 Myr, within its dated range throughout. Table S21 gives the glacial chronology at the principal value, and Fig. 3 of the main text compares it with the dated beds.

S4.2 Sensitivity to single assumptions

The four-glaciation interval exists only for some values of the inputs that enter the model as assumptions (Table 1 of the main text), and we first varied each of these inputs alone. In the comparison of Supplementary Text S3 each assumption was changed to a published alternative with ν held at 0.715 (Fig. S4), and for seven of them we repeated the sweep of Section S4.1 with the one input changed (Fig. S5). In the alternative families of Section S3.6 (the model with one input or one functional form changed), ν was fixed again by the glaciation count (Fig. S6). A change in the number of glaciations at one value of ν means either that the exponent the glacial record fixes has moved or that no interval exists under the changed input; we distinguish the two cases with the repeated sweeps and with the joint sampling of Section S4.3.

The number of glaciations is most sensitive to two of the climate inputs, the glaciation threshold D^* and the nitrogen inventory; at the alternative value of either, no ν in the published range gives the recorded glacial era. The glaciation threshold is held constant at $D^* = 10.1\ \mathrm{W\,m^{-2}}$, the lowest value a general circulation model has given for snowball entry (Voigt et al., 2011). At the $15.8\ \mathrm{W\,m^{-2}}$ that the intermediate-complexity model of Feulner et al. (2023) implies for Paleoproterozoic insolation, our model gives at most two glaciations anywhere in the published range of ν, and those only at $\nu \leq 0.10$. The radiative tables are read at 1 bar of nitrogen; at 0.5 bar no value of ν gives three or four glaciations with none after 2.22 Ga, because glaciations after 2.22 Ga persist up to $\nu \simeq 1.12$, and at that value only two glaciations remain before 2.22 Ga. With its other inputs at the values of the main text, the model thus reproduces the recorded glaciations at some ν only with about one bar of nitrogen and with the lowest published glaciation threshold. However, because the lower nitrogen inventory and the higher threshold of Feulner et al. (2023) displace the interval in opposite directions, combinations of inputs in which both are changed can still have an interval (Section S4.3).

Under the other single changes for which we repeated the sweep over ν, the glacial record fixes ν again, to an interval 0.02–0.04 wide at a displaced value. At a weathering response temperature of 13.9 K instead of 11.1 K the three-or-four interval moves to 0.89–0.91, 0.17 above the interval at the main-text inputs, which is the largest shift we found. For the weathering response time τ_{sil}, which sets the ocean–atmosphere carbon partition (Supplementary Text S1), the main text uses the slow end of the range 170–380 kyr (Colbourn et al., 2015); at its central value, 240 kyr, the interval moves to 0.74–0.76. Modern outgassing at either end of its prior displaces the interval by about 0.02. At a deglaciation level of 0.028 bar instead of the low end, 0.01 bar, of the Cryogenian range (Hoffman et al., 2017; Abbot et al., 2012), three glaciations with none after occur for 0.70–0.72, and no value of ν gives four. The four glaciations also hold for sub-ice venting fractions

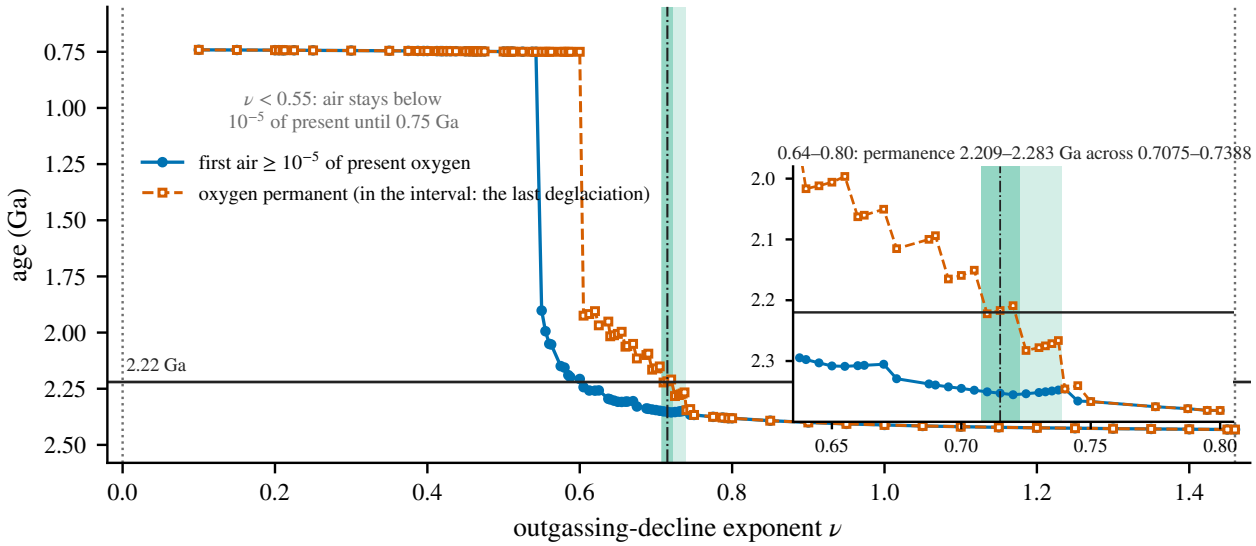

Figure S3: Date at which air first exceeds 10^{-5} of the present oxygen level (filled) and date from which oxygen stays above it (open), against the outgassing-decline exponent ν, from the same 90 integrations as Fig. 6 of the main text; dark and light shading, the four-glaciation and three-or-four intervals; dash-dotted, the principal value 0.715. Across the interval the glacial record allows, the date of first oxic air, which the rock record tests, changes little, whereas the permanence date, which follows from the number of glaciations, moves by 74 Myr. Inside that interval oxygen becomes permanent at the last thaw, 2.209–2.283 Ga (inset), and the date of first oxic air lies at 2.348–2.355 Ga. Below $\nu \simeq 0.55$ the air stays under the threshold until 0.75 Ga, and above 0.7975 (0.839 in the methane-only case of Supplementary Text S1) the two dates coincide in the single smooth rise. Exploratory integrations.

up to 0.03 (Supplementary Text S1), and the emergence date is treated separately in Section S4.5.

The burial inputs and the crossing epoch move the interval by less than its width, and they do not remove it in any of our integrations. The number of glaciations at $\nu = 0.715$ changes by at most one when the late-Archean burial fraction is shifted by one standard error or the epoch at which it is applied is moved, and when the carbon-isotope input is varied across its ±1 per mil band or the crossing epoch across the onset window. Where we fixed ν again, ν moved by one or two grid steps (Fig. S6). The interglacial in which oxic air first appears changes with the isotope input (Table S16). Two inputs affect the later oxygen level and leave the glaciations unchanged. A lower productivity schedule after the transition (0.2 of modern) keeps the mid-Proterozoic anoxic, with permanent oxygen only from 0.74 Ga. If kerogen oxidation stops increasing with oxygen above 0.1 PAL (a ceiling on its $O^{1/2}$ law; Supplementary Text S2), the oxygen of every interglacial falls to a tenth of its value in the principal integration, and air first passes 10^{-5} PAL only at 2.126 Ga. The four glaciations are unaltered when we rescale or remove the subaerial reductant step, set the Archean iron–phosphorus trap at either end of its published span, adopt an in-ocean methanotrophy rule, vary the seafloor-weathering heat-flow exponent or add an enhanced Lomagundi burial.

For the two choices of functional form in Section 2 of the main text, the post-crossing sink law and the sub-ice carbon rule, we integrated each alternative as a family in which ν was fixed again by the glaciation count. The three alternatives to the isotope-inferred post-crossing sink each have a four-glaciation exponent (0.9725, 0.96 and 0.8425), and all three fail the carbonate-isotope criterion by which we chose the isotope-inferred law (Supplementary Text S1). The alternative sub-ice rule, in which a fixed fraction of the sub-ice outgassing accumulates in the air, lengthens the glaciations at the main-text inputs to 41–44 Myr (Supplementary Text S1). Under it we found no four-glaciation exponent with the isotope-inferred sink in the search started from 0.715 (three glaciations, never four) and one only with the nickel-proxy sink, at 0.955, with glaciations of 36–39 Myr.

The sub-ice partition enters the sub-ice carbon rule together with the deglaciation level, and the dated Cryogenian glaciations constrain the two only in combination, since at each deglaciation level there is a band of partitions for which the model's Marinoan glaciation has the dated length (Supplementary Text S1). Within the family of deglaciation levels and partitions so defined, four Paleoproterozoic glaciations with none after 2.22 Ga occur at three of the four combinations that we integrated, each at an exponent fixed again by the glaciation count. The three are the highest deglaciation level with the sub-ice uptake of Le Hir et al. (2008a) as the partition (glaciations of 22.6–23.4 Myr, last thaw 2.2265 Ga), the lowest deglaciation level with the partition that gives the shortest dated Marinoan ($\nu = 0.72$, glaciations of 18.5–20.0 Myr), and the highest deglaciation level with the partition computed from carbonate-saturated seawater chemistry ($\nu = 0.7325$, glaciations of 10 Myr, last thaw 2.283 Ga). With that calcite-saturation partition the third

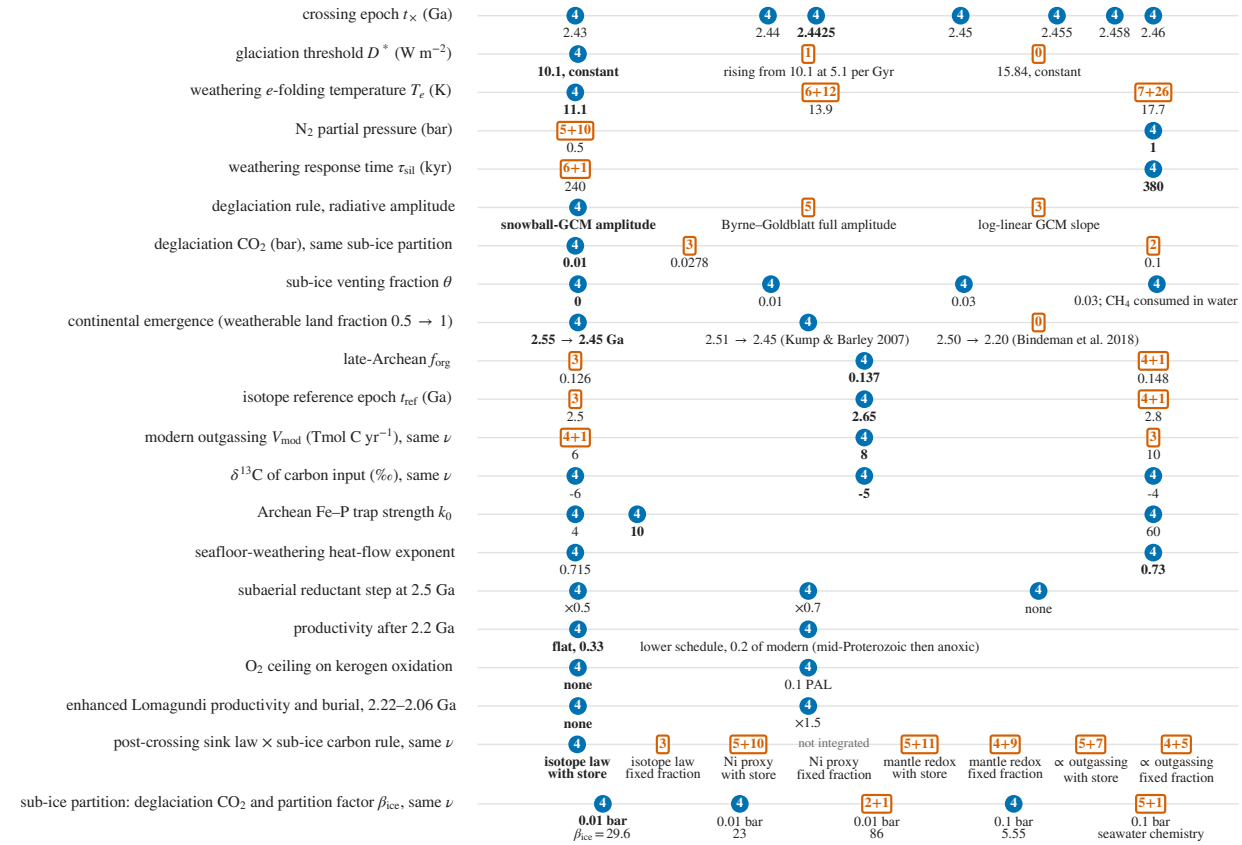

Figure S4: Number of glaciations with one input changed at a time and ν held at 0.715 (comparison of Section S3.6). Each glyph: glaciations beginning by 2.22 Ga, plus any beginning later; filled circles, four and none later; boxed numbers, four not obtained; bold values, those of the main text. A boxed number means that the exponent the glacial record fixes has moved or that no interval exists under the changed input (Fig. S5 and Section S4.3 distinguish the two). At this exponent four glaciations are lost under half a bar of nitrogen, the higher glaciation threshold, a weaker weathering response or a shorter response time, a higher deglaciation level, later emergence and the alternative sink laws, and kept under every other change.

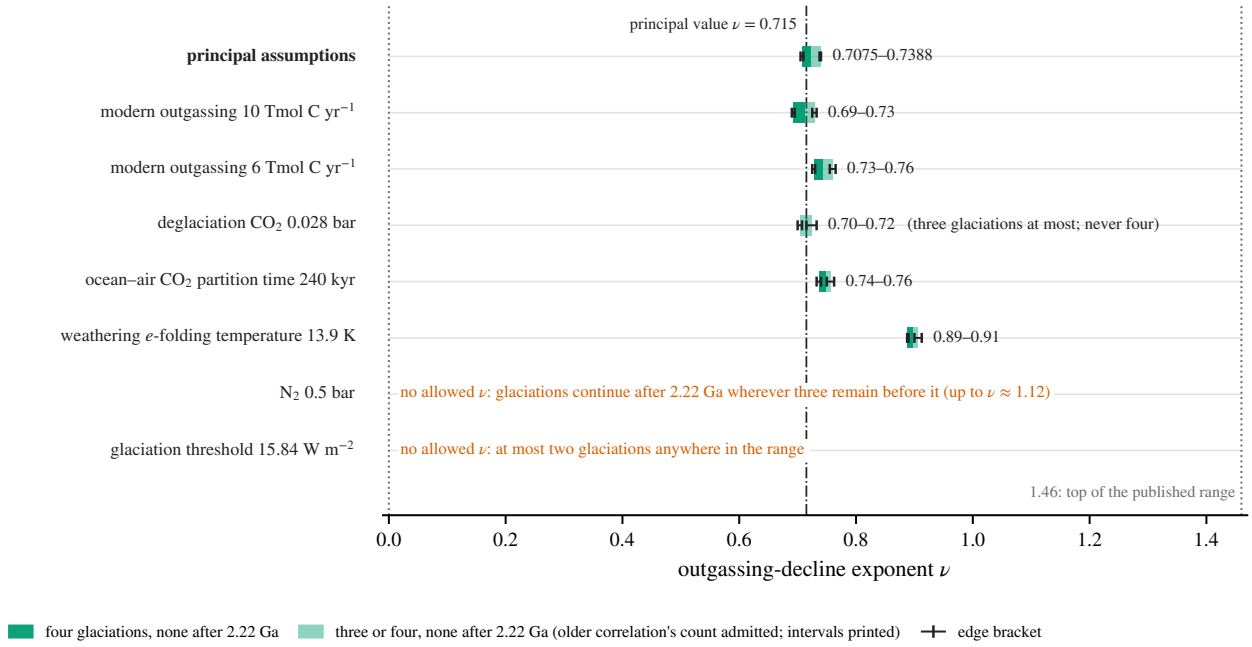

Figure S5: The sweep of Fig. 6 of the main text repeated with one input changed, on a coarser grid, refined near each edge until the edge is located to within the uncertainty drawn as caps. Dark bars, the values of ν giving four glaciations by 2.22 Ga and none after; light bars, three or four, for which the intervals are printed; dash-dotted, the principal value 0.715. Under modern outgassing at either end of its prior, the higher deglaciation level, the central weathering response time or the weaker temperature dependence of weathering, the interval is 0.02–0.04 wide and displaced by about 0.02 (by 0.17 for the weathering temperature); at the higher deglaciation level there are three glaciations and never four. With half a bar of nitrogen (Som et al., 2016) or the glaciation threshold of Feulner et al. (2023) no value of ν gives a Paleoproterozoic glacial era of the recorded kind. Exploratory integrations.

glaciation ends at 2.338 Ga, inside the Gordon Lake bound that the principal integration misses. The first glaciation then no longer contains the Ongeluk age, however, and the upper Timeball Hill bound and the Hekpoort bound on the last deglaciation are missed instead, so no integration in any family meets the four bounds together. At the lowest deglaciation level with the partition that gives the longest dated Marinoan, we found no four-glaciation exponent in the search from 0.715.

We infer that the model's glacial chronology depends on the amount of carbon stored per glaciation and on its return at the thaw. The glacial durations are uncertain by a factor of about 1.3 across the combinations that keep an exchangeable store (18.5–25.9 Myr) and by about 2.5 when the combination with the calcite-saturation partition is included. A dated glacial termination therefore tests the sub-ice uptake within that factor, and a dated spacing, which follows from the number of glaciations once the sub-ice rule is fixed, tests whether the stored carbon returns. The composition of the sub-ice store is not specified in the model (Supplementary Text S1). If the carbon went into altered ocean crust, as in the sub-ice carbon-cycle model of Le Hir et al. (2008b,a), only the airborne excess would return at the thaw. In our integrations of that crustal-carrier case, four glaciations with none later occur for $\nu = 0.719$–0.732 rather than the 0.7075–0.7225 of the exchangeable store, with interglacials of 31.5–51.4 Myr over that higher interval (Supplementary Text S1). At its midpoint the interglacials last 33.0–38.9 Myr, shorter than with the exchangeable store, so that the third glaciation ends inside the Gordon Lake bound but the fourth begins before the upper Timeball Hill tuffs allow. The spacing of the glaciations lengthens toward the upper edge of that interval, and the integration near that edge, at $\nu = 0.73125$, meets the Ongeluk, upper Timeball Hill and Hekpoort bounds together, as well as the open interval that the Timeball Hill shale requires before the fourth glaciation, and misses the Gordon Lake bound by 2.0 Myr (Table 3 of the main text). In these crustal-carrier integrations the carbon returned at a thaw is divided between air and ocean instantaneously. When that division is instead spread over even a few hundred thousand years, the integration near the upper edge no longer meets the upper Timeball Hill and open-interval bounds, although its third glaciation then ends inside the Gordon Lake bound (Supplementary Text S1).

S4.3 Joint sensitivity to the assumptions

A single change at one value of ν cannot distinguish an assumption that removes the glacial era from one that moves the exponent the glacial record fixes, so at D. T. Johnston's request we examined each assumption

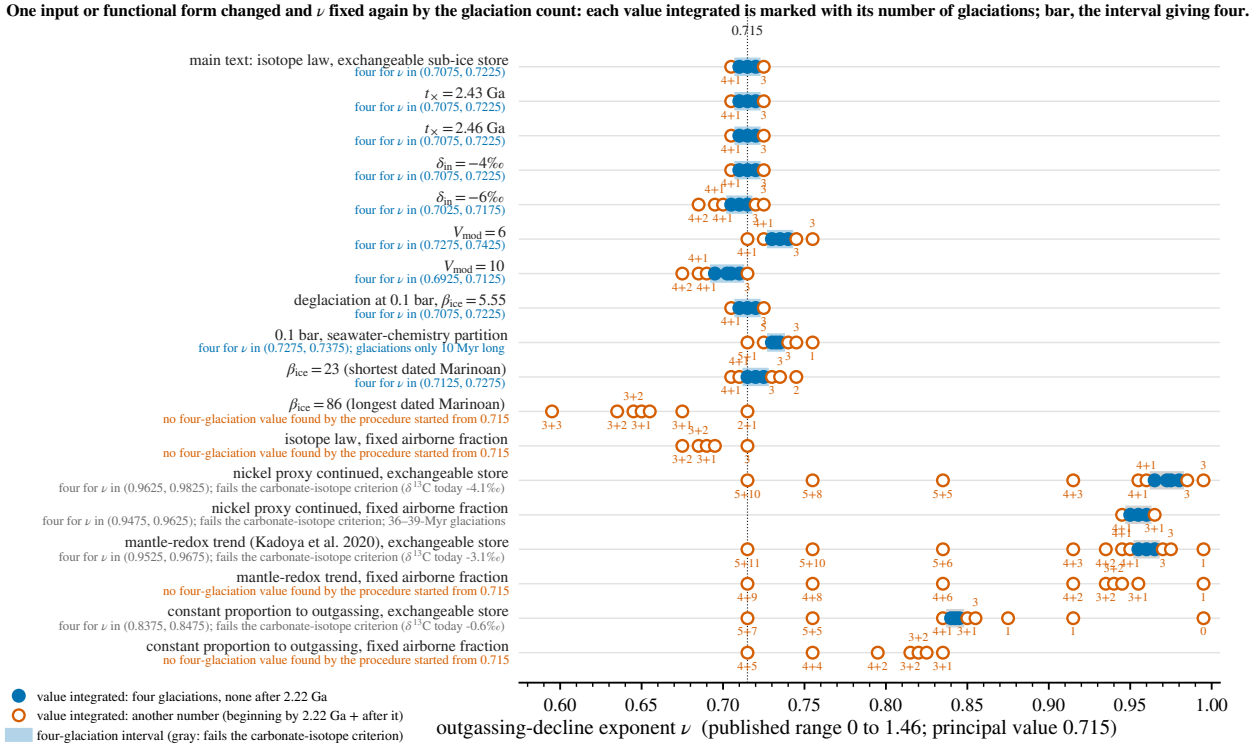

Figure S6: The exponent fixed again by the glaciation count when one input or functional form is changed (procedure of Section S3.6). Each value of ν integrated carries its number of glaciations (filled, four by 2.22 Ga and none later; open, any other number); bars, the interval giving four, gray where the family fails the carbonate-isotope criterion. The exponent moves by less than the interval's width when the crossing epoch or the isotope input is changed, and by about 0.02 for modern outgassing at either end of its prior. Under the fixed-fraction sub-ice rule the procedure, started from 0.715, finds no four-glaciation value with the isotope law or with two of the three alternative sink laws, which does not show that none exists.

over its published range and then all of them jointly. Eight inputs were treated as axes, each varied over its published range in Table S22 (the deglaciation level X is paired with the sub-ice partition, parametrized by its position in the band of partitions that give a Marinoan of the dated length at that level). Along each axis, with the other seven at the values of the main text, we searched ν over $[0.10, 1.46]$ for an interval giving three or four glaciations by 2.22 Ga and none after, and bracketed the value of the input at which that interval disappears. To vary the assumptions jointly we drew Latin-hypercube samples over these ranges under two sampling schemes, $N = 400$ per scheme. The venting fraction, which we varied only singly, is held at zero in these samples, and the deglaciation level and the sub-ice partition are sampled as separate dimensions, eight in all. The open-water partition β_w, on which the interglacial length also depends (Supplementary Text S1, Section S1.9), has no published Paleoproterozoic range and is held at its modern value in every sample. Scheme A samples all eight uniformly over their ranges (X log-uniformly), and scheme C holds the threshold at 10.1 $\mathrm{W\,m^{-2}}$ and the nitrogen at 1 bar and samples the other six. A sample survives if the same search finds some ν giving three or four glaciations by 2.22 Ga and none after; we record "four" only where the search also produced an integration with four rather than three, which makes the four-glaciation fractions lower bounds. We give binomial (Wilson) ninety-five percent intervals on the fractions. In the joint sampling 219 integrations stopped on the model's oxygen floor at low ν and gave no glaciation count, as in the sweep over ν.

Taken one at a time, six of the eight assumptions have an edge inside or at the end of their published range beyond which no scanned value of ν gives the recorded glacial era, and two, the weathering response time and the modern outgassing, do not (Table S22; Fig. S7). The glaciation-threshold edge lies at 14.715 ± 0.045 $\mathrm{W\,m^{-2}}$, above which the interval passes below the scan floor $\nu = 0.10$ (reproducing the glaciations would then require a nearly constant outgassing history). The nitrogen edge lies at 0.5675 ± 0.0075 bar (with the forcing interpolated between the half-bar and one-bar tables), the weathering-response edges lie at 6.6 and 19.6 K, and the emergence edge lies at completion by 2.380 ± 0.005 Ga (completion at any earlier date keeps the glacial era). The recorded glacial era is kept for sub-ice venting fractions up to a tenth, and for every integrated combination of deglaciation level and sub-ice partition except the lowest level with the longest-Marinoan partition. Along these input ranges the exponent the glacial record fixes, written ν^* in Tables S22 and S23, moves from 0.10 to 1.10, toward lower ν as the threshold rises and toward higher ν as the nitrogen falls or the weathering response weakens.

Under joint sampling with scheme A, some ν gives three or four glaciations and none after 2.22 Ga in a fraction 0.45 of the samples (ninety-five percent interval 0.40–0.50) and four (rather than three) in at least 0.28. Under scheme C, with the threshold and the nitrogen held at the values used, the two fractions are 0.64 and 0.54 (Table S23). In the scheme-A samples that fail, the glacial era is most often lost through a steep weathering response ($T_e < 6.6$ K, which moves the interval below the scan floor; only 2 of 64 such samples keep an interval) or through emergence completed later than 2.38 Ga (3 of 103). Among the samples with neither a steep weathering response nor late emergence, the surviving fraction is 0.71 under scheme A and 0.97 under scheme C. We find that the two assumptions that individually exclude the glacial era, the higher threshold and the lower nitrogen, displace the interval in opposite directions and compensate, and 11 of 21 scheme-A samples with a threshold above 14.7 $\mathrm{W\,m^{-2}}$ and less than 0.6 bar of nitrogen still have an interval. Multiplying the one-at-a-time surviving fractions over the published alternatives would give only 0.07, because that product treats the inputs as independent and so misses the compensation between the threshold and the nitrogen. At $\nu = 0.715$ held fixed the recorded number of glaciations occurs in only 3.5% of the scheme-A samples (2.1%–5.8%). This fraction is small because ν is itself fixed by the glaciation count: each setting of the assumptions admits the recorded glaciations only in a narrow interval of ν, and the position of that interval differs from one setting to another.

Across the surviving samples ν^* has median 0.64 and central ninety percent range 0.22–0.98 under scheme A (0.71 and 0.20–0.94 under scheme C), while the median half-width of a single sample's interval is 0.015 (Fig. S8). These numbers suggest that at any one setting of the assumptions the glacial record fixes ν to about ± 0.015, and that varying the assumptions within their ranges moves that value over most of the published range of ν. The principal value 0.715 and its precision are therefore specific to the inputs of Table 1 of the main text. For this reason we treat the glaciation threshold, the nitrogen inventory, the weathering response and the emergence date in Section 4.5 and Table 2 of the main text as quantities that the glacial record and the model constrain jointly. We also compared the distribution of ν^* over the surviving samples with the published outgassing histories converted to this exponent at 2.45 Ga (our conversion; Supplementary Text S2). The central range of ν^* covers the cluster at 0.70–0.79 in which outgassing follows a conventionally declining heat flow, the form that Claire et al. (2006) adopted and on which the law of Krissansen-Totton et al. (2018) is also built, and the values near 1.03–1.06 at which mantle carbon input follows spreading-center heat flow (Hayes and Waldbauer, 2006). The central range does not reach the plate-scaling conversions at 1.16 and above or the xenon-based degassing levels near 2.90–2.93, and none of the individual conversions falls inside the four-glaciation interval of the main text.

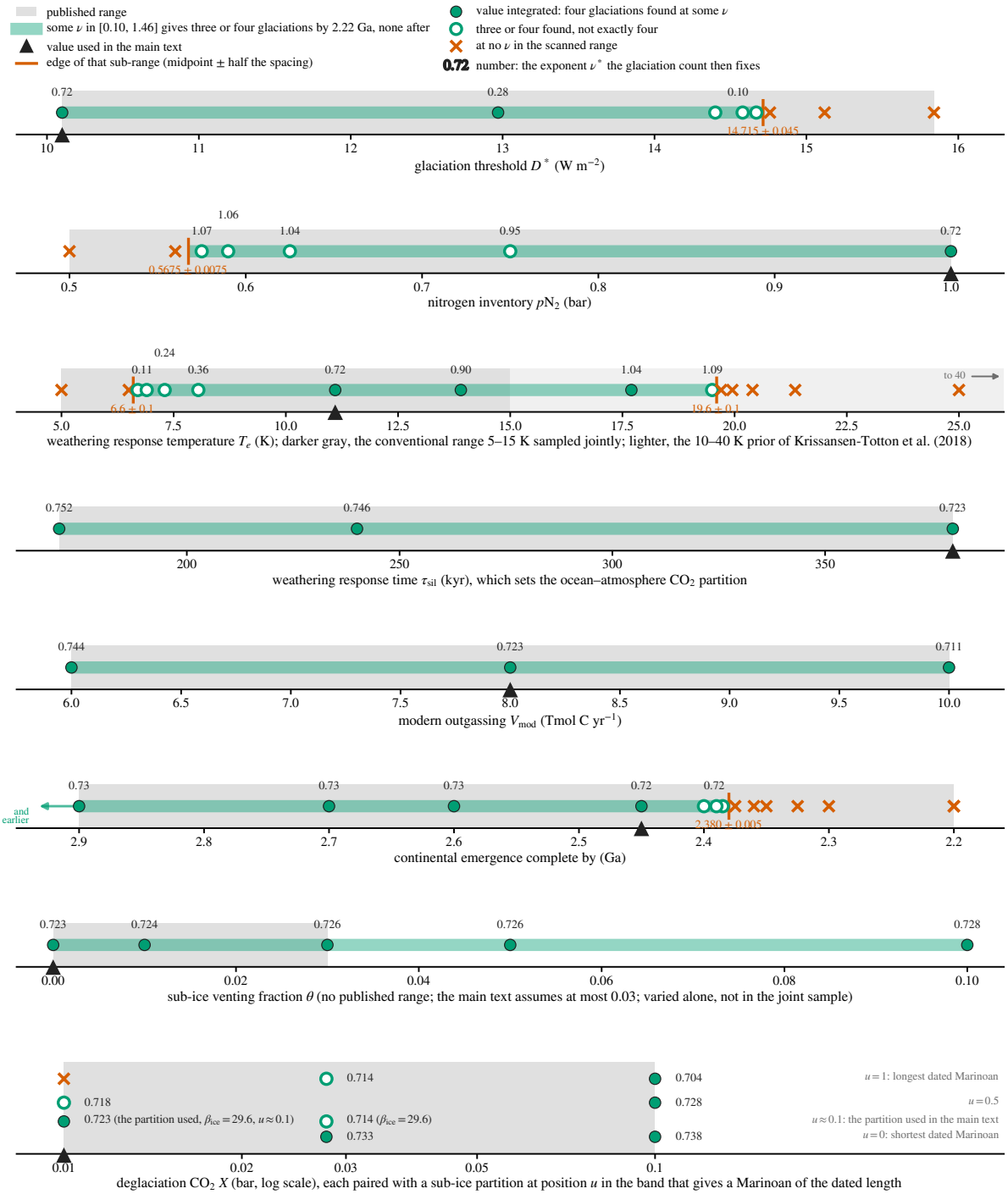

Figure S7: Values of each assumed input at which some exponent ν in $[0.10, 1.46]$ gives three or four glaciations by 2.22 Ga and none later, with the exponent ν^* that the glaciation count then fixes printed at each value. Filled circles, four (not three) found at some ν; open, three or four only; crosses, no such exponent; gray, the published range; triangles, the values of the main text; vermilion, the edges of Table S22 (threshold 14.715 ± 0.045 W m^{-2}, nitrogen 0.5675 ± 0.0075 bar, weathering response 6.6 and 19.6 K, emergence 2.380 ± 0.005 Ga). Along these axes ν^* runs from 0.10 to 1.10, far wider than the interval at any one setting. Fig. 7a of the main text shows the same integrations. Exploratory integrations.

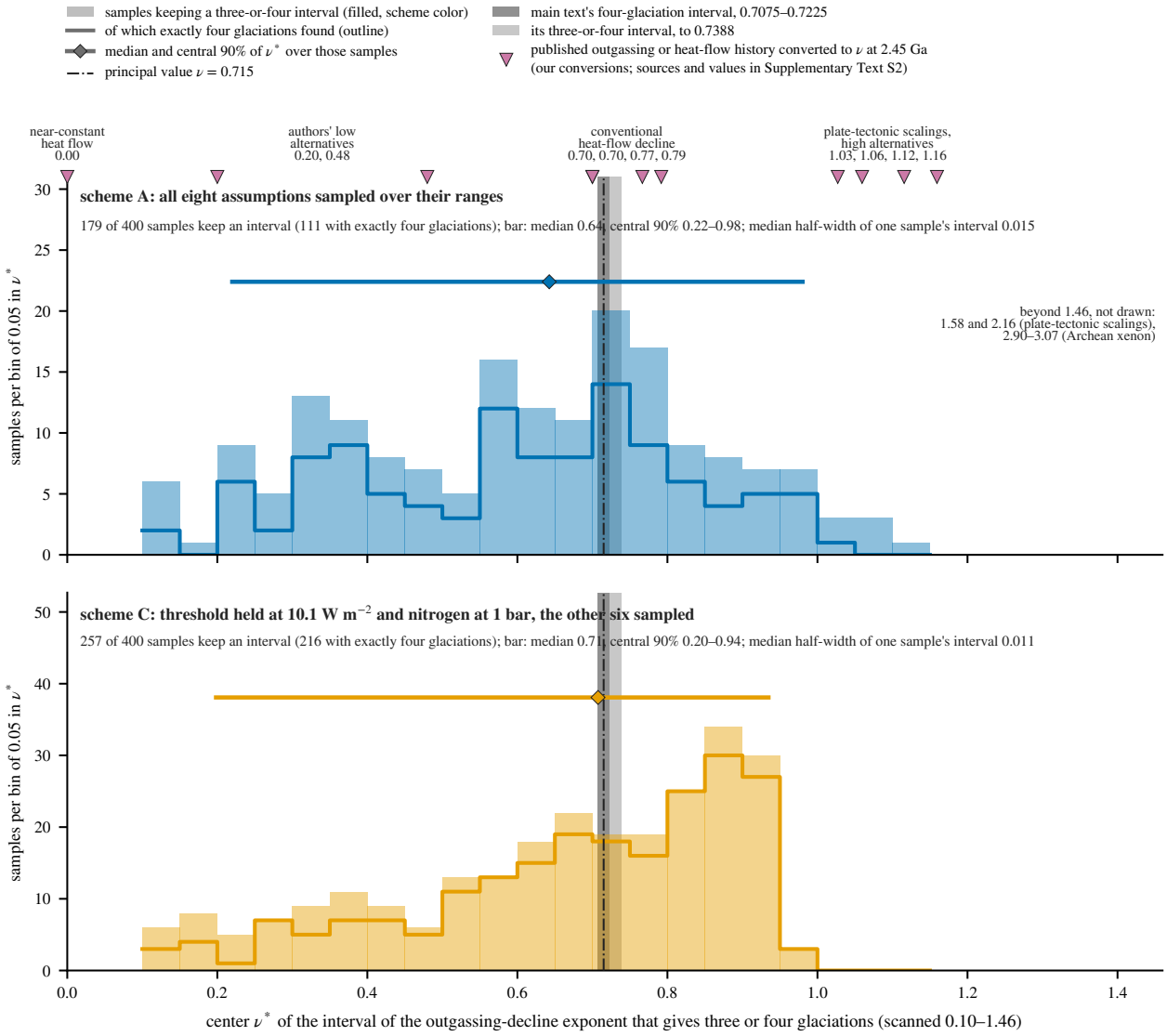

Figure S8: Histograms of the center ν^* of the three-or-four interval over the Latin-hypercube samples that keep one: upper panel, scheme A (179 of 400; median 0.64, central ninety percent 0.22–0.98); lower panel, scheme C (0.71, 0.20–0.94). Heavy outlines, samples in which four (not three) were found; bars with diamonds, median and central ninety percent; gray bands, the main text's four-glaciation and three-or-four intervals; dash-dotted, 0.715. The centers spread over most of the published range, whereas one sample's interval is narrow (median half-width 0.015, scheme A). Triangles, published outgassing histories converted to ν at 2.45 Ga (our conversion; Supplementary Text S2), from near-constant heat flow (0.00) through the conventional decline (0.70–0.79) to plate-tectonic scalings (1.03–1.16); xenon-based levels (2.90–3.07) lie off scale. Exploratory integrations.

S4.4 The prescribed crossing epoch and the first glaciation

The epoch $t_\times$ at which the declining oxygen-independent sinks first equal the gross oxygen source is prescribed inside the dated onset window of the Great Oxidation, and it enters the model only through the methane amplitude G_A solved from it (equation 3 of the main text); the model computes no crossing epoch of its own. Over the 801 integrated trajectories we examined, stored phosphate equals its Archean value at every output time before $t_\times$, so the open-water budget balances at the prescribed epoch by construction. An earlier circulated draft described the prescribed crossing epoch, returned through the one-million-year output grid by a post-processing step, as a crossing epoch computed by the integration itself and falling under the ice; we had misinterpreted the output grid, and the two numbers given there are not used in this work. Because $t_\times$ is prescribed, the position of the crossing relative to the first glaciation depends on where in the onset window $t_\times$ is set, and we therefore give it as a distribution over that window and over ν.

We integrated the model on a grid over the onset window and the exponent, 27 values of $t_\times$ (21 inside the window 2.43–2.46 Ga, including a strip at one-Myr spacing where the position of the crossing relative to the first ice changes) crossed with ν across its published range, 553 integrations in all (Fig. S9; Table S24). We weight $t_\times$ flat on the window and ν either flat or by the product-of-uniforms prior of Section S4.1. With these weights, the model gives no glaciation over 45% of the prior mass on the $(\nu, t_\times)$ grid (25% with ν prior-weighted) and a glacial era running past 2.22 Ga over 46% (64%). Three or four glaciations with none later, the recorded glacial era, occur over only 2.1% (2.8%) of the prior mass. The four-glaciation interval in ν exists for all 21 values of $t_\times$ inside the window, its edges moving by at most one grid step (0.0025), and at the seven crossing epochs of Table S9 every glacial date stays within 9 Myr of its value in the main text. Conditional on three or four glaciations and none later, the prescribed crossing falls under the first glaciation for 84% of the prior mass and before it, in open water, for 16% (the same percentages, to the nearest integer, under either prior on ν). The crossing falls after a thaw at none of the points inside the window that are consistent with the rock record.

We interpret the two cases, a crossing under the first ice and a crossing before it in open water, as a consequence of the different dependence of the methane collapse and of the first glaciation on $t_\times$ and ν (Table S25). The methane collapse is set by $G_A(t_\times)$ and by the reductant and nickel schedules, and it depends only weakly on ν. Over the eight values of ν consistent with the rock record at $t_\times = 2.4425$ Ga, open-water methane falls below ten ppmv at 2.481–2.482 Ga, 30.5–31.9 Myr before the first ice under the escape assumption of Section 2.2 of the main text (about 12 Myr before it in the methane-only case of Supplementary Text S1). Across these values of ν the ten-ppmv date varies by 0.92 Myr and the first-ice date by 2.25 Myr. Both dates thus vary only weakly with ν; their separation is governed mainly by $t_\times$, because the methane collapse moves with $t_\times$ through G_A whereas the first glaciation, whose date is tied chiefly to the prescribed completion of emergence, moves less. At $\nu = 0.715$ the crossing is under the first ice for every value $t_\times \leq 2.456$ Ga and before it for every $t_\times \geq 2.457$ Ga, and that boundary moves 1.6 Myr younger per hundredth of increase in ν over the 22 values at which we bracketed it. In the first case, with the crossing under the first ice, the glacial entry is methane-assisted, in that it coincides with the final collapse of the 0.73–3.77 ppmv of methane still present, and the ice precedes the prescribed crossing by up to 15.0 Myr (8.4 Myr at $t_\times = 2.4425$ Ga). In the second case methane has already fallen below one ppmv in open water, and the glaciation, driven by the carbon dioxide decline alone, follows the crossing by 3.3–9.3 Myr. Across the onset window the date of the first glacial entry moves from 2.4450 to 2.4589 Ga, with four glaciations and none later at every value.

In every integration consistent with the rock record, whatever the position of the prescribed crossing, oxic air first appears only after the first glaciation, and this order, unlike the position of the crossing, is observable in the rocks. We examined 307 such integrations in all, 203 of them with the crossing epoch inside the onset window under the emergence history of the main text, and the rest with the crossing epoch outside the window, with the earlier emergence histories of Section S4.5, or with both varied together. In all of them surface oxygen stays below 6.1×10^{-6} PAL until the first glaciation (below 4.2×10^{-7} PAL over the values inside the window). Air first passes 10^{-5} PAL only after the first glaciation, in a later interglacial in 305 of them and within a fraction of a kiloyear of the second glacial entry in the other two. That interglacial is the first one in 49 of them, most with the crossing epoch older than the onset window or with emergence completed later than in the main text; among the 203 combinations inside the window under the emergence history of the main text it is the first in 16, all with three glaciations, $\nu \geq 0.7275$ and $t_\times \geq 2.454$ Ga, where oxygen reaches at most 1.3×10^{-5} PAL before the second glaciation. Oxygen becomes permanent at the last thaw, which over the values inside the window falls between 2.197 and 2.290 Ga. With emergence complete earlier than in the main text the prescribed crossing falls in the open water of the first interglacial instead (Section S4.5), and the observable order is the same.

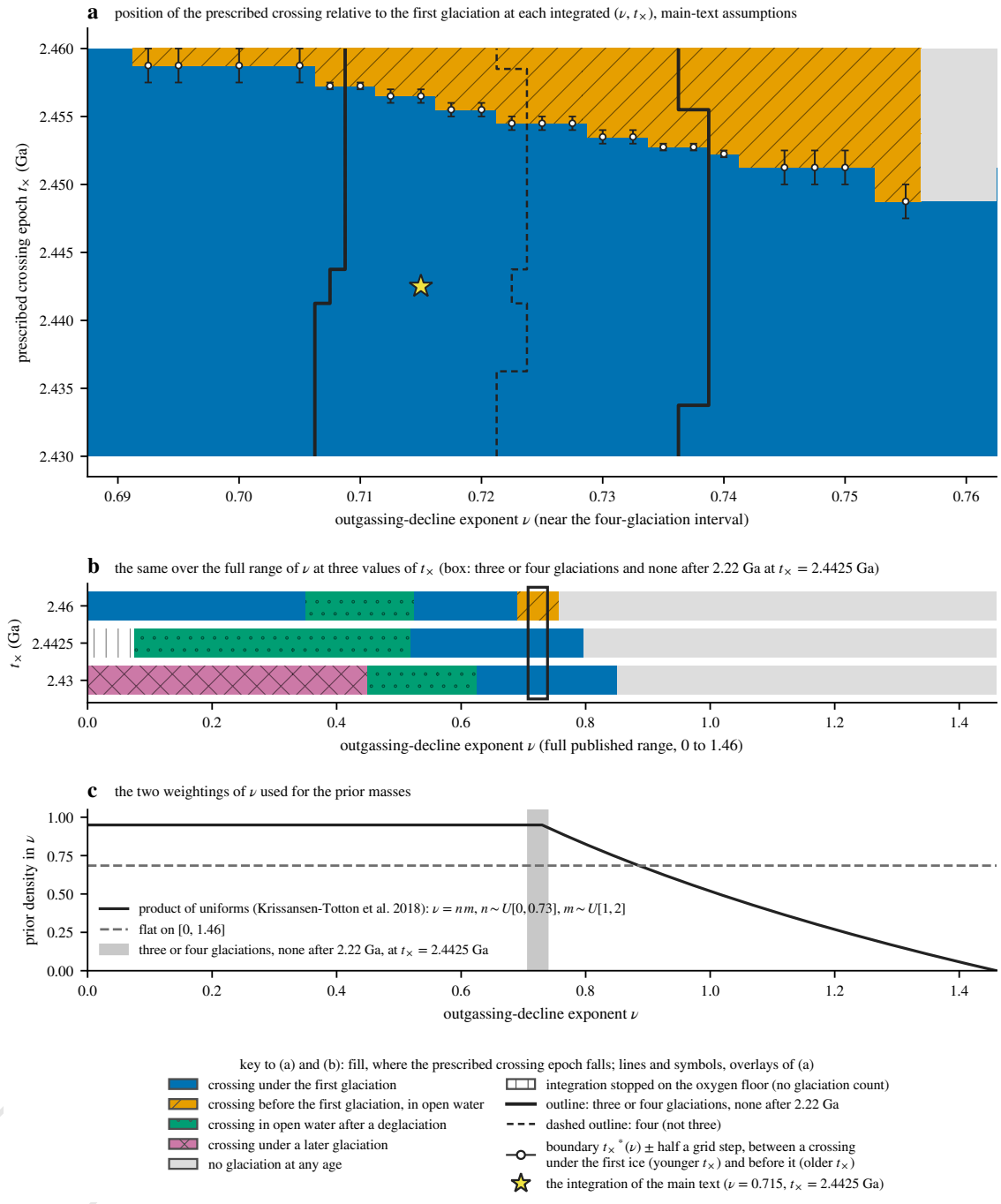

Figure S9: Position of the prescribed crossing epoch $t_\times$ relative to the first glaciation. (a) Fill, the position of the crossing at each integrated $(\nu, t_\times)$ under the main-text assumptions; outlines, three or four glaciations and none after 2.22 Ga (solid), four (dashed); open circles, the boundary between a crossing under the first ice (younger $t_\times$) and before it (older); star, the main text's integration. (b) The same over the full range of ν at three values of $t_\times$. (c) The two weightings of ν in Table S24. Given the recorded number of glaciations, the crossing is under the first ice for 84% of the prior mass and before it for 16%; since $t_\times$ is prescribed, these fractions are not model predictions. Exploratory integrations.

S4.5 The date of continental emergence

The completion of continental emergence is prescribed at the onset of Paleoproterozoic glaciation in the rock record and sets the date of the model's first glaciation (Section 2.1 of the main text). The sensitivity to this date is one-sided: earlier completion keeps the recorded glacial era and changes only the date of the first glaciation, whereas completion later than 2.38 Ga removes the glacial era at every exponent (Table S26). In the main text the weatherable land fraction rises from 0.5 to one over a ramp of width 0.10 Gyr ending at 2.45 Ga, and with the ramp of Kump and Barley (2007) the four glaciations occur at the same exponents, the first beginning at 2.448 Ga. With completion at 2.60 Ga, or at any earlier date up to the 2.90 Ga we integrated (the trajectories are then identical, because emergence is complete before the methane collapse begins), four glaciations and none after 2.22 Ga occur for ν from 0.720 to 0.730. The first glaciation then begins at 2.50 Ga, at the subaerial reductant step, and the prescribed crossing falls in the open water of the first interglacial. Because the glacial era then starts earlier, there is time for a fifth glaciation before 2.22 Ga, and one occurs just below that interval of ν, at the main text's principal exponent, with none later. The statement of Section S4.1 that no exponent gives more than four glaciations without later ice therefore holds for emergence completed near the main text's date and not in general. If the reductant step is moved earlier together with the emergence ramp, the four glaciations occur at $\nu = 0.7125$–0.725, the main text's own interval to within one grid step, and the first glaciation begins at 2.47 Ga. Completion at 2.40 Ga leaves three glaciations only, the first at 2.39 Ga. The edge for three or four lies at 2.380 ± 0.005 Ga, and the edge for exactly four, between 2.40 and 2.45 Ga, was not located more closely.

With the slower and later ramp of Bindeman et al. (2018), from 2.50 to 2.20 Ga, no exponent between 0.30 and 1.20 gives the recorded number of glaciations; there is no glaciation at all for $\nu \geq 0.715$ and a glacial era running past 2.22 Ga below it. By contrast, with completion at or before the end of the main text's ramp the model keeps the recorded glacial era and gives four glaciations at nearly the same exponents (Table S26). Because the model omits any dependence of the riverine phosphorus flux on the emerged area (Section 2.2 of the main text), earlier emergence changes the date of the first glaciation and leaves the oxygen source unchanged.

Table S22: Range of each assumed input over which some outgassing exponent in $[0.10, 1.46]$ gives three or four glaciations by 2.22 Ga with none after, and the displacement of the exponent ν^* that the glacial record fixes along that range. One axis varied at a time with the other seven at the values of the main text (Table 1 of the main text); edges are midpoints between the last surviving and the first failing value integrated, with half the spacing as the uncertainty. The threshold and nitrogen edges are where the interval leaves the scanned range of ν, so an interval below $\nu = 0.10$ is not excluded there; the nitrogen forcing between the two tabulated inventories is an interpolation, not a radiative calculation. Six of the eight inputs have such an edge inside or at the end of their published range (the weathering response time and the modern outgassing do not), and ν^* changes with every input. Exploratory integrations.

assumption (axis)	published range (source)	value used	three or four glaciations, none after 2.22 Ga, at some ν for	how the glacial era is lost; displacement of ν^*
glaciation threshold D^* ($\mathrm{W\,m^{-2}}$)	10.1 (Voigt et al., 2011) to 15.8 (Feulner et al., 2023); other model configurations 17.9, 21.4, 30.2	10.1	up to 14.715 ± 0.045 for $\nu \geq 0.10$; at 15.8 at most two glaciations at any ν	the interval moves to lower ν (-0.12 per $\mathrm{W\,m^{-2}}$) and leaves the scanned range
nitrogen inventory (bar)	0.5 (Som et al., 2016) to 1	1	down to 0.5675 ± 0.0075; none at 0.5	the interval moves to higher ν (-0.81 per bar) and closes when the glaciation after 2.22 Ga persists to higher ν than the third glaciation before it
weathering response temperature T_e (K)	5–15 conventional; 10–40 prior of Krissansen-Totton et al. (2018); 17.7 (Krissansen-Totton and Catling, 2017)	11.1	6.6 to 19.6 (± 0.1)	below the low edge the interval passes under $\nu = 0.10$; above the high edge its width shrinks to zero near 1.11 (0.10 per K)
weathering response time τ_{sil} (kyr)	170–380 (Colbourn et al., 2015)	380	the whole range	not lost; displaced by at most about 0.02 (central value: 0.74–0.76)
deglaciation CO_2 X (bar), with the sub-ice partition inside the Marinoan band at each X	0.01–0.1 (Hoffman et al., 2017; Abbot et al., 2012); partition: the band giving a Marinoan of 4–15 Myr	0.01, $\beta_{\mathrm{ice}} = 29.6$	every combination integrated except the lowest level with the longest-Marinoan partition (two glaciations); at 0.028 bar with the model's partition three only	exactly four occur only in the short-Marinoan half of the band once $X \lesssim 0.028$; ν^* within a few hundredths of 0.715
sub-ice venting fraction	no published determination; the model assumes ≤ 3 percent	zero	every value integrated, up to a tenth	not lost on the integrated range; ν^* rises by less than a hundredth
modern outgassing ($\mathrm{Tmol\,C\,yr^{-1}}$)	6–10 (Krissansen-Totton et al., 2018)	8	the whole range	not lost; four-glaciation interval 0.7275–0.7425 at 6, 0.6925–0.7125 at 10
emergence completion (Ga; ramp of width 0.10 Gyr)	2.20–2.90 (scheme A); published ramps Kump and Barley (2007) (2.51 Ga, 0.06 Gyr) and Bindeman et al. (2018) (2.50–2.20)	2.45	completion by 2.380 ± 0.005 or any earlier date (three glaciations only between the edge and 2.40); with the span of Bindeman et al. (2018), at no ν	late side only: completion after the edge leaves too few glaciations before 2.22 Ga and adds them after (0.06 per Gyr of earlier completion)
sub-ice carbon rule (structural alternative)	exchangeable store; fixed airborne fraction (glaciations of 41–44 Myr); crustal carrier with only the airborne excess returned (Le Hir et al., 2008a)	exchangeable	three or four under all three; exactly four with the exchangeable store (0.7075–0.7225) and with the crustal carrier (0.719–0.732); three, never four, with the fixed fraction	fixed fraction: no four-glaciation exponent (Fig. S6); crustal carrier: $\nu^* = 0.725$, where the third glaciation ends inside the Gordon Lake bound and the fourth begins before the upper Timeball Hill tuffs allow; near the interval's upper edge ($\nu = 0.73125$) the reverse, the Gordon Lake bound being missed by 2.0 Myr (Supplementary Text S1; Table 3 of the main text)
not assumptions in this sense: isotope inputs ($\delta_{\mathrm{in}} \pm 1$ per mil, f_A within one standard error, t_{ref} across its era bin); crossing epoch across 2.43–2.46 Ga	measured inputs; the onset window	-5, 0.137, 2.65 Ga; 2.4425 Ga	all	no effect on the existence of the four glaciations; ν^* moves by less than the interval's width; glacial dates shift by a few Myr

Table S23: Fraction of the Latin-hypercube samples of the eight inputs, drawn over the ranges of Table S22, in which some outgassing exponent gives the rock record's glacial era. The fraction is about half, and about two thirds when the glaciation threshold and the nitrogen inventory are held at the values used. Where the glacial era is lost, the cause is most often a steep weathering response or late emergence, and the higher glaciation threshold and the lower nitrogen inventory, each of which excludes the glacial era on its own, compensate when both are changed. $N = 400$ samples per scheme; fractions with Wilson ninety-five percent intervals; "four" is a lower bound (an integration with four rather than three glaciations found along the search). The strip $\nu < 0.10$ was not scanned: 111 scheme-A samples still had fewer than three glaciations at the scan floor, 8 of them with two, and if every one of those 8 had an interval below the floor the scheme-A fraction would be 0.47 (0.73 if all 111 did). A wider scheme with the threshold up to 30.2 $\mathrm{W\,m^{-2}}$ and T_e over 10–40 K was sampled only where it overlaps scheme A (200 samples, 0.61, 0.54–0.67); over its unsampled extension the fraction is bounded only between 0.03 and 0.98. Exploratory integrations.

scheme or subset	three or four, none after	four, none after (lower bound)	remark
A: all eight axes uniform over their ranges	0.45 (0.40–0.50)	0.28 (0.24–0.32)	179 of 400 survive
C: threshold 10.1 $\mathrm{W\,m^{-2}}$ and 1 bar nitrogen held, six axes sampled	0.64 (0.59–0.69)	0.54	
A at $\nu = 0.715$ held fixed	3.5% (2.1%–5.8%)	1.0%	small because ν is itself fixed by the glaciation count
A, T_e below 6.6 K	2 of 64		interval below the scan floor
A, emergence completed later than 2.38 Ga	3 of 103		too few glaciations before 2.22 Ga
A, neither of the two	0.71 (0.65–0.77)		prior mass 0.62
C, neither of the two	0.97		
A, threshold above its one-at-a-time edge	27 of 78 (0.35)		compensated by other axes
A, nitrogen below its one-at-a-time edge	29 of 54 (0.54)		compensated by other axes
A, threshold above its edge and nitrogen below 0.6 bar	11 of 21 (0.52; 0.32–0.72)		threshold and nitrogen compensate

ν^* over scheme-A survivors: median 0.64, central ninety percent 0.22–0.98, range 0.10–1.11; median half-width of a survivor's interval 0.015 (full widths 0.0025–0.1725); 12 survivor intervals contain 0.715. Over scheme-C survivors: median 0.71, central ninety percent 0.20–0.94.
Linear fit of ν^* over the 179 scheme-A survivors: -0.12 per $\mathrm{W\,m^{-2}}$ of threshold, -0.81 per bar of nitrogen, 0.10 per K of T_e, 0.06 per Gyr of earlier emergence (rms residual 0.05).

Table S24: Prior mass of each outcome over the $(\nu, t_\times)$ grid of Section S4.4 (553 integrations, 507 grid cells), with $t_\times$ flat on 2.43–2.46 Ga and ν flat on $[0, 1.46]$ or weighted by the product-of-uniforms prior of Krissansen-Totton et al. (2018); the last two rows are conditional on three or four glaciations and none after 2.22 Ga. For comparison, on the line $t_\times = 2.4425$ Ga alone the three-or-four interval holds 2.1% of the flat mass and 3.0% of the weighted mass, four alone 1.0% and 1.4%. Over most of the published range of ν crossed with the onset window the model does not give the recorded glacial era; where it does, the crossing falls under the first glaciation about five times in six and before it otherwise, never after a thaw. Because $t_\times$ is prescribed, these fractions describe the position of a prescribed date in its window under a flat prior and are not model predictions. Exploratory integrations.

outcome over the onset window and the published range of ν	ν flat	ν prior-weighted
no glaciation (the single smooth rise)	45%	25%
a glacial era running past 2.22 Ga	46%	64%
one or two glaciations only, none after	4%	5%
three or four glaciations, none after (record-consistent)	2.1%	2.8%
four (not three), none after	1.05%	1.45%
given three or four and none after: crossing under the first glaciation	84% (133 points)	84%
given three or four and none after: crossing before the first glaciation, in open water	16% (70 points)	16%

Table S25: The 21 values of the prescribed crossing epoch $t_\times$ inside the onset window 2.43–2.46 Ga at $\nu = 0.715$, grouped by whether the crossing falls under the first glaciation ($t_\times$ at or younger than 2.456 Ga) or before it ($t_\times$ at or older than 2.457 Ga). Four glaciations and none after 2.22 Ga occur at every value; methane at the glacial entry in ppmv; lead of the first ice over the prescribed crossing in Myr (negative: the crossing comes first, in open water). The boundary lies at 2.4565 Ga (±0.5 Myr) and moves 1.6 Myr younger per hundredth of increase in ν. Exploratory integrations.

	crossing under the first ice	crossing before the first ice
values of $t_\times$ inside the window	16 ($t_\times \leq 2.456$ Ga)	5 ($t_\times \geq 2.457$ Ga)
number of glaciations	four, none after	four, none after
methane at the glacial entry (ppmv)	0.73–3.77 (entry methane-assisted)	below one (entry on CO_2 alone)
first ice minus prescribed crossing (Myr)	up to +15.0; +8.4 at $t_\times = 2.4425$ Ga	−3.3 to −9.3
first-ice date across the window (Ga)	2.4450–2.4589 (range 14 Myr), later for younger $t_\times$ in the under-ice case	
open-water methane below ten ppmv (Ga), rock-record-consistent ν at $t_\times = 2.4425$	2.481–2.482 (30.5–31.9 Myr before the ice)[a]	

[a] Under the escape assumption of Section 2.2 of the main text, as in every methane entry of this table; about 12 Myr before the ice in the methane-only case of Supplementary Text S1 (Section S1.3).

Table S26: Emergence histories integrated with every other input at the values of the main text and ν fixed again by the glaciation count where an interval exists; the column "crossing" states where the prescribed crossing epoch 2.4425 Ga then falls relative to the first glaciation. Completion at any date from 2.45 Ga back to 2.90 Ga keeps four glaciations with none after 2.22 Ga at nearly the same exponent and moves only the first glaciation, whereas completion later than about 2.38 Ga, or the slow late ramp of Bindeman et al. (2018), removes the recorded glacial era at every exponent. Exploratory integrations.

emergence history (completion, Ga)	four glaciations, none after, for ν	first glaciation begins (Ga)	last thaw (Ga)	crossing
main text: ramp of width 0.10 Gyr ending 2.45	0.7075–0.7225 (edges)	2.4509	2.217	under the first ice
Kump and Barley (2007): begins 2.51, lasts 0.06 Gyr	the same values	2.448		under the first ice
completion 2.60 (and every earlier date to 2.90), reductant step unchanged	0.720–0.730	2.50	2.269	first interglacial, open water
the same, reductant step moved with the ramp	0.7125–0.725	2.47		first interglacial, open water
completion 2.40	none (three glaciations only, near 0.715)	2.39		before the first ice
completion later than 2.380 ± 0.005	none; nor three			
Bindeman et al. (2018): 2.50–2.20	none at any ν in 0.30–1.20 (no glaciation for $\nu \geq 0.715$; up to ten after 2.22 Ga below)			

Table S27: The four interpretations of an imposed excess of organic burial $E(t)$ and the terms each adds to the model. The carbon-isotope record fixes $E(t)$ in all four but not the carbon source or the fate of the oxygen. $W_{ox}O^{1/2}$ is the model's oxidative weathering of sedimentary organic carbon, which returns CO_2 as oxygen rises.

	carbon source	fate of the oxygen	term in the carbon equation	term in the oxygen equation
(a)	marine	to the air	$-E$ (burial), later returned through $W_{ox}O^{1/2}$	$+E$
(b)	marine	to crustal sulfide and iron	$-E$ (burial), not returned	none
(c)	external	to the air	supply $+E$ balances burial $-E$; $W_{ox}O^{1/2}$ then adds CO_2	$+E$
(d)	external	to crustal sulfide and iron	none	none (not integrated)

S5 Roles and frequencies of an imposed Lomagundi excursion

The model contains no internal mechanism for the Lomagundi–Jatuli excursion, the long positive excursion of carbonate $\delta^{13}C$ that follows the Paleoproterozoic glaciations. The organic burial fraction f_{org} in the model is interpolated linearly between its value at the crossing epoch $t_\times$ and the mean values for later eras derived from the carbonate $\delta^{13}C$ record. The modeled carbonate $\delta^{13}C$ after $t_\times$ follows from f_{org} through the isotope mass balance and therefore shows no excursion. At D. T. Johnston's request we ask instead how an excursion of the size seen in the carbon-isotope record changes the model's glacial chronology and atmospheric oxygen when it is imposed as a forcing, and how often each outcome occurs across the outgassing exponents that the glacial record allows. We added to the marine organic burial flux an excess $E(t) = \Delta f_{org}(t)\, V_{out}(t)$ whose timing and amplitude are taken from the carbon-isotope record, and integrated the model with this term under each of three interpretations of where the buried carbon comes from and where the released oxygen goes. We ran these simulations after the comparisons of the main text had been specified and completed, and they are not part of that set.

The timing of $E(t)$ follows either the age constraints of Martin et al. (2013) or the compiled curve of Edmonsond and Dyer (2026). With the age constraints, the onset of the excursion falls near the onset of the model's third glaciation, after it in some simulations and before it in others, whereas the rise of the compiled curve begins earlier, within the model's first glaciation. The amplitude of $E(t)$, expressed as the peak excess Δf_{org} of the organic burial fraction, takes three values, from 0.19 to 0.36, which come from the peak carbonate $\delta^{13}C$ of the excursion (the peaks of the compiled curve and the section maxima of Schidlowski et al., 1976 and Karhu and Holland, 1996) through the isotope mass balance of Krissansen-Totton et al. (2015). The excess oxygen released, integrated over the whole excursion with ice-covered intervals included, is 12 to 26 times the present atmospheric inventory, compared with the 12 to 22 inventories estimated by Karhu and Holland (1996). We set E to zero during glaciations, however, because the model's ocean is then capped and the oxygen from sub-ice organic burial is consumed below the ice, and the excess actually applied is therefore smaller than this integral. We imposed the excursion, with both timings and all three amplitudes, at the twelve exponents that the glacial record allows when the other inputs are held at the values of Table 1 of the main text. Of these exponents, six give four glaciations beginning before 2.22 Ga and none after, and the rest give three. The combinations of timing, amplitude and exponent give 72 simulations under each of the three interpretations of the excursion.

The carbon-isotope record constrains the extra net burial but not the source of the buried carbon or the fate of the released oxygen, and the effect of the excursion in the model depends on both (Table S27). If the carbon is marine, drawn from the ocean–atmosphere reservoir the model resolves, the extra burial is a sink of CO_2 as well as a source of O_2; if it is supplied from outside that reservoir at the rate it is buried, the supply balances the burial and no net CO_2 is removed. The oxygen either enters the air, where the model's oxidative weathering of old organic carbon rises with it and returns CO_2, or is consumed by crustal sulfide and ferrous iron, a sink the model does not have, before it can reach the air. The fourth combination (d), external carbon with the oxygen consumed in the crust, adds no term to the model's carbon equation or to its oxygen equation, and because it can have no effect in the model we integrated only the other three combinations.

Under interpretation (a), marine carbon with the oxygen to the air, the excursion ends the glacial cycling in none of the 72 simulations (Table S28, Fig. S10). The number of glaciations is unchanged in 53 of them, with the last thaw at most 17 Myr earlier. In 15 simulations a fourth glaciation is added before 2.22 Ga at exponents that otherwise give three, an outcome still consistent with the glacial record, and in 4 others a glaciation is added after 2.22 Ga. The additions arise because the air must accumulate oxygen before oxidative weathering returns the buried carbon, so the rising excess burial is for a time a net sink of CO_2.

Table S28: Frequency of each outcome of the imposed excursion over the 72 simulations per interpretation (twelve exponents allowed by the glacial record, two timings, three amplitudes). "Consistent" means three or four glaciations beginning before 2.22 Ga and none after; the comparisons with individual dated beds were not repeated on these simulations. Only under interpretation (c), in which the imposed excursion is a net source of CO_2 and warms the planet, can the excursion end the cycling early.

interpretation	ends cycling early	of which consistent	adds after 2.22 Ga	adds one before 2.22 Ga	change of the last thaw
(a) marine C, O_2 to air	none	n.a.	4	15	up to 17 Myr earlier (number unchanged, 53 cases)
(b) marine C, O_2 to crust	none	n.a.	72 (three to four added in each)	none	123–254 Myr later (imposed end of E)
(c) external C, O_2 to air	67	18	none	none	70–83 Myr earlier (consistent cases)
(d) external C, O_2 to crust	none	n.a.	none	none	none (no term)

Late in the glacial era, when the ice-free steady-state CO_2 is only slightly above the glaciation threshold, that transient sink is enough to produce one more glaciation. The oxygen held in the air during the excursion, 0.09 to 0.39 PAL from the lowest to the highest amplitude, is close to the steady-state value at which oxidative weathering $W_{ox}O^{1/2}$ balances the imposed flux E, namely the square of E/W_{ox} with W_{ox} fixed by the modern oxygen budget. The oxygen maxima in the simulations are 0.98 to 1.17 times this value. These oxygen levels are therefore set by the imposed excursion and the modern oxygen budget; they exceed the paleosol floor of 0.14 PAL (Rye and Holland, 1998) at the middle and high amplitudes only. The model's carbonate $\delta^{13}C$ does not reproduce the excursion under (a), or under (c) below, because the oxidative weathering flux that returns isotopically light carbon rises with the oxygen and offsets the isotopic effect of the extra burial.

Under interpretation (b), marine carbon with the oxygen consumed in the crust, the uncompensated CO_2 sink adds three to four glaciations after 2.22 Ga in 72 of the 72 simulations, none of which remains consistent with the glacial record. The last thaw then falls between 2.097 and 2.026 Ga, during the imposed decay of the forcing and 123 to 254 Myr later than without the excursion. Because that date is set by the prescribed end of the excursion, it is an input of these simulations and not a prediction of the model. The carbonate $\delta^{13}C$ rises 4.9 to 10.0 per mil above the baseline, a rise that is the imposed excess burial expressed through the isotope mass balance and is therefore also an input, and the oxygen in the air is unchanged because under (b) the released oxygen is consumed in the crust.

Under interpretation (c), external carbon with the oxygen to the air, the CO_2 returned by oxidative weathering is a net source that warms the planet, and the excursion ends the glacial cycling early in 67 of the 72 simulations. Glaciations whose onset falls after the onset of the excursion are removed and earlier ones are kept. With the excursion onset of Edmonsond and Dyer (2026), which falls inside the model's first glaciation, only the first glaciation survives and the air is oxic from the first thaw, near 2.425 Ga, at all exponents; none of these cases is consistent with the glacial record. With the excursion onset of Martin et al. (2013), the model at the six exponents that otherwise give four glaciations loses the fourth at all three amplitudes and remains consistent with the glacial record (18 cases), with its last thaw 70 to 83 Myr earlier, at 2.292–2.285 Ga. At the exponents that otherwise give three glaciations it loses the third and becomes inconsistent with the glacial record, except where that glaciation had already begun when the excursion started. The removal of the later glaciations under (c) depends on two features of the model, namely that buried organic carbon is returned to the air as CO_2 one for one by oxidative weathering once oxygen is present, and that the external supply is assumed equal to the realized extra burial.

The imposed excursion changes at least one model quantity in every simulation under the three interpretations. The 10 simulations whose glacial dates move by less than a million years (4.6% of the total) all fall under interpretations (a) or (c), in which the oxygen reaches the air, and even in these the oxygen level during the excursion rises by more than an order of magnitude. The frequency with which the excursion ends the cycling early is zero under interpretations (a), (b) and (d), because under those interpretations the excess burial is not a net source of CO_2 that could warm the model's climate. Under interpretation (c) it is 67 in 72, and 18 of the simulations in which the cycling ends early remain consistent with the number of glaciations in the rock record. The frequencies are counts over a grid of exponents at one setting of the other inputs, and the binomial (Wilson) confidence interval of the frequency under (c), 0.85–0.97, reflects only the finite size of that grid; frequencies across the joint range of the assumptions of Supplementary Text S4 were not computed.

Under interpretation (c) with the timing of Martin et al. (2013), whether a given glaciation survives depends on whether its onset precedes the onset of the excursion, and therefore on the onset age adopted

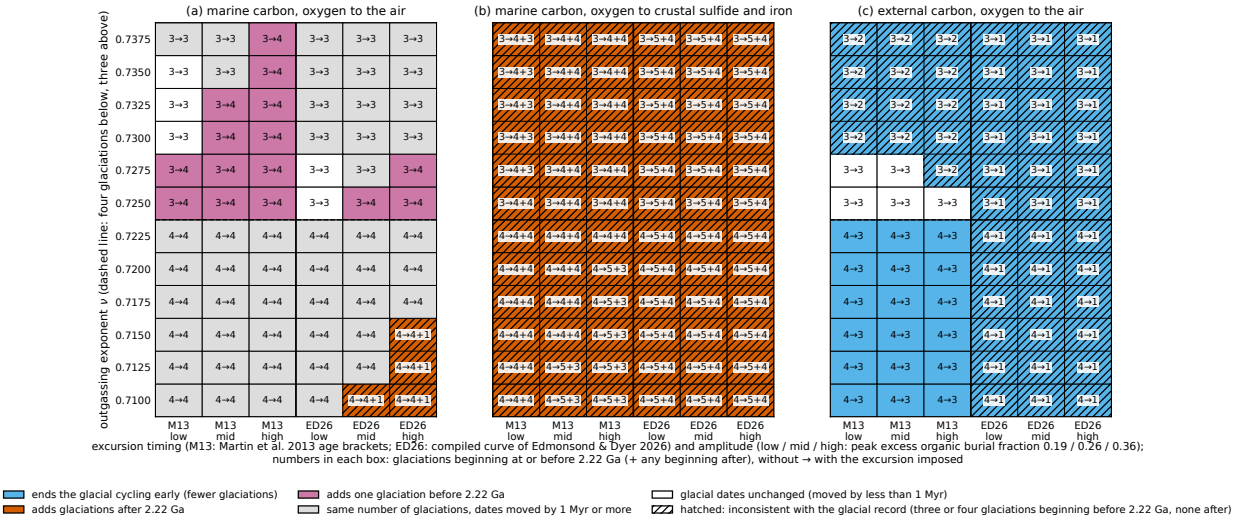

Figure S10: Number of model glaciations with and without an imposed Lomagundi excursion under three interpretations of the excursion. Each panel shows the twelve outgassing exponents allowed by the glacial record (rows; four glaciations below the dashed line, three above) against the two timings and three amplitudes of the imposed excess burial (columns); the boxes give the number of glaciations beginning at or before 2.22 Ga, plus any beginning after, without and with the excursion. (a) Marine carbon with the oxygen to the air leaves the number of glaciations unchanged except where its transient CO_2 sink adds one. (b) Marine carbon with the oxygen consumed in the crust adds further glaciations late in the glacial era in all cases. (c) External carbon with the oxygen to the air removes the glaciations that would begin after the excursion's onset. Hatching marks outcomes inconsistent with the glacial record. The effect of the excursion on the number of glaciations thus depends chiefly on the assumed source of the carbon and fate of the oxygen rather than on the exponent. Exploratory integrations.

from that chronology, and not on the amplitude. In the simulations that stay consistent with the glacial record the glaciation removed is the last one, and the imposed excursion therefore also changes the model's date of permanent oxygenation. The model's last thaw, which marks the onset of permanent oxygenation, then moves 70 to 83 Myr earlier, toward the older of the two permanence dates that have been inferred from the sulfur isotope record (Section 5.2 of the main text), although this shift is not evidence for either date.

Table S29: Archean phosphate factor, productivity factor, marine burial and phosphorus-budget requirement for three strengths k_0 of the Archean iron trap. Columns two to four give the phosphate factor $P_A/(P_A + P_h)$, the productivity factor p_A re-derived so that marine burial equals $N_A = 2.069$ Tmol C yr^{-1}, and the resulting Archean marine burial B_{mar}. The next column lists the organic C:P that N_A then requires at the reactive-phosphorus delivery $W_P = 0.10$ Tmol P yr^{-1} of Laakso et al. (2020). The last column gives the smallest product $r\,W_P$ of organic C:P and phosphorus delivery that can supply the burial N_A through the trap in steady state. The value $k_0 = 10$ is the model's; 4 and 60 were simulated as alternatives. The glacial chronology, the date of first oxic air and the later oxygen level are the same in the three simulations to within the small differences given in the text, and only the phosphorus budget (last two columns) constrains the trap strength.

k_0 (Archean)	$P_A/(P_A + P_h)$	p_A	marine burial B_{mar} (Tmol C yr^{-1})	organic C:P required at W_P = 0.10 Tmol P yr^{-1}	smallest $r\,W_P$ that supplies N_A (Tmol C yr^{-1})
4	0.97	0.32	2.07	103	10.3
10 (model)	0.93	0.33	2.07	228	22.8
60	0.70	0.44	2.07	1262	126

S6 The phosphorus ceiling and the iron trap

Dissolved phosphate P, measured in units of the concentration that modern riverine delivery would support in an ocean without iron-oxide scavenging, relaxes in the model toward its quasi-steady value with an e-folding time of 222 yr, so that at every age of interest

$$P = \frac{W_P}{1 + k_s}, \qquad k_s = \frac{k_0(t)}{1 + (O/O_d)^4}. \tag{S9}$$

Here W_P is the riverine phosphate delivery, held at its modern value ($W_P = 1$ in these units) at all Archean and Paleoproterozoic ages and raised only during the Neoproterozoic pulse described in Supplementary Text S1. The scavenging ratio k_s is the removal of phosphate on iron oxides relative to its removal with organic matter. The strength of this iron trap is $k_0 = 10$ before 0.72 Ga, declining to 1.67 after 0.55 Ga (Reinhard et al., 2017), and it switches off when atmospheric oxygen O passes $O_d = 0.3$ PAL and the deep ocean oxygenates. The delivery W_P carries no continental-emergence factor, although the model halves continental weatherability for silicate and carbonate weathering before 2.55 Ga; the effect of this omission on the phosphorus budget is estimated at the end of this Text. In the anoxic ocean of the Archean and Paleoproterozoic, then, $P = 1/(1 + k_0) = 0.091$ of the modern level: of every eleven phosphorus atoms delivered, ten leave the ocean on iron oxides without carbon and one leaves with organic matter.

Marine organic burial in open water is $B_{\mathrm{mar}} = a_{\mathrm{mar}}\, p(t)\, P/(P + P_h)$, where $a_{\mathrm{mar}} = 6.67$ Tmol C yr^{-1} is the modern marine burial (the total organic burial of Holland, 2002, multiplied by the marine share of Burdige, 2005), $p(t)$ is a productivity factor equal to one today, and $P_h = 0.007$ is an assumed half-saturation constant. With this P_h the phosphate factor $P/(P + P_h)$ is 0.93 in the Archean and 0.99 today. The Archean productivity factor p_A is fixed by requiring that $a_{\mathrm{mar}}\, p_A\, P_A/(P_A + P_h)$, where P_A is the Archean phosphate level found above, equal the net Archean burial $N_A = f_A V_{\mathrm{out}}(t_{\mathrm{ref}}) = 2.069$ Tmol C yr^{-1} implied by the carbon-isotope mass balance ($f_A = 0.137$, Krissansen-Totton et al., 2015; $t_{\mathrm{ref}} = 2.65$ Ga), which gives $p_A = 0.332$. Archean burial is therefore set by the isotope mass balance; phosphate enters it only through the factor $P_A/(P_A + P_h)$, which is close to one, and any change in that factor is compensated by the re-derived p_A.

Because p_A is re-derived to keep Archean burial equal to N_A for any trap strength, the Archean value of k_0 has no effect on the glacial chronology (Table S29). With $k_0 = 4$ or 60 in place of 10 the productivity factor is re-derived to 0.32 or 0.44 in place of 0.33 and Archean marine burial B_{mar} is the same 2.07 Tmol C yr^{-1}. The four glaciations then begin and end at the same dates in all three simulations (to within 1.8×10^{-8} Gyr), the date of first oxic air moves by at most 0.12 Myr, and the oxygen level after the transition changes by a relative amount 4.6×10^{-7}. The three simulations differ only after the trap begins to weaken in the Neoproterozoic. The trap strength k_0 is constrained instead by the steady-state phosphorus budget of the ocean.

In steady state every phosphorus atom delivered to the ocean is eventually buried, either with organic matter of molar C:P ratio r or on iron oxides without carbon. If the oxide route takes the fraction $k_s/(1+k_s)$, the bulk sediment carries organic carbon and phosphorus in the ratio $\rho_{\mathrm{bulk}} = r/(1 + k_s)$, and net oxygen production, which equals net organic carbon burial at one O_2 per carbon atom, cannot exceed $\rho_{\mathrm{bulk}} W_P$, which is the bound of Laakso and Schrag (2017). D. T. Johnston derived the bound in this form from the phosphorus balance of Laakso et al. (2020), in which the burial efficiency and the upwelling flux cancel from the steady-state product, and proposed its use as an upper limit on the model's Archean oxygen source N_A. The model's equations do not enforce this steady-state identity between phosphorus delivery and phosphorus

Table S30: The phosphorus budget of the Archean oxygen source, $N_A = 2.069$ Tmol C yr^{-1}, for three values of the riverine phosphorus delivery W_P. The bound net O_2 production $\leq \rho_{\text{bulk}} W_P$, $\rho_{\text{bulk}} = r/(1 + k_s)$ (Laakso and Schrag, 2017), is respected at reactive-phosphorus delivery ($W_P \geq 0.10$ Tmol P yr^{-1}; Laakso et al., 2020) for organic C:P of a few hundred (above the Redfield ratio), and not at the dissolved flux of 0.04 Tmol P yr^{-1}. At the Redfield ratio of 106 and $W_P = 0.04$ the permitted source is 0.39 Tmol O_2 yr^{-1} and the largest consistent trap strength is $k_0 = 1.0$; at C:P of 250 and $W_P = 0.10$ they are 2.27 Tmol O_2 yr^{-1} and 11.1.

	$W_P = 0.04$ (dissolved flux, modern steady state)	$W_P = 0.10$ (reactive P; Laakso et al., 2020)	$W_P = 0.20$ (largest considered)
bulk-sediment C:P required, N_A/W_P	51.7	20.7	10.3
organic C:P required through the trap ($k_0 = 10$)	569	228	114
organic C:P required at $k_0 = 60$	3156	1262	631
net O_2 source permitted at organic C:P of 300 (Tmol yr^{-1})	1.09	2.73	5.45
largest k_0 consistent with N_A at organic C:P of 300	4.8	13.5	28

burial, because organic carbon burial is imposed by the isotope mass balance and P in equation (S9) is dimensionless, affecting burial only through the phosphate factor $P/(P + P_h)$. Whether the model's Archean fluxes respect the resulting bound therefore has to be tested separately, with W_P and r in physical units (Table S30).

The Archean oxygen source $N_A = 2.069$ Tmol C yr^{-1} requires a bulk-sediment C:P of $N_A/W_P = 51.7$, 20.7 or 10.3 for a delivery of 0.04, 0.10 or 0.20 Tmol P yr^{-1}. These three deliveries are respectively the dissolved riverine flux used to fix the model's modern steady state, the reactive-phosphorus delivery of Laakso et al. (2020), and the largest delivery we considered. Through the model's trap ($k_0 = 10$, ten of eleven phosphorus atoms scavenged) the organic matter must then carry C:P of 569, 228 or 114; equivalently the bound is respected when $r\,W_P \geq N_A(1 + k_0) = 22.8$ Tmol C yr^{-1}. At reactive-phosphorus delivery the required organic C:P is therefore higher than the Redfield value of 106 for modern plankton and lower than two estimates for buried organic matter. Modern total burial divided by the dissolved flux implies an organic C:P of 250, and values up to 300 have been reported for organic matter buried beneath anoxic water (Algeo and Ingall, 2007).

At the dissolved flux of 0.04 Tmol P yr^{-1} the required organic C:P exceeds the Redfield ratio and both estimates for buried organic matter, and at the Redfield ratio the permitted source falls short of N_A by a factor of 5.4. The most favorable combination, C:P of 300 with delivery 0.20 Tmol P yr^{-1}, permits 5.45 Tmol O_2 yr^{-1}, of which N_A is 38%; with no iron trap at all, Redfield organic matter at that delivery would permit 21.2 Tmol O_2 yr^{-1}. Solved for k_0 at the isotope-implied burial N_A, the identity gives an upper bound on the Archean trap strength, $k_0 \leq rW_P/N_A - 1$: at most 28 for that most favorable combination, 11.1–13.5 at reactive-phosphorus delivery with C:P of 250–300, and 4.8 or less at the dissolved flux. The model's $k_0 = 10$ is therefore consistent with this upper bound if phosphorus was delivered at the reactive rate or faster and the buried organic matter carried C:P above the Redfield ratio (a few hundred at the reactive rate), and exceeds it if only the dissolved flux was available. A trap of strength $k_0 = 60$ would require organic C:P of at least 631 even at the highest delivery and is inconsistent with the phosphorus budget at all three deliveries, although it leaves the glacial chronology unchanged. For comparison, the same identity applied to the modern ocean, with marine burial of 6.67 Tmol C yr^{-1} over the dissolved flux, gives a bulk C:P of 167 (250 with terrestrial burial included, the estimate for buried organic matter used above).

Two simplifications of the model qualify these results, one in the riverine phosphorus flux and one in the dependence of production on phosphate. First, riverine phosphorus carries no emergence factor while continental weatherability is halved before 2.55 Ga, a coupling of phosphorus delivery to emergence that Bekker and Holland (2012) and Minsky et al. (2026) include. If W_P carried the same factor, the Archean delivery would be half of each nominal value, the required organic C:P would double, and the bound would be respected only at the highest delivery, with organic C:P of at least twice 114. Second, the phosphate factor remains near saturation after an elevenfold drawdown of phosphate only because the half-saturation constant $P_h = 0.007$ is below one hundredth of the modern phosphate level, and P_h is an assumed constant with no independent estimate.

Grettenberger and Sumner (2024) propose that physiology rather than nutrient availability limited primary productivity after the emergence of oxygenic photosynthesis. The model contains no microbial physiology: its oxygen source is the burial flux fixed by the carbon-isotope mass balance times the phosphate factor $P/(P + P_h)$, which stays near one throughout, as shown above. A physiological limit of the kind they propose could therefore only hold the source below that burial flux and delay the epoch at which the source

overtakes the sinks. Because that epoch is prescribed (equation (3) of the main text), the model cannot test their proposal, a limitation and an argument raised by D. T. Johnston.

S7 Testing published models

Alcott et al. (2019) proposed, using a fourteen-reservoir ocean–atmosphere network, that internal biogeochemical feedbacks convert a smooth decline in the input of reduced gases into a sequence of oxygenation steps, so that no stepwise forcing is required, and Goldblatt et al. (2006) obtained two stable states of atmospheric oxygen in a three-reservoir model. In the three-reservoir model the two states, one low and one high in oxygen, coexist over a range of reductant inputs. We solved both models for the complete set of their steady states at parameter values their authors published, for the first chiefly at one setting of its two burial feedbacks and at the reductant input of its Great Oxidation (Table S32 lists every input and setting solved), with interval bounds that enclose every root and rule out any other root in the search region. We also integrated the fourteen-reservoir network forward in time, from a wide set of initial conditions at that setting and under its authors' declining input at the settings of their own time-dependent simulations. Only the outcome for each model appears in the main text (Section 5.1); the equations we solved, the enumeration of steady states, the forward integrations and the limitations of these calculations are given here.

S7.1 The question and the method

Alcott, Mills, and Poulton argued in a 2019 *Science* paper that stepwise oxygenation emerges from the ocean–atmosphere network governed by a set of 14 coupled ODEs, "an inherent property of global biogeochemical cycling" (Alcott et al., 2019). Although these ODEs can be integrated forward in time, the complete set of stable equilibria of the model was not determined. Moreover, numerical root-finding can find roots but can never prove it found all of them. Whether the model even has multiple stable oxygen states was untested. Steps can arise in such a model in two ways. If two or more stable steady states, that is, configurations of the reservoirs at which every flux balances and small perturbations decay, coexist at fixed boundary conditions, the system can jump between them, and where they coexist over a range of the forcing it can also switch back; this is the mechanism of Goldblatt et al. (2006). If instead the steady state is unique at each value of the forcing but moves sharply over a narrow range of it, a slowly declining forcing produces a step with no coexistence of states, and over some ranges the steady state may give way to a periodic solution. According to Alcott et al. (2019), their model behaves in the second way: their Fig. 3 shows one steady-state branch at each reductant input, with breaks where the solution oscillates. Determining the complete set of stable steady states at fixed forcing distinguishes the two cases and establishes whether the network has a stable oxygenated state, a stable anoxic state, or both at the same boundary conditions. Such an enumeration does not detect periodic solutions, in which the atmosphere may pass repeatedly between the two conditions with no stable steady state of either kind (their Fig. 4A); we look for those by forward integration.

Writing the model as $\dot{\mathbf{x}} = \mathbf{F}(\mathbf{x})$ for the vector $\mathbf{x}$ of its fourteen reservoirs, we determine the set of stable steady states inside an admissible region B of reservoir values,

$$\left\{ \mathbf{x}^* \in B : \ \mathbf{F}(\mathbf{x}^*) = \mathbf{0},\ \mathrm{Re}\,\lambda < 0 \text{ for every eigenvalue } \lambda \text{ of } (\partial\mathbf{F}/\partial\mathbf{x})(\mathbf{x}^*) \right\}, \tag{S10}$$

at the constants of their Tables S1–S3. We set the two burial feedbacks, the redox-dependent fractions of authigenic and of organic phosphorus burial, at 0.10 and 0.10, the weakest of the three settings drawn in their Fig. 3 and the setting of the released codes. The reductant input is that of the time-dependent simulation of Alcott et al. (2019) between 2.45 and 2.0 Ga (their Fig. 5A, in which that input declines linearly from 4.5×10^{13} mol O_2-equivalent per year at 4 Ga to zero today). That simulation itself uses stronger feedbacks, 0.50 and 0.25; we integrate the network at those values below but enumerate its steady states in this range of input only at 0.10 and 0.10. In their steady-state diagram (their Fig. 3A) this input exceeds, for each feedback setting drawn, the threshold of about 1.5×10^{13} mol O_2-equivalent per year above which the steady states are anoxic, so the enumeration characterizes the pre-oxidation branch of that diagram at burial feedbacks of 0.10 and 0.10 and tests whether an oxygenated steady state already coexists there with the anoxic one. The region B bounds every reservoir by published constraints and spans atmospheric oxygen from 10^{-8} to 2 times the present atmospheric level (PAL), so that the neighborhood of the modern oxygenated ocean and atmosphere lies inside it.

We solve the steady-state system algebraically rather than by integration. Ten of the fourteen balance equations are linear in ten of the unknowns once the other four are given, with coefficients whose non-vanishing over the whole of B can be proved (constant rational pivots, and one four-by-four block whose determinant is shown sign-definite over B by exact Sturm sequences). These ten unknowns can therefore be eliminated without approximation, leaving a system in four unknowns, proximal and distal shelf phosphorus, deep-ocean oxygen and the square root of atmospheric oxygen, with every logistic switch, Monod term and piecewise burial law of the original intact. The eliminated equations vanish identically under the substitution, so the roots of the reduced system and of the full one correspond one to one. We then cover the four-dimensional region with boxes and apply interval arithmetic to each: a box is either proved to contain no root or proved,

by a Krawczyk test, to contain exactly one, and boxes that are neither are subdivided until every box is decided. Each root is then back-substituted to recover all fourteen coordinates in interval arithmetic, confirmed to lie inside B, and re-proved as a root of the full fourteen-dimensional system; its stability follows from interval enclosures of the fourteen eigenvalues of the full Jacobian, each of which excludes the imaginary axis. An independent implementation in a different interval-arithmetic library reproduced all the enclosures and stability signs, and 10^4 quasi-random damped-Newton starts per system converged only to roots inside the proved enclosures; such restarts could have refuted the completeness of the enumeration but cannot establish it. We first tested the method on synthetic systems of the same structure with known roots and stabilities, which it recovered correctly.

Steady states of oxygenation models have been determined before by other means. Goldblatt et al. (2006) reduced their own model exactly to a scalar root problem, and Daines and Lenton (2016) recomputed its equilibrium diagram from steady states "derived by integrating to convergence". Olejarz et al. (2021) derived closed-form conditions for bistability and hysteresis in an ecological model of oxygenation; Wortmann et al. (2025) re-implemented a published box model and compared its output with the original figures. Gregory et al. (2021) raised the question of stability for their own network and stated the limits of their analysis ("This suggests, but does not fully prove"; "A full stability analysis requires time-dependent computations beyond the scope of this effort"). Williams et al. (2019) swept parameters of a model in the same family and reported the steady states that a numerical solver returned at each value. Relative to these studies we also prove, by the interval cover, that no steady state inside the region was missed; the statement that the 2019 network has no oxygenated steady state in B requires that proof, since failing to find such a state numerically does not show that none exists.

S7.2 Alcott, Mills and Poulton (2019) at published values

The network of Alcott et al. (2019) tracks phosphorus, carbon and oxygen in four ocean boxes and the atmosphere, in the lineage of the COPSE model (Lenton et al., 2018), and closes the fourteen balances with logistic switches, a Monod term and piecewise burial laws. We solved it at the constants of their Tables S1–S3, with the two burial-feedback parameters at 0.10 and 0.10 and the reductant input at 2.505×10^{13} mol O_2-equivalent per year, the midpoint of the values through which the declining input of their Fig. 5A passes between 2.45 and 2.0 Ga. We also solved it at the two ends of that range, 2.25×10^{13} and 2.76×10^{13}. In this range of input we did not solve the network at other values of the two burial-feedback parameters, neither the 0.50 and 0.25 of their Figs. 4A and 5A nor the still stronger feedbacks for which Alcott et al. (2019) report an oscillating solution at a similar input (their Fig. 4B); the one enumeration at 0.50 and 0.25 is at a lower input (Table S32, point R1). The printed equations and the released code of the model differ in fourteen details, one of them the form of a flux term, and we solved the model both as printed and as coded. Neither version has an oxygenated steady state in B, and as printed the model has no steady state in B at all; the result below therefore does not depend on this choice. For one closure, the dependence of the reductant flux on the oxidation state, the published description is consistent with three functional forms: the constant printed in the methods and two sigmoid forms with different midpoints, both of which reproduce the published figures of the model. We refer to these as the constant closure and the sigmoid closures with midpoints at 10^{-5} and 10^{-6} PAL of atmospheric oxygen, the level at which the reductant sink is half suppressed (sigmoid A and B in Table S31; both have slope 3 per decade of oxygen in the released codes). We state the result for the two sigmoid closures and report the constant closure alongside them. Because the burial laws change form at the present-day deep-ocean oxygen level, each closure gives two algebraic systems, one on each side of that level, and six systems are solved in all.

We solved the model exactly at the authors' published parameter values and find at most one stable equilibrium, and it lies below 10^{-4} of the present oxygen level. Table S31 lists the enumeration by system. Under either sigmoid closure the region B contains a single steady state, which is stable and anoxic. Under sigmoid closure A atmospheric oxygen is 2.4318×10^{-5} PAL and deep-ocean oxygen 1.0440×10^{-8} of its present value, with the two shelf phosphorus reservoirs at 1.196 and 2.873 times their present values; under sigmoid closure B the corresponding oxygen values are 2.4388×10^{-6} PAL and 1.047×10^{-9}. Both states lie far below the threshold of 10^{-3} PAL that separates anoxic from oxic in this analysis; the first lies above, and the second below, the sulfur-isotope threshold of 10^{-5} PAL used in the main text. Each state lies just above the midpoint of its closure, where that closure suppresses the reductant sink, and the two states bracket the level near 10^{-5} PAL at which the model atmosphere of Alcott et al. (2019) rests before its oxidation (their Fig. 3A). Under either closure the state we find therefore lies on the pre-oxidation branch of their steady-state diagram at this reductant input, and the interval enumeration proves in addition that no other steady state, and in particular no oxygenated one, coexists with it anywhere in B. Both states are interior: no enclosure touches a face of the region, the switch of the burial laws, or the oxygen floor. All fourteen eigenvalue enclosures at each state lie strictly in the left half-plane, the slowest mode decaying at 6.6284×10^{-6} yr^{-1}

Table S31: The complete set of steady states of the Alcott et al. (2019) network inside the admissible region B (atmospheric O_2 from 10^{-8} to 2 PAL; every reservoir within published bounds) at the constants of their Tables S1–S3 with burial feedbacks (P_{auth}, P_{org}) of 0.10 and 0.10 and reductant input 2.505×10^{13} mol O_2-equivalent per year, by form of the reductant closure and by piece of the burial law (o is deep-ocean oxygen relative to present; the law changes form at $o = 1$). For every entry the interval method proves that no other root lies in the region; the one steady state under each sigmoid closure is stable in all fourteen dimensions and anoxic (below 10^{-3} PAL; the sigmoid-A state lies above the 10^{-5} PAL sulfur-isotope threshold of the main text). Sigmoid A and B are the closures whose midpoints lie at 10^{-5} and 10^{-6} PAL of atmospheric oxygen, the two values found in the released codes; both have slope 3 per decade of oxygen.

reductant closure	burial-law piece	steady states in B	stable	atmospheric O_2 of the state (PAL)
sigmoid A	$o < 1$	one	one	2.4318×10^{-5}
sigmoid A	$o \geq 1$	none	none	n.a.
sigmoid B	$o < 1$	one	one	2.4388×10^{-6}
sigmoid B	$o \geq 1$	none	none	n.a.
constant (as printed)	$o < 1$	none	none	n.a.
constant (as printed)	$o \geq 1$	none	none	n.a.

Table S32: Steady states of the Alcott et al. (2019) network inside B at every reductant input we solved (mol O_2-equivalent per year), each enumeration proved complete by the interval method: the two ends and the midpoint of the range through which the forcing of their Fig. 5A passes between 2.45 and 2.0 Ga, at burial feedbacks (P_{auth}, P_{org}) of 0.10 and 0.10, and the input of 10^{13} at which they report a limit cycle, at the same feedbacks (point N1) and at the 0.50 and 0.25 of their Figs. 4A and 5A (point R1), both under sigmoid closure B only. The midpoint rows repeat Table S31. Under the constant closure the region contains no steady state at any of the first three inputs. At burial feedbacks of 0.10 and 0.10 the unique steady state is anoxic throughout the Great Oxidation range and oxygenated below the oxidation threshold of their Fig. 3A; with feedbacks of 0.50 and 0.25 at the lower input the one steady state is unstable and no stable state exists, consistent with the oscillation they report there. No row combines 0.50 and 0.25 with an input in the Great Oxidation range; that combination was integrated in time (see text) but not enumerated.

reductant input	burial feedback	closure	steady states in B	stable	atmospheric O_2 (PAL)
2.25×10^{13}	0.10, 0.10	sigmoid A	one	one	3.7171×10^{-5} (anoxic)
2.25×10^{13}	0.10, 0.10	sigmoid B	one	one	3.7375×10^{-6} (anoxic)
2.505×10^{13}	0.10, 0.10	sigmoid A	one	one	2.4318×10^{-5} (anoxic)
2.505×10^{13}	0.10, 0.10	sigmoid B	one	one	2.4388×10^{-6} (anoxic)
2.76×10^{13}	0.10, 0.10	sigmoid A	one	one	1.8530×10^{-5} (anoxic)
2.76×10^{13}	0.10, 0.10	sigmoid B	one	one	1.8565×10^{-6} (anoxic)
10^{13} (N1)	0.10, 0.10	sigmoid B	one	one	0.702 (oxygenated)
10^{13} (R1)	0.50, 0.25	sigmoid B	one	none	0.980 (oxygenated, unstable)

(a timescale near 150 kyr) and the fastest at 46.77 yr^{-1}. Under the constant closure the region contains no steady state. No oxygenated steady state exists anywhere in B under any of the three closures, although B extends to twice the present oxygen level. At both ends of the model's Great Oxidation range of reductant input the structure is the same as at the midpoint, one stable anoxic state under each sigmoid closure and none under the constant closure (Table S32).

Widening the bounds of B on each of the thirteen reservoirs other than atmospheric oxygen by a factor of ten produced no further root, and when we continued the modern oxygenated state numerically, raising the reductant input toward the Great Oxidation value at which the enumeration was made, that state merged into the anoxic one. At a lower input on the same path the steady state is again unique: at a reductant input of 10^{13} mol O_2-equivalent per year, below the oxidation threshold of their Fig. 3A, the network with burial feedbacks of 0.10 and 0.10 has, under sigmoid closure B, a single steady state, stable and oxygenated, at 0.702 PAL (Table S32; we did not solve this input under closure A). As the reductant input declines from the Great Oxidation values to that input, the network therefore passes from a unique anoxic state to a unique oxygenated one, which is the step mechanism its authors describe. The anoxic and the oxygenated state do not coexist at any input we solved, and with the feedbacks of their Fig. 4A at that lower input the network has no stable steady state, consistent with the oscillation they report there (point R1 of Table S32).

Because the only stable state in B at the Great Oxidation reductant input is anoxic, the network cannot remain in an oxygenated state there, and any oxygenation it produces at fixed input must be either transient or periodic. To look for both we integrated the network forward at the same parameter values (burial feedbacks 0.10 and 0.10, reductant input 2.505×10^{13} mol O_2-equivalent per year) from 101 initial conditions of three kinds. They comprise the published present-day state; perturbations of the anoxic steady state that raise atmospheric oxygen by one to four decades (factors of ten) and deep-ocean oxygen by two to eight decades, singly and jointly; and a one-at-a-time grid over six reservoirs starting from both of those states,

with the 14 starts that fell outside B moved to its edge. Each was integrated for 10^8 yr, about thirteen times as long as weathering would take to remove the oxygen now in the atmosphere, with two stiff integrators (a variable-order multistep method and an implicit Runge–Kutta method) at two tolerances each, and three of these integrations were continued to 10^9 yr, for 407 integrations in all. We counted as a step a rise of at least one decade in atmospheric oxygen between plateaus each held for at least ten times the rise time, provided both integrators at both tolerances reproduced it, and as an oscillation three successive maxima separated by at least half a decade. No integration produced a step or an oscillation. Every trajectory under the sigmoid closures ended on the anoxic steady state of Table S31, and every trajectory under the constant closure left the region through the oxygen floor, consistent with the absence of any steady state in the region under that closure. On the most extreme start, deep-ocean phosphorus a thousand times its present value, nine of the fourteen reservoirs passed transiently through negative values, identically under both integrators, so the solution left the physical domain of the equations on that trajectory, which likewise produced no step or oscillation.

The forward integrations hold the reductant input constant. We also drove the network with the time-varying forcing of Alcott et al. (2019) themselves, the linear decline of reductant input of their Fig. 5A over four billion years, at three settings: the burial feedbacks of that figure (0.50 and 0.25, no scavenging), the 0.10 and 0.10 of the enumeration, and the stronger feedbacks with phosphorus scavenging of their Fig. 5C. At every setting the atmosphere oxygenates once, with no later atmospheric step by the plateau criterion above; the date of that oxygenation lies between 3.39 and 1.30 Ga across the settings and closures, and in all of these integrations the atmosphere remains oxic after that date. The time-dependent solution in their Fig. 5 shows the same single atmospheric oxidation, as does a later version of the model driven by declining reductant input, in which oxygen "rises to a new stable level without any subsequent decline" (Dodd et al., 2025). The later steps that Alcott et al. (2019) show in that figure are transitions of the ocean compartments, which our integration of the 2019 network at the parameters of their Fig. 5A reproduces as repeated deep-ocean redox cycles under an atmosphere that stays oxic. In this network, as its authors state, the steps are the response to a declining reductant input; under that input the atmosphere oxygenates once, at 2.39 Ga with the parameters of their Fig. 5A (sigmoid closure B), and does not return to anoxia.

Alcott et al. (2026) have since driven a later version of the network, with a sulfur reservoir added, through the last two Paleoproterozoic glaciations with imposed post-glacial pulses of nutrient and reduced gas, and obtained an oscillatory oxygenation entangled with the glaciations. In their words, "our model results suggest that a delayed pulse of reduced gases would have been able to briefly return the atmosphere to anoxia." Applying the same enumeration to that 2026 network, we find no stable oxygenated state at the parameter values from which its published integration starts, as we found for the 2019 network. At the transient peak of its imposed nutrient pulse the 2026 network has a stable oxygenated state where the 2019 network at the same values does not. At the reductant input of 10^{13} mol O_2-equivalent per year at which Alcott et al. (2019) report a limit cycle (their Fig. 4A), the steady states under sigmoid closure B, the closure used in the 2026 code, depend on the burial-feedback parameters. With burial feedbacks of 0.10 and 0.10 the 2019 network has one stable oxygenated state and the 2026 network has no stable steady state; with the 0.50 and 0.25 of their Figs. 4A and 5A neither network has a stable steady state, consistent with the oscillation they report (Table S32). Because the forced 2026 model takes the pulse-peak parameter values only briefly, the existence of an oxygenated steady state at those values does not by itself imply that the forced trajectory reaches it.

S7.3 Goldblatt, Lenton and Watson (2006)

The proposal that atmospheric oxygen has two stable states originates with the three-reservoir model of atmospheric oxygen, methane and crustal organic carbon of Goldblatt et al. (2006), who argued that, once oxygenic photosynthesis existed, a low-oxygen steady state and a high-oxygen one shielded by ozone were stable simultaneously, with an unstable steady state between them. We treated this model in the same way as the fourteen-reservoir network. We took its equations and constants from Goldblatt et al. (2006) and their supplementary information (one rate constant that they do not print as a number cancels from the steady-state equations). The search region in atmospheric oxygen, 10^8 to 10^{20} mol, is the range over which they state their photochemical parameterization to be valid. At steady state the methane and crustal-carbon balances fix those two reservoirs in terms of oxygen, so the system reduces exactly to one scalar equation in oxygen. The interval method encloses the roots of that equation, and their stability follows from the full three-dimensional Jacobian. We solved the model at three published parameter points: the bistable case that the authors later drew as a phase portrait (Goldblatt et al., 2009), with reductant input $r = 5.3544 \times 10^{11}$ mol O_2-equivalent per year; the reductant input before the transition in their Fig. 3a, $r = 3 \times 10^{11}$; and its present-day value, $r = 7.5 \times 10^{10}$.

Applying the same method to the earlier Goldblatt, Lenton, and Watson two-state model from 2006, we

Table S33: The complete set of steady states of the Goldblatt et al. (2006) model at its three published reductant inputs r, inside the region $O \in [10^8, 10^{20}]$ mol set by the model's own photochemical parameterization. The two published stable states and the intervening saddle are recovered in the bistable case; at the other two inputs the region contains one stable, high-oxygen state. For each entry the interval method proves that no other root lies in the region.

parameter point	r (mol O_2-eq yr^{-1})	steady states in region	stable	$\log_{10} O$ (mol) of the states
bistable case (Goldblatt et al., 2009)	5.3544×10^{11}	three	two	13.738 (stable), 15.573 (saddle), 18.631 (stable)
pre-transition input (Fig. 3a)	3×10^{11}	one	one	18.797 (high branch)
present day	7.5×10^{10}	one	one	19.112 (high branch)

find that what those authors said happens actually happens. In the bistable case the region contains three steady states, of which two are stable: a low-oxygen state at 5.4666×10^{13} mol of O_2 (about 3.1×10^{-7} atm) and a high-oxygen state at 4.2805×10^{18} mol (about 2.4×10^{-2} atm), with an unstable saddle between them at 3.7385×10^{15} mol (Table S33), the structure those authors published. At the pre-transition input of their Fig. 3a the equations, in our implementation, have one steady state in the region, which is stable and lies on the high-oxygen branch. The region contains no low-oxygen state at this input, although that figure shows one; in a floating-point scan over r (without interval bounds, and therefore indicative only) the lower edge of the bistable range lies near 3.3×10^{11}, just above that input. At the present-day input the region again contains one stable state, on the high-oxygen branch, as Goldblatt et al. (2006) state for that input. The independent implementation and the restart test were repeated for this model with the same outcome.

S7.4 Scope of these results and the literature

The results above concern the equations of the two models as published, at their authors' parameter values and inside the search region of reservoir values defined for each model. For the fourteen-reservoir network that region contains the neighborhood of the modern oxygenated ocean and atmosphere, and, apart from the tenfold widening of its bounds on the thirteen reservoirs other than atmospheric oxygen, we did not search outside it. The enumeration is restricted to steady states. Its result, that the region contains no oxygenated stable state at these values, means that at fixed forcing the network cannot remain in an oxygenated state there; it does not exclude periodic solutions, in which the atmosphere could return to anoxia repeatedly without any second stable state, and Alcott et al. (2019) report one at a similar reductant input for larger burial-feedback parameters than we solved in the Great Oxidation range (their Fig. 4B). A unique steady state at each fixed forcing is compatible with steps under a moving forcing, which is the mechanism those authors propose and which we examined by integrating the network under their declining reductant input. The forward integrations are ordinary floating-point computations, checked by agreement between two stiff integrators at two tolerances, without interval bounds. We solved the 2019 network with burial feedbacks of 0.10 and 0.10 at the midpoint and both ends of its Great Oxidation range of reductant input and at the lower input of Table S32, with the feedbacks 0.50 and 0.25 of their Figs. 4A and 5A at that lower input only, and at the settings at which we compared it with the 2026 network. We integrated the 2019 network in time under their forcing at both feedback settings and at that of their Fig. 5C, and solved the 2006 model at three points. These results do not extend to other parameter values of either model. In particular, they do not bear on the conclusions either group of authors drew beyond the behavior of their equations at those values. The Neoproterozoic oscillatory regimes that Li et al. (2026) examined in related networks, for example, occur at parameter values outside those solved here.

Neither model, however, produces the repeated loss and return of the sulfur-isotope signal through the Great Oxidation: under its authors' declining reductant input the first oxygenates the atmosphere once and permanently, and the second supplies two states and needs a driver the field has yet to identify. In our model that driver is the decline of volcanic outgassing acting through the climate. In July 2026 we searched the literature that cites Alcott et al. (2019), the COPSE model (Lenton et al., 2018) and Goldblatt et al. (2006) in two citation indexes, together with the main preprint servers. We found no work that enumerates, completely or heuristically, the stable steady states of the 2019 network, or those of COPSE under any of its boundary conditions, or that tests whether oxygenation is inevitable in either model. The study of Alcott et al. (2026) appeared after that search and is discussed above with the forward integrations. Excitable-dynamics studies of related networks (Daines and Li, 2024; Li et al., 2025, 2026; Sheng et al., 2026) treat individual oxygenation events as limit-cycle or instability episodes and concentrate on the dynamics of each event rather than on

the set of steady states. Chemical reaction network theory has been applied to Anthropocene carbon-cycle box models to obtain existence conditions for multiple steady states (Alamin et al., 2025); those models have no oxygen reservoir and use modern boundary conditions. A stochastic one-variable balance for atmospheric oxygen has "only three stable states", the zero crossings of a single function (Fakhraee and Planavsky, 2024); the multi-dimensional networks are cited there but not analyzed. The question of multiple stable oxygen states was posed by Goldblatt et al. (2006); our contribution is the complete enumeration, with interval bounds, of the steady states of the fourteen-reservoir network at its published parameter values.

S7.5 Lineages of the models compared

The models discussed in the main text and here belong, by their authors' own descriptions, to a small number of lineages. The one-dimensional photochemistry behind the Archean oxygen and methane estimates of Kasting and Ji (2025) derives from earlier calculations by Kasting and co-workers (Pavlov et al., 2001; Kharecha et al., 2005), and the sulfur-isotope constraint of Pavlov and Kasting (2002) was computed with a photochemical model adapted from an earlier model of the same group. The photochemical model of Zahnle et al. (2006) is described by its authors as an updated version of the one-dimensional code of Kasting and co-workers, and Claire et al. (2006) used that model to compute the $k_{\mathrm{eff}}(p_{\mathrm{O_2}}, p_{\mathrm{CH_4}})$ surface that enters their biogeochemical model. The carbon-cycle inversion of Krissansen-Totton et al. (2021) is a modified version of the carbonate–silicate model of Krissansen-Totton and Catling (2017). Daines and Lenton (2016) coupled their ocean box model to the atmospheric redox model of Goldblatt et al. (2006). The 2019 network is built, in its authors' description, on earlier marine phosphorus models with equations added from COPSE (Lenton et al., 2018), and the sulfur cycle of its 2026 version (Alcott et al., 2026) is based on the single-box COPSE framework. Laakso and Schrag (2014) built their own ocean–atmosphere electron-cycling model, and the three-state theory of Laakso and Schrag (2017) computes its atmospheric hydrogen and methane chemistry, following Goldblatt et al. (2006), with the photochemical results of Pavlov and Kasting (2002). Across lineages, Kasting (2013) adopted the redox-budget parameter of Claire et al. (2006), and Kasting and Ji (2025) argue for their mid-Proterozoic oxygen level "following logic presented originally by" Daines et al. (2017). The model of the main text draws on each of these lines without descending from one: its methane photochemistry is the k_{eff} surface and escape constant of Claire et al. (2006), its redox accounting the source-to-sink oxygen budget of the same paper, its carbon cycle the outgassing and seafloor-weathering laws of Krissansen-Totton et al. (2018) and Krissansen-Totton and Catling (2017), its organic burial the isotope mass balance of Krissansen-Totton et al. (2015), and its climate thresholds the radiative tables of Byrne and Goldblatt (2014) with the snowball entry and exit values of Voigt et al. (2011) and Abbot et al. (2012).

Published accounts of the Great Oxidation differ on the order of the first glaciation and the first oxic air. Zahnle et al. (2006) and Claire et al. (2006) put the methane collapse, and with it the ice, first, as does our model. Kopp et al. (2005), Kasting and Ji (2025) and Swain et al. (2024) put oxygen first, whereas Harada et al. (2015), Tajika and Harada (2017) ("Such an extremely large perturbation could have been caused only by the snowball Earth event"), Laakso and Schrag (2017) and the nominal case of Goldblatt et al. (2026) make deglaciation the trigger. Mechanisms proposed for a glacial trigger include cold that "favors the oxygenation" (Jaziri et al., 2022), deglacial phosphorus pulses (Harada et al., 2015; Alcott et al., 2026) and glacial hydrogen peroxide (Kirschvink and Kopp, 2008). Our model contains none of these, and its atmospheric oxygen first passes the sulfur-isotope threshold after the second deglaciation only because the methane collapse precedes the epoch at which the oxygen source overtakes the sinks. A repeated rise and fall of atmospheric oxygen has been obtained in earlier models by imposed pulsed reductant forcing (Daines and Lenton, 2016, Fig. 6), by a parameterized ice–CO_2 switch its authors described as too simple to be predictive (Claire et al., 2006, Sect. 7.3), by orbital variation of the methane flux (Wogan et al., 2022), by prescribed glacial temperature swings (Garduno Ruiz et al., 2024), and by post-glacial nutrient and degassing pulses (Alcott et al., 2026). Repeated glaciation also occurs without any oxygen chemistry, in the outgassing-limited climate limit cycles whose period is set by the outgassing rate (Tajika, 2007; Mills et al., 2011; Kadoya and Tajika, 2014; Menou, 2015; Haqq-Misra et al., 2016); the glacial cycle of our model is a limit cycle of this kind.

S8 Paleosol CO_2 barometry for Ville Marie and Hokkalampi

The model predicts a definite range of atmospheric carbon dioxide for the ice-free intervals of its glacial era, and a weathering profile dated to one of those intervals, analyzed with either of the two paleosol CO_2 barometers in use (mass balance or porewater inversion), would test that prediction directly. Of the profiles analyzed here, the two from inside the glacial era have age constraints too broad to assign either to a single ice-free interval, so their CO_2 values do not yet provide that test. In multiples of the pre-industrial atmospheric level, the unit used for CO_2 throughout this Text, the model gives 253, 239 and 221 at one million years after the first, second and third deglaciations respectively. Carbon dioxide then falls to 65, 59 and 53 just before the next glaciation, and the medians over the three intervals are 86, 77 and 65. Under the current age assignments of the dated profiles, no published CO_2 estimate from either barometer comes from a profile lying between the first and the last glaciation. We describe here the dated weathering profiles of the glacial era, our implementation and calibration of the two barometers, the CO_2 values they give for the two profiles inside the era with complete published chemistry, Ville Marie in Quebec and Hokkalampi in Finland, and the measurements still needed for these values to test the model.

S8.1 Dated weathering profiles across the glacial era

Published paleosol CO_2 estimates for the early Paleoproterozoic come from profiles dated either just before the model's first glaciation or after its last, and from two schools of barometry (Table S34). At the older end, the porewater-inversion school (Kanzaki and Murakami, 2015) gives 160–490 times pre-industrial for the Pronto and related profiles beneath the basal Huronian volcanic rocks of Ontario, between about 2.475 and 2.44 Ga. The lower ends of that school's ranges rest on the requirement that liquid water was present for aqueous weathering and not on a radiative constraint. At the younger end, the mass-balance school (Sheldon, 2006) gives 7.67–69 times pre-industrial for three paleosols of about 2.25–2.15 Ga, the Hekpoort paleosol of the Transvaal among them (Rye and Holland, 2000). The inversion values at the older end thus exceed the mass-balance values at the younger end by about an order of magnitude. Between those ends, from 2.44 to 2.25 Ga, we reviewed every weathering profile with a published age assignment and found that all of them lacked a published CO_2 estimate. Two profiles in that interval with major-element chemistry complete enough for barometry had nevertheless been described, Ville Marie (Panahi et al., 2000) and Hokkalampi (Marmo, 1992), and neither school had analyzed them under their current age assignments.

The Ville Marie paleosol developed on Archean granite and is buried by the basal Lorrain Formation of the upper Huronian Supergroup; it has no direct radiometric age (its Rb–Sr system was reset long after burial), and its stratigraphic bracket under the current age assignment is 2.38–2.31 Ga. Panahi et al. (2000) measured two sections, a primary one and a more deeply eroded one, together with the fresh granite parent. The mass-balance school cites the profile and may have included it among its younger-end paleosols under an older correlation, so a mass-balance value for Ville Marie, assigned to that younger group, may already form part of that school's published range; the value we give is computed under the current age assignment. The Hokkalampi paleosol of eastern Finland developed on two parent rocks (Archean granitoid and a Paleoproterozoic glaciogenic deposit), is bracketed between 2.43 and 2.20 Ga with no direct date, and carries a later greenschist-facies metamorphic overprint (Marmo, 1992). Two further profiles serve to calibrate our implementations at the older and younger ends of the era. The Cooper Lake profile of Ontario, developed on mafic volcanic rocks (Utsunomiya et al., 2003), lies at the older edge of the glacial era (∼2.45 Ga) and has been analyzed by the inversion school. The Strata 1 drill core near Gaborone is the one section of the Hekpoort paleosol that preserves the top of the profile (Yang and Holland, 2003); its age assignment (2.24 to 2.06 Ga, after the model's last glaciation) places it at the younger end.

S8.2 Implementation and calibration of the two barometers

We applied both barometers to the published element-loss tables of each profile. The sections, parent rocks, excluded samples, age brackets and temperatures to be used were chosen for every profile before any CO_2 value was computed and kept fixed thereafter, to prevent any of these choices from being adjusted toward the model. The mass-balance barometer (Sheldon, 2006) equates the CO_2 consumed by silicate weathering over the life of the soil, obtained by integrating the loss of base cations down the profile against an immobile element, with the CO_2 delivered to the soil from the atmosphere over the same time. The atmospheric level then follows once a formation time for the soil is assumed, and it scales inversely with that time. To calibrate our implementation against the mass-balance school's own result we tested it on the Hekpoort paleosol (Rye and Holland, 2000), the one profile both schools have analyzed; it yields 24.1 times pre-industrial against that school's published 23 with its factor-of-three band (Sheldon, 2006), a ratio of 1.05. The porewater inversion (Kanzaki and Murakami, 2015) needs no formation time, because it reconstructs the steady-state

Table S34: Weathering profiles with published age assignments across the model's glacial era, the parent rock, the age bracket, and which barometer school has published a CO_2 value for each. Only the profiles at the two ends of the era have published values; Ville Marie and Hokkalampi, the two profiles inside it with complete chemistry, have none. Ages are stratigraphic brackets except where a school's own age bin is given; neither Ville Marie nor Hokkalampi has a direct radiometric date.

profile (region)	parent rock	age (Ga)	published CO_2 value (× pre-industrial)	chemistry
Pronto and related (Ontario)	Archean granite, greenstone	2.475–2.44	160–490, inversion school	Kanzaki and Murakami (2015)
Cooper Lake (Ontario), edge	mafic volcanic rocks	∼2.45	inversion school (temperature-limited)	Utsunomiya et al. (2003)
Ville Marie (Quebec), inside the era	Archean granite	2.38–2.31	none	Panahi et al. (2000)
Hokkalampi (Finland), inside the era	granitoid; glaciogenic deposit	2.43–2.20	none	Marmo (1992)
Hekpoort (Transvaal), younger end	basaltic andesite	2.25–2.15	7.67–69, mass-balance school	Rye and Holland (2000); Sheldon (2006)
Strata 1, Hekpoort (Gaborone)	basalt	2.24–2.06	30–100, profile authors	Yang and Holland (2003)

composition of the soil water (pH, dissolved silica and cations) that is consistent with the measured ratios of element loss in the profile at an assumed temperature, and solves for the CO_2 pressure in equilibrium with that water. We evaluate the inversion at each temperature the school tabulates and take the result at its reference temperature as the central value. On the inversion school's own profiles our implementation reproduces their published values at all of these temperatures, for example 318 to 829 times pre-industrial at the Pronto profile, where they obtained 320 to 820, and likewise for Cooper Lake and Gaborone.

Two choices in the implementation affect the Ville Marie and Hokkalampi estimates. First, the inversion takes its potassium budget from the school's rule for felsic parent rocks instead of the potassium measured in the profile, which makes its result nearly independent of whether that potassium is pedogenic or was added after burial. Treating the measured potassium as a later addition moves the CO_2 bands downward by only 0.2 to 10.2 percent and leaves every comparison with the model unchanged. Second, the two Ville Marie sections differ in measured sodium mobility (0.91 and 0.60) and are analyzed separately, never averaged; for each barometer we give a central value and a band per profile and per section. At Hokkalampi the two parent rocks are likewise kept separate, and we treat disagreement between the estimates from the two parents beyond their bands as evidence that the metamorphic overprint has compromised the barometry.

S8.3 CO_2 estimates for the interior and edge profiles

Applied to Ville Marie, the mass-balance barometer as calibrated on the Hekpoort paleosol gives 8.5 times pre-industrial inside a band of 1.3 to 67 on the primary section, and a higher central value on the eroded one. Cooper Lake, at the older edge, gives 24.3 inside 3.8 to 192 by mass balance. The inversion school has also analyzed Cooper Lake, and there the two barometers differ by a factor of about 12, the same order-of-magnitude offset that separates the two schools' published estimates at the two ends of the era. When values from the two schools are combined into one CO_2 history, they may differ by about this factor for reasons of method alone. By the porewater inversion, Ville Marie gives 55 times pre-industrial inside a band of 15.5 to 198 on its primary section and 17 inside a band of 3.8 to 79 on the eroded one. Our implementation of the inversion gives 513 (inside 318 to 829) for Pronto at the older edge and 42 (inside 3.2 to 564) for the Strata 1 core of the Hekpoort paleosol at the younger end, for which Yang and Holland (2003) themselves estimate 30 to 100 times pre-industrial. For Ville Marie the two barometers therefore agree more closely, mass balance giving 8.5 to 19.6 for the two sections and the inversion giving central values of 17 to 55, whereas at the older edge the order-of-magnitude offset between them remains.

At Hokkalampi we ran the inversion on both parent rocks. For the glaciogenic parent and the full column at the type locality the inversion gives 9 times pre-industrial inside a band of 0.9 to 82, and for the granitoid parent and the truncated drill core as recovered it gives 15 inside 1.2 to 191. The two estimates agree within their bands; the metamorphic overprint has therefore not detectably compromised the barometry, and we retain both. For a third case, a full column assembled on the granitoid parent, the inversion fails, because no self-consistent porewater composition exists for that column at any tabulated temperature. Hokkalampi is more deeply weathered than any profile in the inversion school's own set, and this greater maturity probably biases both estimates low; the two values are uncorrected for this bias. We give no mass-balance value for Hokkalampi, because the depth and assumed duration of the full column inflate the estimate, the truncated

Table S35: Paleosol CO_2 values computed here (upper block: the five central values, by profile, section or parent, and barometer) together with the model's interglacial range and the published values at the two ends of the era (lower block), in multiples of the pre-industrial level. Every band computed for Ville Marie and Hokkalampi overlaps the model's ice-free range of 53–253; four of the five central values lie below the model's interglacial minimum of 53 and one lies inside the range. Neither profile is yet dated to an interglacial, which a test of the model requires, and the mass-balance values assume a formation time. Sections and parents are separate branches and are not averaged.

profile	branch	barometer	central (× pre-industrial)	band (× pre-industrial)	against the model's range
Ville Marie	primary section	mass balance	8.5	1.3–67	below
Ville Marie	primary section (Na mobility 0.91)	porewater inversion	55	15.5–198	inside
Ville Marie	eroded section (Na mobility 0.60)	porewater inversion	17	3.8–79	below
Hokkalampi	glaciogenic parent, full column	porewater inversion	9	0.9–82	below
Hokkalampi	granitoid parent, core as drilled	porewater inversion	15	1.2–191	below
model, ice-free intervals 2.43–2.24 Ga	minimum to one Myr after a thaw		medians 65–86	53–253	
Pronto (older edge)	reference temperature	porewater inversion	513	318–829	published 160–490
Cooper Lake (older edge)		mass balance	24.3	3.8–192	
Hekpoort (younger end)	calibration	mass balance	24.1	factor of three	published 23
Strata 1, Hekpoort		porewater inversion	42	3.2–564	profile authors 30–100
Neoarchean profiles 2.70–2.68 Ga		mass balance		10–50	Driese et al. (2011)

core biases it low, and the mass-balance school has published no profile this deeply weathered against which to calibrate. Because Marmo (1992) reports the Hokkalampi data as per-zone average chemistries rather than depth series, the element-loss integrals down the profile are computed from zone means, which at the rounding used here leaves the bands unchanged. In Fig. S11 both Hokkalampi values are plotted across the whole stratigraphic bracket of the profile, which still lacks a direct age.

S8.4 Comparison with the model and proposed tests

The model's CO_2 in the ice-free intervals between 2.43 and 2.24 Ga spans 53 to 253 times pre-industrial, from the minimum before a glaciation to one million years after a deglaciation, with interval medians of 65 to 86 (Table S35, Fig. S11). Every barometer band computed for Ville Marie and Hokkalampi overlaps that range. Of the five central values, four (the mass-balance value and the eroded-section inversion value at Ville Marie, and both Hokkalampi values) lie below the model's interglacial minimum and one, the inversion value on the Ville Marie primary section, lies inside the range. In the alternative storage case of Table 3 of the main text, in which the sub-ice carbon stays in the ocean crust and only the airborne excess returns at each thaw, the model's ice-free CO_2 spans 56 to 114 times pre-industrial at the middle of the four-glaciation interval of ν for that case (Supplementary Text S1; Table S5c), and every barometer band also overlaps this narrower range. We draw no conclusion from this comparison yet, for three reasons. First, neither profile is dated to an interglacial rather than to a glaciation or its aftermath. Second, the mass-balance values assume a soil formation time, which the length of the model's ice-free intervals, 43.4 to 48.8 Myr, does not constrain. Third, the comparison was not among those fixed before the integrations reported in the main text. The Ville Marie and Hokkalampi values therefore do not yet discriminate for or against the model: their bands overlap its interglacial range, and four of their five central values, taken at face value, favor lower CO_2 than that range, although both Hokkalampi estimates are probably biased low by that profile's maturity (Section S8.3).

A direct age on either profile precise enough to place it inside one ice-free interval of the model would turn the comparison into a test, and the mass-balance barometer would also have to be reapplied to the same published element-loss tables with a formation time estimated for each profile. Chemical-abrasion U–Pb dating of the units that bracket Ville Marie and Hokkalampi could narrow the age range of either profile to a few tens of millions of years. The glacial era is most sparsely sampled by weathering profiles between 2.32 and 2.25 Ga, and one new major-element profile of that age, complete enough for barometry and analyzed together with its parent rock, would add a CO_2 estimate to the compilation of Fig. S11. Candidate surfaces

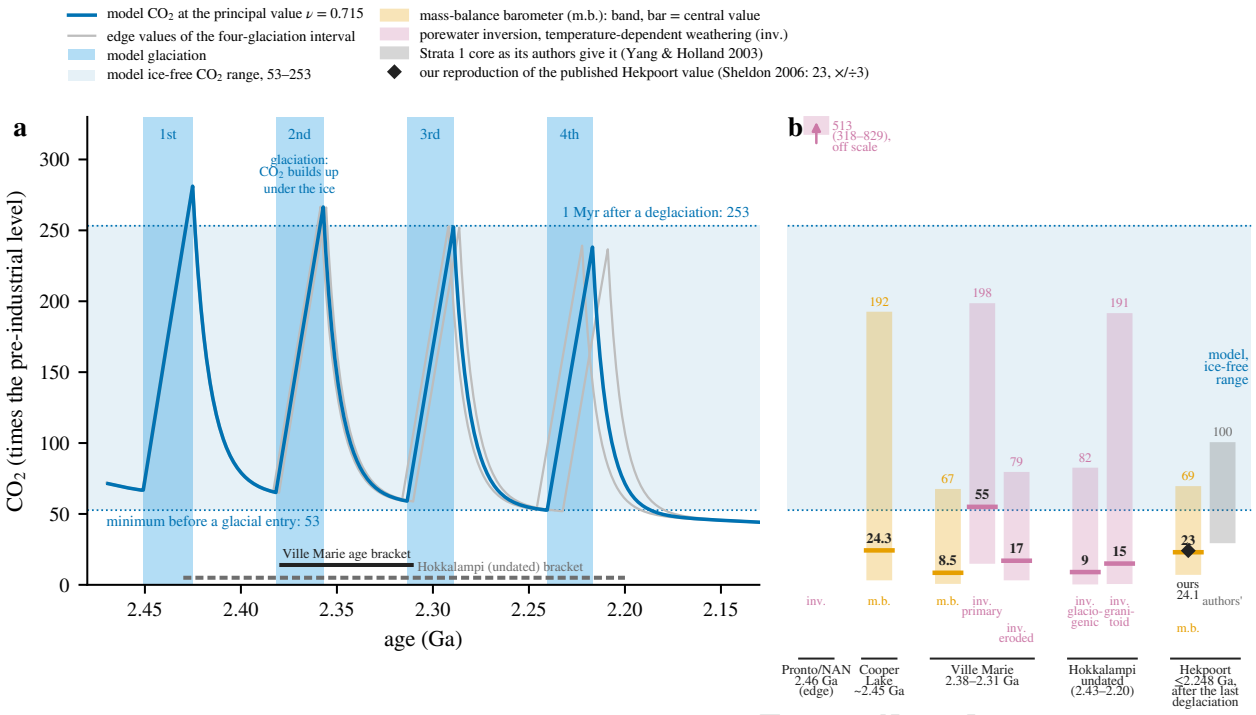

Figure S11: Paleosol CO_2 estimates for the Ville Marie and Hokkalampi profiles, both from within the glacial era, compared with the model's CO_2 between glaciations. (a) Model CO_2 (multiples of pre-industrial) at $\nu = 0.715$ and, in gray, at the two ends of the four-glaciation ν interval. CO_2 is 238–281 just after each thaw and is drawn down to within 53–253 while ice-free. (b) Estimates on the same axis: Ville Marie by the mass-balance barometer and by the porewater inversion of the temperature-dependent-weathering school, its two sections kept separate, and Hokkalampi by the inversion for two candidate parent rocks. Also shown are two profiles from the beginning of the glacial era (Cooper Lake; Pronto/NAN by the inversion, off scale) and the Hekpoort paleosol from after the last thaw. For Hekpoort we plot the published value (Sheldon, 2006), our reproduction of it and the Strata 1 core as given by Yang and Holland (2003). The Ville Marie and Hokkalampi bands overlap the model's ice-free range, with most central values below it, and the comparison would test the model if either profile were dated to a specific ice-free interval. Sources, age brackets and values are listed in Tables S34 and S35.

exist in the oxidized weathering horizons reported above the deposits of the third Paleoproterozoic glaciation (Rasmussen et al., 2013), the disconformities at the bases of the Hekpoort and Daspoort formations (Schröder et al., 2016), and the Turee Creek Group of Western Australia, for which a chronology has been published (Caquineau et al., 2018). A well-dated interglacial value below about half the model's minimum, or above its post-glacial maximum, would count against the model's carbon cycle. Four of the five central values computed here lie below half that minimum, but none can be used in this way until its profile has a direct age placing it in an ice-free interval and, for the mass-balance value, an estimate of the formation time.

References

D. S. Abbot, A. Voigt, M. Branson, R. T. Pierrehumbert, D. Pollard, G. Le Hir, and D. D. B. Koll. Clouds and Snowball Earth deglaciation. *Geophysical Research Letters*, 39(20):L20711, 2012. doi: 10.1029/2012GL052861.

A. J. L. J. Alamin, M. J. T. Cruz, B. S. Hernandez, and E. R. Mendoza. The long-term impact of direct capture approaches to carbon dioxide removal. arXiv:2510.20593 [math.DS], 2025. Preprint.

L. J. Alcott, B. J. W. Mills, and S. W. Poulton. Stepwise Earth oxygenation is an inherent property of global biogeochemical cycling. *Science*, 366(6471):1333–1337, 2019. doi: 10.1126/science.aax6459.

L. J. Alcott, B. J. W. Mills, A. Bekker, Z. Peng, and S. W. Poulton. A nutrient control on oxygenation dynamics during Earth's Great Oxidation Episode. *Nature Communications*, 2026. doi: 10.1038/s41467-026-76597-y. published online 27 August 2026.

T. J. Algeo and E. Ingall. Sedimentary C_{org}:P ratios, paleocean ventilation, and Phanerozoic atmospheric pO_2. *Palaeogeography, Palaeoclimatology, Palaeoecology*, 256(3-4):130–155, 2007. doi: 10.1016/j.palaeo.2007.02.029.

W. Altermann. Hekpoort Formation, South Africa, ca. 2.223 Ma (February 2019 LIP of the Month). Large Igneous Provinces Commission, http://www.largeigneousprovinces.org/19feb, 2019. accessed 11 September 2026.

A. D. Anbar, Y. Duan, T. W. Lyons, G. L. Arnold, B. Kendall, R. A. Creaser, A. J. Kaufman, G. W. Gordon, C. Scott, J. Garvin, and R. Buick. A whiff of oxygen before the Great Oxidation Event? *Science*, 317:1903–1906, 2007. doi: 10.1126/science.1140325.

A. D. Anbar, R. Buick, G. W. Gordon, A. C. Johnson, B. Kendall, T. W. Lyons, C. M. Ostrander, N. J. Planavsky, C. T. Reinhard, and E. E. Stüeken. Technical comment on "Reexamination of 2.5-Ga 'whiff' of oxygen interval points to anoxic ocean before GOE". *Science Advances*, 9(14):eabq3736, 2023. doi: 10.1126/sciadv.abq3736.

G. Avice, B. Marty, and R. Burgess. The origin and degassing history of the Earth's atmosphere revealed by Archean xenon. *Nature Communications*, 8:15455, 2017. doi: 10.1038/ncomms15455.

G. Avice, B. Marty, R. Burgess, A. Hofmann, P. Philippot, K. Zahnle, and D. Zakharov. Evolution of atmospheric xenon and other noble gases inferred from Archean to Paleoproterozoic rocks. *Geochimica et Cosmochimica Acta*, 232:82–100, 2018. doi: 10.1016/j.gca.2018.04.018.

A. Bekker and H. D. Holland. Oxygen overshoot and recovery during the early Paleoproterozoic. *Earth and Planetary Science Letters*, 317-318:295–304, 2012. doi: 10.1016/j.epsl.2011.12.012.

A. Bekker and A. J. Kaufman. Oxidative forcing of global climate change: A biogeochemical record across the oldest Paleoproterozoic ice age in North America. *Earth and Planetary Science Letters*, 258(3-4):486–499, 2007. doi: 10.1016/j.epsl.2007.04.009.

A. Bekker, H. D. Holland, P.-L. Wang, D. Rumble III, H. J. Stein, J. L. Hannah, L. L. Coetzee, and N. J. Beukes. Dating the rise of atmospheric oxygen. *Nature*, 427:117–120, 2004. doi: 10.1038/nature02260.

C. M. Belcher and J. C. McElwain. Limits for combustion in low O_2 redefine paleoatmospheric predictions for the Mesozoic. *Science*, 321:1197–1200, 2008. doi: 10.1126/science.1160978.

R. A. Berner and Z. Kothavala. GEOCARB III: A revised model of atmospheric CO_2 over Phanerozoic time. *American Journal of Science*, 301:182–204, 2001. doi: 10.2475/ajs.301.2.182.

N. J. Beukes and S. Schröder. Sedimentary and stratigraphic architecture of the Duitschland and Rooihoogte formations (Palaeoproterozoic, South Africa): implications for tempo of the Great Oxidation Event. *South African Journal of Geology*, 127(2):433–454, 2024. doi: 10.25131/sajg.127.0006.

I. N. Bindeman, D. O. Zakharov, J. Palandri, N. D. Greber, N. Dauphas, G. J. Retallack, A. Hofmann, J. S. Lackey, and A. Bekker. Rapid emergence of subaerial landmasses and onset of a modern hydrologic cycle 2.5 billion years ago. *Nature*, 557:545–548, 2018. doi: 10.1038/s41586-018-0131-1.

C. L. Blättler, M. W. Claire, A. R. Prave, K. Kirsimäe, J. A. Higgins, P. V. Medvedev, A. E. Romashkin, D. V. Rychanchik, A. L. Zerkle, K. Paiste, T. Kreitsmann, I. L. Millar, J. A. Hayles, H. Bao, A. V. Turchyn, M. R. Warke, and A. Lepland. Two-billion-year-old evaporites capture Earth's great oxidation. *Science*, 360:320–323, 2018. doi: 10.1126/science.aar2687.

A. T. Brasier, A. P. Martin, V. A. Melezhik, A. R. Prave, D. J. Condon, and A. E. Fallick. Earth's earliest global glaciation? Carbonate geochemistry and geochronology of the Polisarka Sedimentary Formation, Kola Peninsula, Russia. *Precambrian Research*, 235:278–294, 2013. doi: 10.1016/j.precamres.2013.06.007.

A. R. Brenner, R. R. Fu, A. R. C. Kylander-Clark, G. J. Hudak, and B. J. Foley. Plate motion and a dipolar geomagnetic field at 3.25 Ga. *Proceedings of the National Academy of Sciences*, 119(44):e2210258119, 2022. doi: 10.1073/pnas.2210258119.

J. J. Brocks, A. J. M. Jarrett, E. Sirantoine, C. Hallmann, Y. Hoshino, and T. Liyanage. The rise of algae in Cryogenian oceans and the emergence of animals. *Nature*, 548:578–581, 2017. doi: 10.1038/nature23457.

D. J. Burdige. Burial of terrestrial organic matter in marine sediments: A re-assessment. *Global Biogeochemical Cycles*, 19(4):GB4011, 2005. doi: 10.1029/2004GB002368.

B. Byrne and C. Goldblatt. Radiative forcings for 28 potential Archean greenhouse gases. *Climate of the Past*, 10(5):1779–1801, 2014. doi: 10.5194/cp-10-1779-2014.

D. E. Canfield. The evolution of the Earth surface sulfur reservoir. *American Journal of Science*, 304(10): 839–861, 2004. doi: 10.2475/ajs.304.10.839.

T. Caquineau, J.-L. Paquette, and P. Philippot. U-Pb detrital zircon geochronology of the Turee Creek Group, Hamersley Basin, Western Australia: timing and correlation of the Paleoproterozoic glaciations. *Precambrian Research*, 307:34–50, 2018. doi: 10.1016/j.precamres.2018.01.003.

D. C. Catling and K. J. Zahnle. The Archean atmosphere. *Science Advances*, 6:eaax1420, 2020. doi: 10.1126/sciadv.aax1420.

D. C. Catling, K. J. Zahnle, and C. P. McKay. Biogenic methane, hydrogen escape, and the irreversible oxidation of early Earth. *Science*, 293(5531):839–843, 2001. doi: 10.1126/science.1061976.

E. Chi Fru, N. P. Rodríguez, C. A. Partin, S. V. Lalonde, P. Andersson, D. J. Weiss, A. El Albani, I. Rodushkin, and K. O. Konhauser. Cu isotopes in marine black shales record the Great Oxidation Event. *Proceedings of the National Academy of Sciences*, 113(18):4941–4946, 2016. doi: 10.1073/pnas.1523544113.

M. W. Claire, D. C. Catling, and K. J. Zahnle. Biogeochemical modelling of the rise in atmospheric oxygen. *Geobiology*, 4(4):239–269, 2006. doi: 10.1111/j.1472-4669.2006.00084.x.

G. Colbourn, A. Ridgwell, and T. M. Lenton. The time scale of the silicate weathering negative feedback on atmospheric CO_2. *Global Biogeochemical Cycles*, 29(5):583–596, 2015. doi: 10.1002/2014GB005054.

K. C. Condie, C. O'Neill, and R. C. Aster. Evidence and implications for a widespread magmatic shutdown for 250 My on Earth. *Earth and Planetary Science Letters*, 282(1–4):294–298, 2009. doi: 10.1016/j.epsl.2009.03.033.

S. A. Crowe, G. Paris, S. Katsev, C. Jones, S.-T. Kim, A. L. Zerkle, S. Nomosatryo, D. A. Fowle, J. F. Adkins, A. L. Sessions, J. Farquhar, and D. E. Canfield. Sulfate was a trace constituent of Archean seawater. *Science*, 346:735–739, 2014. doi: 10.1126/science.1258966.

S. Daines and Z. Li. Excitable dynamics of Neoproterozoic to early Paleozoic atmospheric and ocean oxygen. EarthArXiv preprint, 2024.

S. J. Daines and T. M. Lenton. The effect of widespread early aerobic marine ecosystems on methane cycling and the Great Oxidation. *Earth and Planetary Science Letters*, 434:42–51, 2016. doi: 10.1016/j.epsl.2015.11.021.

S. J. Daines, B. J. W. Mills, and T. M. Lenton. Atmospheric oxygen regulation at low Proterozoic levels by incomplete oxidative weathering of sedimentary organic carbon. *Nature Communications*, 8:14379, 2017. doi: 10.1038/ncomms14379.

R. Dasgupta. Ingassing, storage, and outgassing of terrestrial carbon through geologic time. *Reviews in Mineralogy and Geochemistry*, 75(1):183–229, 2013. doi: 10.2138/rmg.2013.75.7.

M. S. Dodd, C. Li, H. Gu, Z. Zhang, M. Hou, A. Sadekov, C. A. Rosière, F. Pirajno, L. Alcott, F. O. Ossa, B. J. W. Mills, and A. Bekker. Marine phosphorus and atmospheric oxygen were coupled during the Great Oxidation Event. *Nature Communications*, 16:9151, 2025. doi: 10.1038/s41467-025-64194-4.

S. G. Driese, M. A. Jirsa, M. Ren, S. L. Brantley, N. D. Sheldon, D. Parker, and M. Schmitz. Neoarchean paleoweathering of tonalite and metabasalt: Implications for reconstructions of 2.69 Ga early terrestrial ecosystems and paleoatmospheric chemistry. *Precambrian Research*, 189(1-2):1–17, 2011. doi: 10.1016/j.precamres.2011.04.003.

A. Dutkiewicz, A. S. Merdith, A. S. Collins, B. Mather, L. Ilano, S. Zahirovic, and R. D. Müller. Duration of Sturtian "Snowball Earth" glaciation linked to exceptionally low mid-ocean ridge outgassing. *Geology*, 52(4):292–296, 2024. doi: 10.1130/G51669.1.

S. Edmonsond and B. Dyer. Timing and magnitude of the Lomagundi–Jatuli carbon isotope excursion. *Proceedings of the National Academy of Sciences*, 123(2):e2512767123, 2026. doi: 10.1073/pnas.2512767123.

J. Eguchi, J. Seales, and R. Dasgupta. Great Oxidation and Lomagundi events linked by deep cycling and enhanced degassing of carbon. *Nature Geoscience*, 13(1):71–76, 2020. doi: 10.1038/s41561-019-0492-6.

M. Eickhoff, M. Obst, C. Schröder, A. P. Hitchcock, T. Tyliszczak, R. E. Martinez, L. J. Robbins, K. O. Konhauser, and A. Kappler. Nickel partitioning in biogenic and abiogenic ferrihydrite: The influence of silica and implications for ancient environments. *Geochimica et Cosmochimica Acta*, 140:65–79, 2014. doi: 10.1016/j.gca.2014.05.021.

M. Fakhraee and N. Planavsky. Insights from a dynamical system approach into the history of atmospheric oxygenation. *Nature Communications*, 15:6794, 2024. doi: 10.1038/s41467-024-51042-0.

G. Feulner, M. Bukenberger, and S. Petri. Tracing the Snowball bifurcation of aquaplanets through time reveals a fundamental shift in critical-state dynamics. *Earth System Dynamics*, 14(3):533–547, 2023. doi: 10.5194/esd-14-533-2023.

G. P. Fournier, K. R. Moore, L. T. Rangel, J. G. Payette, L. Momper, and T. Bosak. The Archean origin of oxygenic photosynthesis and extant cyanobacterial lineages. *Proceedings of the Royal Society B*, 288: 20210675, 2021. doi: 10.1098/rspb.2021.0675.

S. Franck, A. Block, W. von Bloh, C. Bounama, H. J. Schellnhuber, and Y. Svirezhev. Reduction of biosphere life span as a consequence of geodynamics. *Tellus B*, 52(1):94–107, 2000. doi: 10.1034/j.1600-0889.2000.00898.x.

J. J. Fuentes, J. W. Crowley, R. Dasgupta, and J. X. Mitrovica. The influence of plate tectonic style on melt production and CO_2 outgassing flux at mid-ocean ridges. *Earth and Planetary Science Letters*, 511: 154–163, 2019. doi: 10.1016/j.epsl.2019.01.020.

J. Gaillardet, B. Dupré, P. Louvat, and C. J. Allègre. Global silicate weathering and CO_2 consumption rates deduced from the chemistry of large rivers. *Chemical Geology*, 159(1-4):3–30, 1999. doi: 10.1016/S0009-2541(99)00031-5.

D. Garduno Ruiz, C. Goldblatt, and A.-S. Ahm. Climate variability leads to multiple oxygenation episodes across the Great Oxidation Event. *Geophysical Research Letters*, 51(3):e2023GL106694, 2024. doi: 10.1029/2023GL106694.

C. Goldblatt, T. M. Lenton, and A. J. Watson. Bistability of atmospheric oxygen and the Great Oxidation. *Nature*, 443(7112):683–686, 2006. doi: 10.1038/nature05169.

C. Goldblatt, A. J. Watson, and T. M. Lenton. Bistability of atmospheric oxygen and the Great Oxidation: Implications for life detection. In K. J. Meech, J. V. Keane, M. J. Mumma, J. L. Siefert, and D. J. Werthimer, editors, *Bioastronomy 2007: Molecules, Microbes and Extraterrestrial Life*, volume 420 of *ASP Conference Series*, pages 277–285, 2009.

C. Goldblatt, J. K. Eager-Nash, and J. E. Horne. Evolution of the Archean atmosphere. In M. Homann, T. W. Lyons, R. E. Ernst, C. Heubeck, E. Stueeken, A. Webb, D. Papineau, R. Mazumder, P. R. D. Mason, and W. Altermann, editors, *The Archean Earth: Tempos and Events*, pages 333–344. Elsevier, second edition, 2026. ISBN 9780323955478. doi: 10.1016/B978-0-323-95547-8.00022-7.

D. O. Gough. Solar interior structure and luminosity variations. *Solar Physics*, 74:21–34, 1981. doi: 10.1007/BF00151270.

R. J. Graham and R. Pierrehumbert. Thermodynamic and energetic limits on continental silicate weathering strongly impact the climate and habitability of wet, rocky worlds. *The Astrophysical Journal*, 896:115, 2020. doi: 10.3847/1538-4357/ab9362.

B. S. Gregory, M. W. Claire, and S. Rugheimer. Photochemical modelling of atmospheric oxygen levels confirms two stable states. *Earth and Planetary Science Letters*, 561:116818, 2021. doi: 10.1016/j.epsl.2021.116818.

C. L. Grettenberger and D. Y. Sumner. Physiology, not nutrient availability, may have limited primary productivity after the emergence of oxygenic photosynthesis. *Geobiology*, 22(5):e12622, 2024. doi: 10.1111/gbi.12622.

A. P. Gumsley, K. R. Chamberlain, W. Bleeker, U. Söderlund, M. O. de Kock, E. R. Larsson, and A. Bekker. Timing and tempo of the Great Oxidation Event. *Proceedings of the National Academy of Sciences*, 114:1811–1816, 2017. doi: 10.1073/pnas.1608824114.

Q. Guo, H. Strauss, A. J. Kaufman, S. Schröder, J. Gutzmer, B. Wing, M. A. Baker, A. Bekker, Q. Jin, S.-T. Kim, and J. Farquhar. Reconstructing Earth's surface oxidation across the Archean-Proterozoic transition. *Geology*, 37(5):399–402, 2009. doi: 10.1130/G25423A.1.

J. L. Hannah, A. Bekker, H. J. Stein, R. J. Markey, and H. D. Holland. Primitive Os and 2316 Ma age for marine shale: implications for Paleoproterozoic glacial events and the rise of atmospheric oxygen. *Earth and Planetary Science Letters*, 225(1-2):43–52, 2004. doi: 10.1016/j.epsl.2004.06.013.

J. Haqq-Misra, R. K. Kopparapu, N. E. Batalha, C. E. Harman, and J. F. Kasting. Limit cycles can reduce the width of the habitable zone. *The Astrophysical Journal*, 827(2):120, 2016. doi: 10.3847/0004-637X/827/2/120.

J. D. Haqq-Misra, S. D. Domagal-Goldman, P. J. Kasting, and J. F. Kasting. A revised, hazy methane greenhouse for the Archean Earth. *Astrobiology*, 8(6):1127–1137, 2008. doi: 10.1089/ast.2007.0197.

M. Harada, E. Tajika, and Y. Sekine. Transition to an oxygen-rich atmosphere with an extensive overshoot triggered by the Paleoproterozoic snowball Earth. *Earth and Planetary Science Letters*, 419:178–186, 2015. doi: 10.1016/j.epsl.2015.03.005.

J. C. Havsteen, I. C. Kleinhanns, S. Schröder, B. Eickmann, G. Izon, M. D. Gogouvitis, R. Ngobeli, N. J. Beukes, and R. Schoenberg. Evidence for contemporaneous deposition of the Duitschland and Rooihoogte formations (Transvaal Supergroup): Implications for tempo and mode of Earth's Great Oxidation. *Precambrian Research*, 391:107055, 2023. doi: 10.1016/j.precamres.2023.107055.

J. M. Hayes and J. R. Waldbauer. The carbon cycle and associated redox processes through time. *Philosophical Transactions of the Royal Society B*, 361(1470):931–950, 2006. doi: 10.1098/rstb.2006.1840.

A. W. Heard, C. M. Ostrander, Y. Shu, A. Bekker, S. W. Poulton, and S. G. Nielsen. Onset of persistent surface ocean oxygenation during the Great Oxidation Event. *Nature Communications*, 16:10190, 2025. doi: 10.1038/s41467-025-66323-5.

C. Herzberg, K. Condie, and J. Korenaga. Thermal history of the Earth and its petrological expression. *Earth and Planetary Science Letters*, 292(1-2):79–88, 2010. doi: 10.1016/j.epsl.2010.01.022.

J. A. Higgins and D. P. Schrag. Aftermath of a snowball Earth. *Geochemistry, Geophysics, Geosystems*, 4(3):1028, 2003. doi: 10.1029/2002GC000403.

P. F. Hoffman. The Great Oxidation and a Siderian snowball Earth: MIF-S based correlation of Paleoproterozoic glacial epochs. *Chemical Geology*, 362:143–156, 2013. doi: 10.1016/j.chemgeo.2013.04.018.

P. F. Hoffman, D. S. Abbot, Y. Ashkenazy, D. I. Benn, J. J. Brocks, P. A. Cohen, G. M. Cox, J. R. Creveling, Y. Donnadieu, D. H. Erwin, I. J. Fairchild, D. Ferreira, J. C. Goodman, G. P. Halverson, M. F. Jansen, G. Le Hir, G. D. Love, F. A. Macdonald, A. C. Maloof, C. A. Partin, G. Ramstein, B. E. J. Rose, C. V. Rose, P. M. Sadler, E. Tziperman, A. Voigt, and S. G. Warren. Snowball Earth climate dynamics and Cryogenian geology-geobiology. *Science Advances*, 3:e1600983, 2017. doi: 10.1126/sciadv.1600983.

H. D. Holland. Volcanic gases, black smokers, and the great oxidation event. *Geochimica et Cosmochimica Acta*, 66:3811–3826, 2002. doi: 10.1016/S0016-7037(02)00950-X.

H. D. Holland. The oxygenation of the atmosphere and oceans. *Philosophical Transactions of the Royal Society B*, 361:903–915, 2006. doi: 10.1098/rstb.2006.1838.

H. D. Holland. Why the atmosphere became oxygenated: A proposal. *Geochimica et Cosmochimica Acta*, 73(18):5241–5255, 2009. doi: 10.1016/j.gca.2009.05.070.

T. T. Isson, N. J. Planavsky, L. A. Coogan, E. M. Stewart, J. J. Ague, E. W. Bolton, S. Zhang, N. R. McKenzie, and L. R. Kump. Evolution of the global carbon cycle and climate regulation on Earth. *Global Biogeochemical Cycles*, 34(2):e2018GB006061, 2020. doi: 10.1029/2018GB006061.

G. Izon, G. Luo, B. T. Uveges, N. Beukes, K. Kitajima, S. Ono, J. W. Valley, X. Ma, and R. E. Summons. Bulk and grain-scale minor sulfur isotope data reveal complexities in the dynamics of Earth's oxygenation. *Proceedings of the National Academy of Sciences*, 119(13):e2025606119, 2022. doi: 10.1073/pnas.2025606119.

A. Y. Jaziri, B. Charnay, F. Selsis, J. Leconte, and F. Lefèvre. Dynamics of the Great Oxidation Event from a 3D photochemical–climate model. *Climate of the Past*, 18(10):2421–2447, 2022. doi: 10.5194/cp-18-2421-2022.

J. E. Johnson, A. Gerpheide, M. P. Lamb, and W. W. Fischer. O_2 constraints from Paleoproterozoic detrital pyrite and uraninite. *Geological Society of America Bulletin*, 126(5-6):813–830, 2014. doi: 10.1130/B30949.1.

S. Kadoya and E. Tajika. Conditions for oceans on Earth-like planets orbiting within the habitable zone: Importance of volcanic CO_2 degassing. *The Astrophysical Journal*, 790(2):107, 2014. doi: 10.1088/0004-637X/790/2/107.

S. Kadoya and E. Tajika. Evolutionary climate tracks of Earth-like planets. *The Astrophysical Journal Letters*, 815(1):L7, 2015. doi: 10.1088/2041-8205/815/1/L7.

S. Kadoya, D. C. Catling, R. W. Nicklas, I. S. Puchtel, and A. D. Anbar. Mantle cooling causes more reducing volcanic gases and gradual reduction of the atmosphere. *Geochemical Perspectives Letters*, 13:25–29, 2020a. doi: 10.7185/geochemlet.2009.

S. Kadoya, D. C. Catling, R. W. Nicklas, I. S. Puchtel, and A. D. Anbar. Mantle data imply a decline of oxidizable volcanic gases could have triggered the Great Oxidation. *Nature Communications*, 11:2774, 2020b. doi: 10.1038/s41467-020-16493-1.

Y. Kanzaki and T. Murakami. Estimates of atmospheric CO_2 in the Neoarchean–Paleoproterozoic from paleosols. *Geochimica et Cosmochimica Acta*, 159:190–219, 2015. doi: 10.1016/j.gca.2015.03.011.

Y. Kanzaki and T. Murakami. Estimates of atmospheric O_2 in the Paleoproterozoic from paleosols. *Geochimica et Cosmochimica Acta*, 174:263–290, 2016. doi: 10.1016/j.gca.2015.11.022.

J. A. Karhu and H. D. Holland. Carbon isotopes and the rise of atmospheric oxygen. *Geology*, 24:867–870, 1996. doi: 10.1130/0091-7613(1996)024⟨0867:CIATRO⟩2.3.CO;2.

J. F. Kasting. What caused the rise of atmospheric O_2? *Chemical Geology*, 362:13–25, 2013. doi: 10.1016/j.chemgeo.2013.05.039.

J. F. Kasting and A. Ji. Atmospheric oxygen and methane on the early Earth. *Philosophical Transactions of the Royal Society B*, 380:20240093, 2025. doi: 10.1098/rstb.2024.0093.

C. B. Keller and B. Schoene. Statistical geochemistry reveals disruption in secular lithospheric evolution about 2.5 Gyr ago. *Nature*, 485(7399):490–493, 2012. doi: 10.1038/nature11024.

P. Kharecha, J. Kasting, and J. Siefert. A coupled atmosphere–ecosystem model of the early Archean Earth. *Geobiology*, 3(2):53–76, 2005. doi: 10.1111/j.1472-4669.2005.00049.x.

J. L. Kirschvink and R. E. Kopp. Palaeoproterozoic ice houses and the evolution of oxygen-mediating enzymes: the case for a late origin of photosystem II. *Philosophical Transactions of the Royal Society B*, 363(1504):2755–2765, 2008. doi: 10.1098/rstb.2008.0024.

K. O. Konhauser, E. Pecoits, S. V. Lalonde, D. Papineau, E. G. Nisbet, M. E. Barley, N. T. Arndt, K. Zahnle, and B. S. Kamber. Oceanic nickel depletion and a methanogen famine before the Great Oxidation Event. *Nature*, 458:750–753, 2009. doi: 10.1038/nature07858.

K. O. Konhauser, L. J. Robbins, E. Pecoits, C. Peacock, A. Kappler, and S. V. Lalonde. The Archean nickel famine revisited. *Astrobiology*, 15(10):804–815, 2015. doi: 10.1089/ast.2015.1301.

R. E. Kopp, J. L. Kirschvink, I. A. Hilburn, and C. Z. Nash. The Paleoproterozoic snowball Earth: A climate disaster triggered by the evolution of oxygenic photosynthesis. *Proceedings of the National Academy of Sciences*, 102:11131–11136, 2005. doi: 10.1073/pnas.0504878102.

J. Korenaga. Plate tectonics, flood basalts and the evolution of Earth's oceans. *Terra Nova*, 20(6):419–439, 2008. doi: 10.1111/j.1365-3121.2008.00843.x.

J. Korenaga. Crustal evolution and mantle dynamics through Earth history. *Philosophical Transactions of the Royal Society A*, 376(2132):20170408, 2018. doi: 10.1098/rsta.2017.0408.

J. Krissansen-Totton and D. C. Catling. Constraining climate sensitivity and continental versus seafloor weathering using an inverse geological carbon cycle model. *Nature Communications*, 8:15423, 2017. doi: 10.1038/ncomms15423.

J. Krissansen-Totton, R. Buick, and D. C. Catling. A statistical analysis of the carbon isotope record from the Archean to Phanerozoic and implications for the rise of oxygen. *American Journal of Science*, 315(4): 275–316, 2015. doi: 10.2475/04.2015.01.

J. Krissansen-Totton, G. N. Arney, and D. C. Catling. Constraining the climate and ocean pH of the early Earth with a geological carbon cycle model. *Proceedings of the National Academy of Sciences*, 115(16): 4105–4110, 2018. doi: 10.1073/pnas.1721296115.

J. Krissansen-Totton, M. A. Kipp, and D. C. Catling. Carbon cycle inverse modeling suggests large changes in fractional organic burial are consistent with the carbon isotope record and may have contributed to the rise of oxygen. *Geobiology*, 19(4):342–363, 2021. doi: 10.1111/gbi.12440.

L. R. Kump and M. E. Barley. Increased subaerial volcanism and the rise of atmospheric oxygen 2.5 billion years ago. *Nature*, 448:1033–1036, 2007. doi: 10.1038/nature06058.

L. R. Kump and W. E. Seyfried Jr. Hydrothermal Fe fluxes during the Precambrian: Effect of low oceanic sulfate concentrations and low hydrostatic pressure on the composition of black smokers. *Earth and Planetary Science Letters*, 235(3-4):654–662, 2005. doi: 10.1016/j.epsl.2005.04.040.

T. A. Laakso and D. P. Schrag. Regulation of atmospheric oxygen during the Proterozoic. *Earth and Planetary Science Letters*, 388:81–91, 2014. doi: 10.1016/j.epsl.2013.11.049.

T. A. Laakso and D. P. Schrag. A theory of atmospheric oxygen. *Geobiology*, 15(3):366–384, 2017. doi: 10.1111/gbi.12230.

T. A. Laakso, E. A. Sperling, D. T. Johnston, and A. H. Knoll. Ediacaran reorganization of the marine phosphorus cycle. *Proceedings of the National Academy of Sciences*, 117(22):11961–11967, 2020. doi: 10.1073/pnas.1916738117.

G. Le Hir, Y. Goddéris, Y. Donnadieu, and G. Ramstein. A geochemical modelling study of the evolution of the chemical composition of seawater linked to a "snowball" glaciation. *Biogeosciences*, 5(1):253–267, 2008a. doi: 10.5194/bg-5-253-2008.

G. Le Hir, G. Ramstein, Y. Donnadieu, and Y. Goddéris. Scenario for the evolution of atmospheric pCO_2 during a snowball Earth. *Geology*, 36(1):47–50, 2008b. doi: 10.1130/G24124A.1.

G. Le Hir, Y. Donnadieu, Y. Goddéris, R. T. Pierrehumbert, G. P. Halverson, M. Macouin, A. Nédélec, and G. Ramstein. The snowball Earth aftermath: Exploring the limits of continental weathering processes. *Earth and Planetary Science Letters*, 277(3–4):453–463, 2009. doi: 10.1016/j.epsl.2008.11.010.

C.-T. A. Lee, L. Y. Yeung, N. R. McKenzie, Y. Yokoyama, K. Ozaki, and A. Lenardic. Two-step rise of atmospheric oxygen linked to the growth of continents. *Nature Geoscience*, 9(6):417–424, 2016. doi: 10.1038/ngeo2707.

T. M. Lenton, S. J. Daines, and B. J. W. Mills. COPSE reloaded: An improved model of biogeochemical cycling over Phanerozoic time. *Earth-Science Reviews*, 178:1–28, 2018. doi: 10.1016/j.earscirev.2017.12.004.

Z.-H. Li, T. M. Lenton, F.-F. Zhang, Z.-Q. Chen, and S. J. Daines. Earth system instability amplified biogeochemical oscillations following the end-Permian mass extinction. *Nature Communications*, 16:3703, 2025. doi: 10.1038/s41467-025-59038-0.

Z.-H. Li, Z.-Q. Chen, S. J. Daines, F. Zhang, and T. M. Lenton. Periodic ocean oxygenation events during the mid-Ediacaran. *Nature Geoscience*, 19(2):216–222, 2026. doi: 10.1038/s41561-025-01883-1.

R. P. Lowell and S. M. Keller. High-temperature seafloor hydrothermal circulation over geologic time and Archean banded iron formations. *Geophysical Research Letters*, 30(7):1391, 2003. doi: 10.1029/2002GL016536.

G. Luo, S. Ono, N. J. Beukes, D. T. Wang, S. Xie, and R. E. Summons. Rapid oxygenation of Earth's atmosphere 2.33 billion years ago. *Science Advances*, 2(5):e1600134, 2016. doi: 10.1126/sciadv.1600134.

J. S. Marmo. The Lower Proterozoic Hokkalampi paleosol in North Karelia, eastern Finland. In *Early Organic Evolution*, pages 41–66. Springer, 1992. doi: 10.1007/978-3-642-76884-2_5.

A. P. Martin, D. J. Condon, A. R. Prave, and A. Lepland. A review of temporal constraints for the Palaeoproterozoic large, positive carbonate carbon isotope excursion (the Lomagundi–Jatuli Event). *Earth-Science Reviews*, 127:242–261, 2013. doi: 10.1016/j.earscirev.2013.10.006.

B. Marty, D. V. Bekaert, M. W. Broadley, and C. Jaupart. Geochemical evidence for high volatile fluxes from the mantle at the end of the Archaean. *Nature*, 575(7783):485–488, 2019. doi: 10.1038/s41586-019-1745-7.

K. Menou. Climate stability of habitable Earth-like planets. *Earth and Planetary Science Letters*, 429:20–24, 2015. doi: 10.1016/j.epsl.2015.07.046.

A. E. G. Millikin, B. T. Uveges, G. Izon, A. M. Bauer, R. E. Summons, D. A. D. Evans, and A. D. Rooney. A new Re-Os age constraint informs the dynamics of the Great Oxidation Event. *Geology*, 52(11):857–862, 2024. doi: 10.1130/G52481.1.

B. Mills, A. J. Watson, C. Goldblatt, R. Boyle, and T. M. Lenton. Timing of Neoproterozoic glaciations linked to transport-limited global weathering. *Nature Geoscience*, 4(12):861–864, 2011. doi: 10.1038/ngeo1305.

B. Mills, T. M. Lenton, and A. J. Watson. Proterozoic oxygen rise linked to shifting balance between seafloor and terrestrial weathering. *Proceedings of the National Academy of Sciences*, 111(25):9073–9078, 2014. doi: 10.1073/pnas.1321679111.

B. J. W. Mills, C. R. Scotese, N. G. Walding, G. A. Shields, and T. M. Lenton. Elevated CO_2 degassing rates prevented the return of Snowball Earth during the Phanerozoic. *Nature Communications*, 8:1110, 2017. doi: 10.1038/s41467-017-01456-w.

C. Minsky, R. Wordsworth, D. T. Johnston, and A. H. Knoll. Repeated snowball–hothouse cycles within the Neoproterozoic Sturtian glaciation. *Proceedings of the National Academy of Sciences*, 123(19):e2525919123, 2026. doi: 10.1073/pnas.2525919123.

J. L. Morris, M. N. Puttick, J. W. Clark, D. Edwards, P. Kenrick, S. Pressel, C. H. Wellman, Z. Yang, H. Schneider, and P. C. J. Donoghue. The timescale of early land plant evolution. *Proceedings of the National Academy of Sciences*, 115:E2274–E2283, 2018. doi: 10.1073/pnas.1719588115.

A. Y. Nke, R. E. M. Rickaby, H. Tsikos, P. R. D. Mason, X. Mhlanga, and R. Tostevin. A window into transition metal availability in early Palaeoproterozoic seawater. *Scientific Reports*, 15:44267, 2025. doi: 10.1038/s41598-025-27806-z.

J. Olejarz, Y. Iwasa, A. H. Knoll, and M. A. Nowak. The Great Oxygenation Event as a consequence of ecological dynamics modulated by planetary change. *Nature Communications*, 12:3985, 2021. doi: 10.1038/s41467-021-23286-7.

C. M. Ostrander, A. W. Heard, Y. Shu, A. Bekker, S. W. Poulton, K. P. Olesen, and S. G. Nielsen. Onset of coupled atmosphere–ocean oxygenation 2.3 billion years ago. *Nature*, 631(8020):335–339, 2024. doi: 10.1038/s41586-024-07551-5.

A. Panahi, G. M. Young, and R. H. Rainbird. Behavior of major and trace elements (including REE) during Paleoproterozoic pedogenesis and diagenetic alteration of an Archean granite near Ville Marie, Québec, Canada. *Geochimica et Cosmochimica Acta*, 64:2199–2220, 2000. doi: 10.1016/S0016-7037(99)00420-2.

J. G. Park, M. N. Hudgins, P. Fralick, J. T. Shelley, and M. F. Schaller. Breathing life into the boring billion: Direct constraints from 1.4 Ga fluid inclusions reveal a fair climate and oxygenated atmosphere. *Proceedings of the National Academy of Sciences*, 122(52):e2513030122, 2025. doi: 10.1073/pnas.2513030122.

A. A. Pavlov and J. F. Kasting. Mass-independent fractionation of sulfur isotopes in Archean sediments: strong evidence for an anoxic Archean atmosphere. *Astrobiology*, 2:27–41, 2002. doi: 10.1089/153110702753621321.

A. A. Pavlov, J. F. Kasting, L. L. Brown, K. A. Rages, and R. Freedman. Greenhouse warming by CH_4 in the atmosphere of early Earth. *Journal of Geophysical Research: Planets*, 105:11981–11990, 2000. doi: 10.1029/1999JE001134.

A. A. Pavlov, L. L. Brown, and J. F. Kasting. UV shielding of NH_3 and O_2 by organic hazes in the Archean atmosphere. *Journal of Geophysical Research: Planets*, 106(E10):23267–23287, 2001. doi: 10.1029/2000JE001448.

P. Philippot, J. N. Ávila, B. A. Killingsworth, S. Tessalina, F. Baton, T. Caquineau, E. Muller, E. Pecoits, P. Cartigny, S. V. Lalonde, T. R. Ireland, C. Thomazo, M. J. van Kranendonk, and V. Busigny. Globally asynchronous sulphur isotope signals require re-definition of the Great Oxidation Event. *Nature Communications*, 9:2245, 2018. doi: 10.1038/s41467-018-04621-x.

N. J. Planavsky, O. J. Rouxel, A. Bekker, S. V. Lalonde, K. O. Konhauser, C. T. Reinhard, and T. W. Lyons. The evolution of the marine phosphate reservoir. *Nature*, 467:1088–1090, 2010. doi: 10.1038/nature09485.

N. J. Planavsky, D. Asael, A. Hofmann, C. T. Reinhard, S. V. Lalonde, A. Knudsen, X. Wang, F. Ossa Ossa, E. Pecoits, A. J. B. Smith, N. J. Beukes, A. Bekker, T. M. Johnson, K. O. Konhauser, T. W. Lyons, and O. J. Rouxel. Evidence for oxygenic photosynthesis half a billion years before the Great Oxidation Event. *Nature Geoscience*, 7:283–286, 2014a. doi: 10.1038/ngeo2122.

N. J. Planavsky, C. T. Reinhard, X. Wang, D. Thomson, P. McGoldrick, R. H. Rainbird, T. Johnson, W. W. Fischer, and T. W. Lyons. Low mid-Proterozoic atmospheric oxygen levels and the delayed rise of animals. *Science*, 346:635–638, 2014b. doi: 10.1126/science.1258410.

S. W. Poulton, A. Bekker, V. M. Cumming, A. L. Zerkle, D. E. Canfield, and D. T. Johnston. A 200-million-year delay in permanent atmospheric oxygenation. *Nature*, 592(7853):232–236, 2021. doi: 10.1038/s41586-021-03393-7.

B. Rasmussen, A. Bekker, and I. R. Fletcher. Correlation of Paleoproterozoic glaciations based on U-Pb zircon ages for tuff beds in the Transvaal and Huronian Supergroups. *Earth and Planetary Science Letters*, 382:173–180, 2013. doi: 10.1016/j.epsl.2013.08.037.

B. Rasmussen, J.-W. Zi, and A. Bekker. New U-Pb zircon tuff ages and revised stratigraphic correlations in the Superior craton during the Great Oxidation Episode. *Earth and Planetary Science Letters*, 640:118779, 2024. doi: 10.1016/j.epsl.2024.118779.

C. T. Reinhard, N. J. Planavsky, and T. W. Lyons. Long-term sedimentary recycling of rare sulphur isotope anomalies. *Nature*, 497(7447):100–103, 2013. doi: 10.1038/nature12021.

C. T. Reinhard, N. J. Planavsky, B. C. Gill, K. Ozaki, L. J. Robbins, T. W. Lyons, W. W. Fischer, C. Wang, D. B. Cole, and K. O. Konhauser. Evolution of the global phosphorus cycle. *Nature*, 541:386–389, 2017. doi: 10.1038/nature20772.

L. J. Robbins, S. V. Lalonde, M. A. Saito, N. J. Planavsky, A. M. Mloszewska, E. Pecoits, C. Scott, C. L. Dupont, A. Kappler, and K. O. Konhauser. Authigenic iron oxide proxies for marine zinc over geological time and implications for eukaryotic metallome evolution. *Geobiology*, 11(4):295–306, 2013. doi: 10.1111/gbi.12036.

L. J. Robbins, S. Mughal, N. Mahmoudi, D. B. Mills, H. R. Rucker, E. E. Stüeken, A. D. Anbar, A. H. Knoll, B. Kaçar, and K. O. Konhauser. Revisiting the bio-inorganic bridge 25 years later. *Annual Review of Earth and Planetary Sciences*, 54:389–410, 2026. doi: 10.1146/annurev-earth-040523-125151.

C. V. Rubinstein, P. Gerrienne, G. S. de la Puente, R. A. Astini, and P. Steemans. Early Middle Ordovician evidence for land plants in Argentina (eastern Gondwana). *New Phytologist*, 188:365–369, 2010. doi: 10.1111/j.1469-8137.2010.03433.x.

A. J. Rushby, M. Johnson, B. J. W. Mills, A. J. Watson, and M. W. Claire. Long-term planetary habitability and the carbonate-silicate cycle. *Astrobiology*, 18(5):469–480, 2018. doi: 10.1089/ast.2017.1693.

R. Rye and H. D. Holland. Paleosols and the evolution of atmospheric oxygen: a critical review. *American Journal of Science*, 298:621–672, 1998. doi: 10.2475/ajs.298.8.621.

R. Rye and H. D. Holland. Geology and geochemistry of paleosols developed on the Hekpoort Basalt, Pretoria Group, South Africa. *American Journal of Science*, 300:85–141, 2000. doi: 10.2475/ajs.300.2.85.

M. Saunois, A. R. Stavert, B. Poulter, P. Bousquet, J. G. Canadell, R. B. Jackson, P. A. Raymond, E. J. Dlugokencky, S. Houweling, P. K. Patra, et al. The global methane budget 2000–2017. *Earth System Science Data*, 12(3):1561–1623, 2020. doi: 10.5194/essd-12-1561-2020.

M. Schidlowski, R. Eichmann, and C. E. Junge. Carbon isotope geochemistry of the Precambrian Lomagundi carbonate province, Rhodesia. *Geochimica et Cosmochimica Acta*, 40:449–455, 1976. doi: 10.1016/0016-7037(76)90010-7.

S. Schröder, N. J. Beukes, and R. A. Armstrong. Detrital zircon constraints on the tectonostratigraphy of the Paleoproterozoic Pretoria Group, South Africa. *Precambrian Research*, 278:362–393, 2016. doi: 10.1016/j.precamres.2016.03.016.

C. Scott, N. J. Planavsky, C. L. Dupont, B. Kendall, B. C. Gill, L. J. Robbins, K. F. Husband, G. L. Arnold, B. A. Wing, S. W. Poulton, A. Bekker, A. D. Anbar, K. O. Konhauser, and T. W. Lyons. Bioavailability of zinc in marine systems through time. *Nature Geoscience*, 6(2):125–128, 2013. doi: 10.1038/ngeo1679.

M. H. Senger, J. H. F. L. Davies, M. Ovtcharova, N. Beukes, A. Gumsley, S. P. Gaynor, A. Ulianov, R. Ngobeli, and U. Schaltegger. Improving the chronostratigraphic framework of the Transvaal Supergroup (South Africa) through in-situ and high-precision U-Pb geochronology. *Precambrian Research*, 392:107070, 2023. doi: 10.1016/j.precamres.2023.107070.

N. D. Sheldon. Precambrian paleosols and atmospheric CO_2 levels. *Precambrian Research*, 147:148–155, 2006. doi: 10.1016/j.precamres.2006.02.004.

K. Sheng, Z.-H. Li, J.-L. Zhou, Y.-B. Lin, G.-L. Xiong, G.-Y. Ren, Z.-Q. Chen, T. M. Lenton, S.-z. Shen, and F. Zhang. Earth system instability explains redox paradox during late Cambrian SPICE event. *Science Advances*, 12(15):eaeb9224, 2026. doi: 10.1126/sciadv.aeb9224.

N. H. Sleep and K. Zahnle. Carbon dioxide cycling and implications for climate on ancient Earth. *Journal of Geophysical Research: Planets*, 106(E1):1373–1399, 2001. doi: 10.1029/2000JE001247.

S. P. Slotznick, J. E. Johnson, B. Rasmussen, T. D. Raub, S. M. Webb, J.-W. Zi, J. L. Kirschvink, and W. W. Fischer. Reexamination of 2.5-Ga "whiff" of oxygen interval points to anoxic ocean before GOE. *Science Advances*, 8(1):eabj7190, 2022. doi: 10.1126/sciadv.abj7190.

S. P. Slotznick, J. E. Johnson, B. Rasmussen, T. D. Raub, S. M. Webb, J.-W. Zi, J. L. Kirschvink, and W. W. Fischer. Response to comment on "Reexamination of 2.5-Ga 'whiff' of oxygen interval points to anoxic ocean before GOE". *Science Advances*, 9(14):eadg1530, 2023. doi: 10.1126/sciadv.adg1530.

M. A. Smit and K. Mezger. Earth's early O_2 cycle suppressed by primitive continents. *Nature Geoscience*, 10(10):788–792, 2017. doi: 10.1038/ngeo3030.

S. M. Som, R. Buick, J. W. Hagadorn, T. S. Blake, J. M. Perreault, J. P. Harnmeijer, and D. C. Catling. Earth's air pressure 2.7 billion years ago constrained to less than half of modern levels. *Nature Geoscience*, 9(6):448–451, 2016. doi: 10.1038/ngeo2713.

C. J. Spencer, J. B. Murphy, C. L. Kirkland, Y. Liu, and R. N. Mitchell. A Palaeoproterozoic tectonomagmatic lull as a potential trigger for the supercontinent cycle. *Nature Geoscience*, 11(2):97–101, 2018. doi: 10.1038/s41561-017-0051-y.

A. Swain, A. J. Kaufman, M. Kalinowski, S. A. Yarwood, and W. F. Fagan. Were Neoarchean atmospheric methane hazes and early Paleoproterozoic glaciations driven by the rise of oxygen in surface environments? *Earth and Planetary Science Letters*, 643:118900, 2024. doi: 10.1016/j.epsl.2024.118900.

E. Tajika. Long-term stability of climate and global glaciations throughout the evolution of the Earth. *Earth, Planets and Space*, 59(4):293–299, 2007. doi: 10.1186/BF03353107.

E. Tajika and M. Harada. A possible relationship bewteen the Great Oxidation Event and the Paleoproterozoic snowball Earth event. *Viva Origino*, 45(4):5, 2017. doi: 10.50968/vivaorigino.45_5.

M. Tang, K. Chen, and R. L. Rudnick. Archean upper crust transition from mafic to felsic marks the onset of plate tectonics. *Science*, 351(6271):372–375, 2016. doi: 10.1126/science.aad5513.

Y. Teitler, G. Le Hir, F. Fluteau, P. Philippot, and Y. Donnadieu. Investigating the Paleoproterozoic glaciations with 3-D climate modeling. *Earth and Planetary Science Letters*, 395:71–80, 2014. doi: 10.1016/j.epsl.2014.03.044.

S. Utsunomiya, T. Murakami, M. Nakada, and T. Kasama. Iron oxidation state of a 2.45-Byr-old paleosol developed on mafic volcanics. *Geochimica et Cosmochimica Acta*, 67:213–221, 2003. doi: 10.1016/S0016-7037(02)01083-9.

B. T. Uveges, G. Izon, S. Ono, N. J. Beukes, and R. E. Summons. Reconciling discrepant minor sulfur isotope records of the Great Oxidation Event. *Nature Communications*, 14:279, 2023. doi: 10.1038/s41467-023-35820-w.

A. Voigt, D. S. Abbot, R. T. Pierrehumbert, and J. Marotzke. Initiation of a Marinoan Snowball Earth in a state-of-the-art atmosphere-ocean general circulation model. *Climate of the Past*, 7(1):249–263, 2011. doi: 10.5194/cp-7-249-2011.

S.-J. Wang, R. L. Rudnick, R. M. Gaschnig, H. Wang, and L. E. Wasylenki. Methanogenesis sustained by sulfide weathering during the Great Oxidation Event. *Nature Geoscience*, 12(4):296–300, 2019. doi: 10.1038/s41561-019-0320-z.

M. R. Warke and S. Schröder. Synsedimentary fault control on the deposition of the Duitschland Formation (South Africa): implications for depositional settings, Paleoproterozoic stratigraphic correlations, and the GOE. *Precambrian Research*, 310:348–364, 2018. doi: 10.1016/j.precamres.2018.03.001.

M. R. Warke, T. Di Rocco, A. L. Zerkle, A. Lepland, A. R. Prave, A. P. Martin, Y. Ueno, D. J. Condon, and M. W. Claire. The Great Oxidation Event preceded a Paleoproterozoic "snowball Earth". *Proceedings of the National Academy of Sciences*, 117:13314–13320, 2020. doi: 10.1073/pnas.2003090117.

J. J. Williams, B. J. W. Mills, and T. M. Lenton. A tectonically driven Ediacaran oxygenation event. *Nature Communications*, 10:2690, 2019. doi: 10.1038/s41467-019-10286-x.

N. F. Wogan, D. C. Catling, K. J. Zahnle, and M. W. Claire. Rapid timescale for an oxic transition during the Great Oxidation Event and the instability of low atmospheric O_2. *Proceedings of the National Academy of Sciences*, 119(37):e2205618119, 2022. doi: 10.1073/pnas.2205618119.

K. Wong, E. Mason, S. Brune, M. East, M. Edmonds, and S. Zahirovic. Deep carbon cycling over the past 200 million years: A review of fluxes in different tectonic settings. *Frontiers in Earth Science*, 7:263, 2019. doi: 10.3389/feart.2019.00263.

U. G. Wortmann, T. Tsan, M. Niazi, I. A. Ma, R. Navasardyan, M.-R. Marun, B. S. Chede, J. Zhong, and M. Wolfe. The Earth Science Box Modeling Toolkit (ESBMTK 0.14.0.11): a Python library for research and teaching. *Geoscientific Model Development*, 18(4):1155–1167, 2025. doi: 10.5194/gmd-18-1155-2025.

J. Yang, W. R. Peltier, and Y. Hu. The initiation of modern soft and hard Snowball Earth climates in CCSM4. *Climate of the Past*, 8:907–918, 2012. doi: 10.5194/cp-8-907-2012.

W. Yang and H. D. Holland. The Hekpoort paleosol profile in Strata 1 at Gaborone, Botswana: soil formation during the Great Oxidation Event. *American Journal of Science*, 303:187–220, 2003. doi: 10.2475/ajs.303.3.187.

K. Zahnle and N. H. Sleep. Carbon dioxide cycling through the mantle and implications for the climate of ancient Earth. *Geological Society, London, Special Publications*, 199(1):231–257, 2002. doi: 10.1144/GSL.SP.2002.199.01.12.

K. Zahnle, M. Claire, and D. Catling. The loss of mass-independent fractionation in sulfur due to a Palaeoproterozoic collapse of atmospheric methane. *Geobiology*, 4:271–283, 2006. doi: 10.1111/j.1472-4669.2006.00085.x.

K. J. Zahnle, M. Gacesa, and D. C. Catling. Strange messenger: A new history of hydrogen on Earth, as told by Xenon. *Geochimica et Cosmochimica Acta*, 244:56–85, 2019. doi: 10.1016/j.gca.2018.09.017.

S. Zhang, X. Wang, H. Wang, C. J. Bjerrum, E. U. Hammarlund, M. M. Costa, J. N. Connelly, B. Zhang, J. Su, and D. E. Canfield. Sufficient oxygen for animal respiration 1,400 million years ago. *Proceedings of the National Academy of Sciences*, 113:1731–1736, 2016. doi: 10.1073/pnas.1523449113.